Analysis of the Structure of Parameter Degeneracy in Neutrino Oscillations

Shoichi Uchinami

Department of Physics
Tokyo Metropolitan University

Contents

Chapter 1

Introduction and Summary

Discovery of the neutrino oscillation indicated that neutrinos have masses, the property which is not contained in the standard model of elementary particles. It means that there is a new physics beyond the standard model, giving a significant impact on high energy physics. Probing physics behind the neutrino mass and the lepton flavor mixing with comprehension of the mixing in the quark sector, are expected to open a new window to deeper understanding of fundamental matter in nature.

Until now, experiments using atmospheric, solar, reactor, and accelerator neutrinos have revealed the structure of 2-3 and 1-2 sector of the Maki-Nakagawa-Sakata mixing matrix, U_{MNS}, which describes the three generation lepton flavor mixing. The results of these experiments told us that the value of θ_{23} is close to the maximal angle 45°, and θ_{12} is about 30°, both of which are large contrary to what was widely believed at that time based on small mixing in the quark sector. The remaining outstanding issues are the determination of the last mixing angle of U_{MNS}, θ_{13}, which is known to be small, the Kobayashi-Maskawa type CP-phase δ in the lepton sector, and the pattern of neutrino masses.

It is expected that future neutrino experiments will be able to have sensitivities to these parameters. Especially, the long baseline oscillation experiments which use the artificial neutrino beams have a potential to determine the lepton flavor mixing because they can be setup with the appropriate experimental condition in order to measure the unknown parameters. The CP-violating effect caused by the phase δ arises as a genuine three-flavor effect and it receives various suppression factors owing to this character. To determine δ, therefore, we need precision measurement and the experiments inevitably have the character of simultaneous measurement of both δ and θ_{13} in seeking such an accuracy.

It is known that there is a serious problem in measurement of θ_{13} and δ. It is the problem of existence of multiple solutions, which is usually called as the "parameter degeneracy". In general, there exist eight solutions which reproduce the two neutrino oscillation probabilities of $\nu_\mu \to \nu_e$ and $\bar{\nu}_\mu \to \bar{\nu}_e$ channels at a given energy. Furthermore, the degenerate solutions depend intricately on various mixing parameters. Therefore, in order to have a clear understanding of the results of feature long baseline experiments, it is important to reveal the whole picture of the parameter degeneracy and understand the structure of degenerate solutions. If there exist any non-standard phenomena in neutrino propagation, complete understanding of the degeneracy would help us to determine the neutrino oscillation parameters avoiding the confusion caused by the non-standard effect.

The purpose of this thesis is to make the structure of the parameter degeneracy manifest. It is nothing but the invariance of a certain set of the oscillation probabilities under the discrete transformations. They consist of the following three mappings:

(1). intrinsic mapping,
(2). sign-Δm_{31}^2 mapping,
(3). θ_{23} octant mapping.

By combing these three mappings one can reconstruct all the eightfold degenerate solutions from the true one. The feature is represented pictorially in Fig. 1.1. Notice that the sign-octant mapping can be constructed by doing the two successive mappings, the sign-Δm_{31}^2 and the θ_{23} octant mappings.
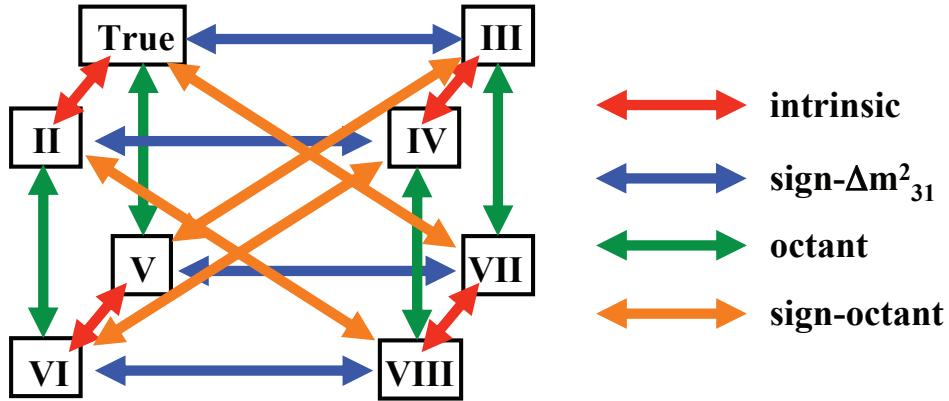
Figure 1.1: The relationships between the true solution and the seven degenerate solutions are exhibited by color arrows, representing mappings which create the them from the others.

The explicit forms of the mappings can be derived by obtaining analytic solutions of the eightfold degeneracy. In the case of CP-conjugate measurement this task is carried out explicitly in this thesis. In the T-conjugate measurement, the CPT-conjugate measurement, and in a setting combining the golden ($\nu_e \rightarrow \nu_\mu$) and the silver ($\nu_e \rightarrow \nu_\tau$) channels, several forms of the mapping can be obtained by the symmetry obeyed by the approximate formula of the oscillation probability derived by Cervera et al.. For the latter, however, we also work out the explicit solutions to confirm the above expectation. The explicit analytic solutions would merit understanding of results of future experiments.

We display various features of the parameter degeneracy for CP-conjugate measurement by using color graduation and other types of plots. Several characteristic features of the degeneracy are clearly represented. The difference between the true and degenerate solution of θ_{13} is, in general, large for the intrinsic degeneracy. However, its energy dependence is relatively strong suggesting that it can be resolved by spectrum analysis. Whereas in the sign-Δm_{31}^2 and the θ_{23} octant degeneracies the differences are generally small and depend on energy only weakly in short and medium baseline distances. The similar feature exists also for CP phase δ. Therefore, it would be hard to lift the latter types of degeneracies. It was shown that the degenerate solution of δ can be approximated by $\pi - \delta$ in various regions of the parameters. It indicates that confusion of CP violation and CP conservation

is minimal in particular at short baselines. On the other hand, we also observe that in longer baselines the sign-Δm_{31}^2 degeneracy produces fake solutions of δ which can confuse CP violation with CP conservation.

To understand better these characteristic features of the degeneracy we also derive the perturbative expressions of the degenerate solutions in CP-conjugate measurement. The matter perturbation formula of the sign-Δm_{31}^2 degeneracy solution gives us simple understanding of the above mentioned features. The θ_{23} octant degeneracy solution of θ_{13} is close to the true one and its energy dependence is so weak even in the neutrino factory setting. To understand these features of the octant degeneracy, we also formulate the maximal θ_{23} perturbation theory by taking $\epsilon_{\text{oct}} \equiv \theta_{23} - \frac{\pi}{4}$ as the small expansion parameter.

Finally, we also discuss the parameter degeneracy in the system with non-standard interactions (NSI) of neutrinos with matter propagating in the earth. It is shown that the conventional types of degeneracy discussed above are modified by the presence of NSI, and a nobel type of degeneracy exchanging the solar and the atmospheric variable exists.

Chapter 2

Neutrino Mass and Oscillation

In this chapter, we review neutrino mixing and oscillations. First, we give an overview of how the fermions except for neutrinos get their masses in the standard electroweak model and its mixing structure in the quark sector. Next, we review the neutrino oscillation mechanism and show the constraints on the neutrino masses and mixing angles from various experiments.

2.1 Standard model and mass matrix

The standard model of the elementary particles has succeeded explaining a lot of phenomena of nature. It consists of the Quantum Chromo Dynamics (QCD) which describes the strong interaction, and the standard electroweak model, the model of the electromagnetic and weak interactions [1]. In this section we review the standard electroweak model to recollect how fermions get their masses and the resultant structure of flavor mixing.

The standard electroweak model is constructed on the basis of $SU(2)_L \times U(1)_Y$ gauge symmetry.

We denote the fermions by the chirality as

$$\Psi_L = \frac{1 - \gamma^5}{2}\Psi, \quad \Psi_R = \frac{1 + \gamma^5}{2}\Psi, \tag{2.1}$$

in order to construct the invariant Lagrangian under the $SU(2)_L$ transformation.

The left-handed fermions can be written by the doublets of $SU(2)_L$ as

$$
\begin{aligned}
q_i &: \begin{pmatrix} u_L \\ d_L \end{pmatrix}, \begin{pmatrix} c_L \\ s_L \end{pmatrix}, \begin{pmatrix} t_L \\ b_L \end{pmatrix}, \\
l_i &: \begin{pmatrix} \nu_{eL} \\ e_L \end{pmatrix}, \begin{pmatrix} \nu_{\mu L} \\ \mu_L \end{pmatrix}, \begin{pmatrix} \nu_{\tau L} \\ \tau_L \end{pmatrix}.
\end{aligned}
\tag{2.2}
$$

On the other hand, the right-handed fermions are the singlet under $SU(2)_L$ transformation

$$
\begin{aligned}
u_{Ri} &: u_R, c_R, t_R; \quad d_{Ri} : d_R, s_R, b_R \\
e_{Ri} &: e_R, \mu_R, \tau_R.
\end{aligned}
\tag{2.3}
$$

The right-handed neutrinos are not considered because there is no evidence of right-handed neutrinos.

Lagrangian of this model is written with the gauge bosons denoted $W_\mu^a (a = 1, 2, 3)$ and B_μ as

$$\mathcal{L} = -\frac{1}{4} F_{\mu\nu}^a F_a^{\mu\nu} - \frac{1}{4} B_{\mu\nu} B^{\mu\nu} + \bar{\Psi} i \gamma^\mu D_\mu \Psi + (D_\mu \Phi)^\dagger (D^\mu \Phi) - V(\Phi) + \mathcal{L}_Y \quad (2.4)$$

$$\mathcal{L}_Y = -\sum_{i,j} (f_{ij}^u \bar{q}_i \Phi^c u_{Rj} + f_{ij}^d \bar{q}_i \Phi d_{Rj} + f_{ij}^e \bar{l}_i \Phi e_{Ri} + h.c.)$$

$$F_{\mu\nu}^a = \partial_\mu W_\nu^a - \partial_\nu W_\mu - g \epsilon^a_{\ bc} W_\mu^b W_\nu^c$$

$$B_{\mu\nu} = \partial_\mu B_\nu - \partial_\nu B_\mu$$

$$D_\mu = \partial_\mu + ig W_\mu^a \tau_a + i\frac{g'}{2} B_\mu Y$$

$$\Phi = \begin{pmatrix} \phi^+ \\ \phi^0 \end{pmatrix}, \Phi^c = \begin{pmatrix} \phi^{0\dagger} \\ -\phi^- \end{pmatrix} \quad (2.5)$$

where $a = 1, 2, 3$ and Ψ are fermions determined in (2.2) and (2.3).

The important point is that the $SU(2)_L$ symmetry implies no mass term not only on the gauge bosons but also on the fermions. As we discuss later, The Higgs mechanism resolves this problem.

If the potential of Higgs bosons have the form of

$$V(\Phi) = -\mu^2 |\Phi|^2 + \lambda(|\Phi|^2)^2, \quad (2.6)$$

the vacuum is at non-zero ϕ

$$\Phi \to \begin{pmatrix} 0 \\ v/\sqrt{2} \end{pmatrix} \quad (2.7)$$

where $v = \sqrt{\mu^2/\lambda}$. Therefore at the vacuum, B and W^3 are mixed and reinterpreted as photon field A and neutral boson Z as

$$Z_\mu = \cos\theta_W W_\mu^3 - \sin\theta_W B_\mu$$

$$A_\mu = \sin\theta_W W_\mu^3 + \cos\theta_W B_\mu \quad (2.8)$$

where

$$\cos\theta_W \equiv \frac{g}{\sqrt{g^2 + g'^2}}, \quad \sin\theta_W \equiv \frac{g'}{\sqrt{g^2 + g'^2}}. \quad (2.9)$$

The gauge interaction terms are written by

$$\mathcal{L}_{int} = -\Big[g \sin\theta_W \bar{\Psi} \gamma^\mu A_\mu Q \Psi + \frac{g}{\cos\theta_W} \bar{\Psi} \gamma^\mu Z_\mu (I_3 - Q \sin^2\theta_W) \Psi$$

$$+ \frac{g}{\sqrt{2}} \bar{\Psi}_L \gamma^\mu (W_\mu^+ \tau_+ + W_\mu^- \tau_-) \Psi_L \Big] \quad (2.10)$$

7

where

$$
\begin{aligned}
W_\mu^\pm &\equiv \frac{1}{\sqrt{2}}(W_\mu^1 \mp iW_\mu^2), \\
\tau_\pm &\equiv \tau_1 \pm i\tau_2, \\
Q &\equiv \tau_3 + \frac{Y}{2}.
\end{aligned}
\tag{2.11}
$$

Considering gauge symmetry spontaneous breaking, we have the mass of Z and $W^\pm$ bosons,

$$
m_W = \frac{gv}{2},
\tag{2.12}
$$

$$
m_Z = \frac{gv}{2\cos\theta_W}.
\tag{2.13}
$$

Furthermore, the Yukawa coupling terms, $\mathcal{L}_Y$, give the fermion mass terms as

$$
\mathcal{L}_m = -\sum_{i,j}(\bar{u}_{Li}M_{ij}^u u_{Rj} + \bar{d}_{Li}M_{ij}^d d_{Rj} + \bar{e}_{Li}M_{ij}^e e_{Rj} + h.c.)
\tag{2.14}
$$

where $M_{ij}^\alpha \equiv vf_{ij}^\alpha/\sqrt{2}, \alpha = u, d, e$.

In general, we can take the arbitrary complex matrix for the Yukawa coupling constants. Therefore, the state of fermions in this expression is not the mass eigenstate but the state under the weak interaction (weak eigenstate). In order to get the diagonalized mass matrix, let us consider the bi-unitary transformation using unitary matrixes S^α and T^α

$$
S^u M^u T^{u\dagger} = M_{\mathrm{dia}}^u = \begin{pmatrix} m_u & 0 & 0 \\ 0 & m_c & 0 \\ 0 & 0 & m_t \end{pmatrix}
\tag{2.15}
$$

$$
S^d M^d T^{d\dagger} = M_{\mathrm{dia}}^d = \begin{pmatrix} m_d & 0 & 0 \\ 0 & m_s & 0 \\ 0 & 0 & m_b \end{pmatrix}
\tag{2.16}
$$

$$
S^e M^e T^{e\dagger} = M_{\mathrm{dia}}^e = \begin{pmatrix} m_e & 0 & 0 \\ 0 & m_\mu & 0 \\ 0 & 0 & m_\tau \end{pmatrix}.
\tag{2.17}
$$

The fermion mass terms are transformed as

$$
\begin{aligned}
-\mathcal{L}_m &= \overline{U}_L M^u U_R + \overline{D}_L M^d D_R + \overline{E}_L M^e E_R + h.c. \\
&= (\overline{S^u U_L})S^u M^u T^{u\dagger}(T^u U_R) + (\overline{S^d D_L})S^d M^d T^{d\dagger}(T^d D_R) \\
&\quad + (\overline{S^e E_L})S^e M^e T^{e\dagger}(T^e E_R) + h.c. \\
&= \sum_i \left[m_i^u(\bar{u}'_{Li}u'_{Ri} + \bar{u}'_{Ri}u'_L) + m_i^d(\bar{d}'_{Li}d'_{Ri} + \bar{d}'_{Ri}d'_L) + m_i^e(\bar{e}'_{Li}e'_{Ri} + \bar{e}'_{Ri}e'_L) \right],
\end{aligned}
\tag{2.18}
$$

where $U, D,$ and E are the weak eigenstates,

$$U = \begin{pmatrix} u \\ c \\ t \end{pmatrix}, D = \begin{pmatrix} d \\ s \\ b \end{pmatrix}, E = \begin{pmatrix} e \\ \mu \\ \tau \end{pmatrix}, \tag{2.19}$$

and we determine the mass eigenstate as

$$u'_{Li} \equiv \sum_j S^u_{ij} u_{Lj}, \quad d'_{Li} \equiv \sum_j S^d_{ij} d_{Lj}, \quad e'_{Li} \equiv \sum_j S^e_{ij} e_{Lj}. \tag{2.20}$$

(2.10) shows that the electromagnetic interaction and neutral current interaction do not change their form under the transformation of the mass eigenstate to the weak eigenstate, but charged current interaction by $W^{\pm}$ bosons change the picture. In the quark sector, charged current interaction term can be written by

$$\begin{aligned} -\frac{\sqrt{2}}{g}\mathcal{L}_{cc,q} &= \overline{U}_L \gamma^\mu D_L W^+_\mu + h.c. \\ &= \overline{U'}_L \gamma^\mu (S^u S^{d\dagger}) D'_L W^+_\mu + h.c. \\ &= \sum_{i,j} \left[\bar{u}'_{Li} \gamma^\mu V_{ij} d'_{Lj} W^+_\mu + \bar{d}'_{Li} \gamma^\mu V^*_{ij} u_{Lj} W^-_\mu \right] \end{aligned} \tag{2.21}$$

where $V \equiv S^u S^{d\dagger}$ is the Kobayashi-Maskawa matrix[2]. This matrix produces cross-generation mixing connecting flavor eigenstate $\tilde{d}$ to mass eigenstate d',

$$\tilde{d}_{Li} = \sum_j V_{ij} d'_{Lj}. \tag{2.22}$$

The 3×3 unitary matrix has 9 independent parameters. Three of them are rotation angle and the remaining six are the phases whose five can be absorbed by redefinition of quark fields. Therefore, the Kobayashi-Maskawa matrix has the unique complex phase and the KM phase gives rise to CP violating effects[2]. Note that if the fermions are massless, the rotation by S and T makes no sense.

If the neutrinos have their masses the lepton sector has similar structure as quark sector

$$\tilde{\nu}_i = \sum_j (S^{e\dagger} S^\nu)_{ij} \nu'_j. \tag{2.23}$$

In what follows, considering the massive neutrinos we discuss the neutrino oscillation.

2.2 Neutrino mixing and oscillation

If neutrinos have masses, generally the flavor eigenstates can be expressed by superposition of the mass eigenstates. Introducing Maki-Nakagawa-Sakata unitary matrix[3], $U \equiv S^{e\dagger} S^\nu$, the flavor eigenstate can be written by the mass eigenstate as

$$|\nu_\alpha\rangle = \sum_i U^*_{\alpha i} |\nu_i\rangle. \tag{2.24}$$

Where $\alpha = e, \mu, \nu$ and $i = 1, 2, 3$. This relation immediately derive the expression of the mass eigenstate

$$|\nu_i\rangle = \sum_\alpha U_{\alpha i} |\nu_\alpha\rangle. \qquad (2.25)$$

The unitary matrix $U(N \times N)$ has N^2 parameters, $\frac{1}{2}N(N-1)$ rotation angles and $\frac{1}{2}N(N+1)$ phases. If neutrinos are Dirac particle, $2N-1$ of phases are unphysical by phase redefinition of fermion field. On the other hand, if neutrinos are Majorana particle, only N of phases can be subtracted because the neutrino and anti-neutrino have to be identical. Thus U in Eq.(2.24) has three real mixing parameter and one complex phase for Dirac neutrino and two more phases for Majorana neutrino. We use standard parameterization for this matrix,

$$
\begin{aligned}
U &= \begin{pmatrix} 1 & 0 & 0 \\ 0 & c_{23} & s_{23} \\ 0 & -s_{23} & c_{23} \end{pmatrix} \begin{pmatrix} c_{13} & 0 & s_{13}e^{-i\delta} \\ 0 & 1 & 0 \\ -s_{13}e^{i\delta} & 0 & c_{13} \end{pmatrix} \begin{pmatrix} c_{12} & s_{12} & 0 \\ -s_{12} & c_{12} & 0 \\ 0 & 0 & 1 \end{pmatrix} \Gamma \\
&= \begin{pmatrix} c_{12}c_{13} & s_{12}c_{13} & s_{13}e^{-i\delta} \\ -s_{12}c_{23} - c_{12}s_{23}s_{13}e^{-i\delta} & c_{12}c_{23} - s_{12}s_{23}s_{13}e^{i\delta} & s_{23}c_{13} \\ s_{12}s_{23} - c_{12}c_{23}s_{13}e^{i\delta} & -c_{12}s_{23} - s_{12}c_{23}s_{13}e^{i\delta} & c_{23}c_{13} \end{pmatrix} \Gamma,
\end{aligned} \qquad (2.26)
$$

where $s_{ij} \equiv \sin\theta_{ij}, c_{ij} \equiv \cos\theta_{ij}$ and $\Gamma \equiv \mathrm{diag}(e^{i\frac{\alpha_1}{2}}, e^{i\frac{\alpha_2}{2}}, 1)$ exists only the case neutrinos are Majorana particle.

2.2.1 Neutrino oscillation in vacuum

Considering the propagation equation of mass eigenstates of neutrinos

$$
\begin{aligned}
i\frac{\partial}{\partial t}|\nu_i\rangle &= E_i|\nu_i\rangle \\
&\simeq \left(p + \frac{m_i^2}{2p}\right)|\nu_i\rangle,
\end{aligned} \qquad (2.27)
$$

where we use the assumption that neutrinos are ultra-relativistic to obtain the second line.

Using the relationship of mass eigenstates and flavor eigenstates Eq.(2.24)(2.25), one can obtain the propagation equation of flavor eigenstates,

$$
\begin{aligned}
i\frac{\partial}{\partial t}|\nu_\alpha\rangle &= \sum_\beta \sum_i U_{\alpha i}^* E_i U_{\beta i} |\nu_\beta\rangle \qquad (2.28) \\
&= H_{\alpha\beta}^{\mathrm{vac}*} |\nu_\beta\rangle. \qquad (2.29)
\end{aligned}
$$

In order to obtain the neutrino flavor eigenstate $|\nu_\alpha\rangle$ after the propagation for a distance

L, we solve the Eq.(2.27) with $t \to L$,

$$
\begin{aligned}
|\nu_\alpha(L)\rangle &= \sum_i U_{\alpha i}^* |\nu_i(L)\rangle \\
&= \sum_i U_{\alpha i}^* e^{-iEL} e^{-i\frac{m_i^2 L}{2E}} |\nu_i(0)\rangle \\
&= \sum_i \sum_\beta e^{-iEL} U_{\alpha i}^* e^{-i\frac{m_i^2 L}{2E}} U_{\beta i} |\nu_\beta\rangle
\end{aligned}
$$

where we have used $p \simeq E$ under the ultra-relativistic approximation.

Therefore it gives us the amplitude of flavor changing $\nu_\alpha \to \nu_\beta$

$$
A(\nu_\alpha \to \nu_\beta) = \sum_i e^{-iEL} U_{\alpha i}^* e^{-i\frac{m_i^2 L}{2E}} U_{\beta i}. \tag{2.30}
$$

We obtain the absolute square of the amplitude which describe the neutrino oscillation probability in vacuum by using the unitarity of the mixing matrix, ,

$$
\begin{aligned}
P(\nu_\alpha \to \nu_\beta) &= |A(\nu_\alpha \to \nu_\beta)|^2 \\
&= |\sum_i U_{\alpha i}^* e^{-i\frac{m_i^2}{2E}} U_{\beta i}|^2 \\
&= \delta_{\alpha\beta} - 4 \sum_{i>j} \mathrm{Re}(U_{\alpha i}^* U_{\beta i} U_{\alpha j} U_{\beta j}^*) \sin^2\left(\frac{\Delta m_{ij}^2 L}{4E}\right) \\
&\quad + 2 \sum_{i>j} \mathrm{Im}(U_{\alpha i}^* U_{\beta i} U_{\alpha j} U_{\beta j}^*) \sin\left(\frac{\Delta m_{ij}^2 L}{2E}\right), \tag{2.31}
\end{aligned}
$$

where $\Delta m_{ij}^2 \equiv m_i^2 - m_j^2$.

Note that $\mathrm{Im}(U_{\alpha i}^* U_{\beta i} U_{\alpha j} U_{\beta j}^*)$ is proportional to $\sin\delta$, the sign of it differs between neutrino and anti-neutrino. Therefore, it describes the CP-violating effect in neutrino oscillation. It is the lepton analogue of the Jarlskog factor [4], all the $|\mathrm{Im}(U_{\alpha i}^* U_{\beta i} U_{\alpha j} U_{\beta j}^*)|$ in $\alpha \neq \beta, i \neq j$ can be written by $J = c_{13}^2 s_{13} c_{12} s_{12} c_{23} s_{23} \sin\delta$.

In the case of two generation neutrinos the mixing matrix is given by 2×2 matrix with angle θ,

$$
\begin{pmatrix} \nu_\alpha \\ \nu_\beta \end{pmatrix} = \begin{pmatrix} \cos\theta & \sin\theta \\ -\sin\theta & \cos\theta \end{pmatrix} \begin{pmatrix} \nu_1 \\ \nu_2 \end{pmatrix}. \tag{2.32}
$$

The oscillation probability can be written as

$$
\begin{aligned}
P(\nu_\alpha \to \nu_\beta) &= \sin^2 2\theta \sin^2\left(\frac{\Delta m_{12}^2 L}{4E}\right), \quad (\alpha \neq \beta) \\
P(\nu_\alpha \to \nu_\alpha) &= 1 - \sin^2 2\theta \sin^2\left(\frac{\Delta m_{12}^2 L}{4E}\right) \tag{2.33}
\end{aligned}
$$

11

As we shall discuss later, two generation approximation formula is convenient for simple understanding of the basic features of the neutrino oscillations in nature.

At the end of this subsection, we summarize the values of oscillation parameters from Particle Data Group[7].

$$
\begin{align}
\sin^2(2\theta_{12}) &= 0.87 \pm 0.03 \tag{2.34} \\
\Delta m_{21}^2 &= (7.59 \pm 0.20) \times 10^{-5} eV^2 \tag{2.35} \\
\sin^2(2\theta_{23}) &> 0.92, \quad \text{CL} = 90\% \tag{2.36} \\
|\Delta m_{32}^2| &= (2.43 \pm 0.13) \times 10^{-3} eV^2 \tag{2.37} \\
\sin^2(2\theta_{13}) &< 0.19, \quad \text{CL} = 90\% \tag{2.38}
\end{align}
$$

The absolute value sign of (2.37) indicates that it is not yet determined whether $m_3 > m_2$ (normal mass hierarchy) or $m_3 < m_2$ (inverted mass hierarchy). Other parameters, complex phases δ, α_1, and α_2, have no constraint from any experiments.

2.2.2 Neutrino oscillation probability in matter

We have discussed neutrino oscillation in vacuum in a previous subsection. When neutrinos propagate in matter however, flavor changing probability is modified from the one in vacuum. It is known as the Mikheev-Smirnov-Wolfenstein (MSW)[5, 6] effect.

The electron neutrinos interact with electron by exchanging W boson in matter (Fig. 2.1). The effective Hamiltonian of the interaction is
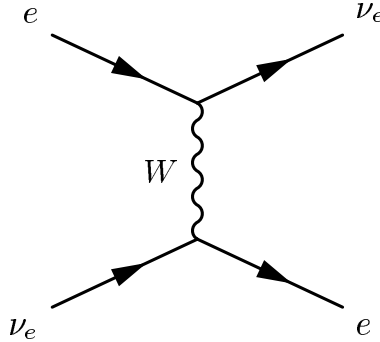
Figure 2.1: Feynman diagram of charged current interaction of electron with electron neutrino.

$$
H = \frac{G_F}{\sqrt{2}} \bar{\nu}_e \gamma^\mu (1 - \gamma_5) \nu_e \bar{e} \gamma_\mu (1 - \gamma_5) e, \tag{2.39}
$$

where G_F is the Fermi constant. In the rest frame of electrons, expectation value of electron term can be understood as

$$
\langle \bar{e} \gamma_\mu e \rangle = \delta_{0\mu} n_e, \tag{2.40}
$$

where n_e is electron number density in matter. An electron neutrino feels the effective potential from the coherent forward scattering. Because matter consist of electrons and nucleons, we do not have to consider the $\mu - \nu_\mu$ or $\tau - \nu_\tau$ coherent scattering. Therefore the Hamiltonian of neutrino propagation equation is written by

$$
\begin{aligned}
H_{\text{matt}} &= H_{\text{vac}} + \text{diag}(a, 0, 0) \\
&= U \frac{1}{2E} \begin{pmatrix} 0 & 0 & 0 \\ 0 & \Delta m_{21}^2 & 0 \\ 0 & 0 & \Delta m_{31}^2 \end{pmatrix} U^{-1} + \begin{pmatrix} a & 0 & 0 \\ 0 & 0 & 0 \\ 0 & 0 & 0 \end{pmatrix}, \\
a &= \sqrt{2} G_F n_e.
\end{aligned}
\tag{2.41}
$$

The Hamiltonian of anti-neutrino have a similar form of potential but with opposite sign, $-a$, by taking the CP-conjugate of ν_e in (2.39). Of course, the neutral-current interactions with matter produce a similar effective potential, but in a form proportional to identity matrix in the Hamiltonian. However, the term can be absorbed into the phase of the wave function, and it does not change the probability of flavor transition. Therefore, it can be safely ignored if we discuss flavor transformation.

In order to understand the solar neutrino discussed next chapter, let us review the theoretical outline of the solar neutrino oscillation in two generation neutrinos.

The effective mixing angle with effective eigenvalues $\tilde{\lambda}_1(x), \tilde{\lambda}_2(x)$ in matter can be written as

$$
\begin{aligned}
\tilde{U}(x) &= \begin{pmatrix} \cos \tilde{\theta}(x) & \sin \tilde{\theta}(x) \\ -\sin \tilde{\theta}(x) & \cos \tilde{\theta}(x) \end{pmatrix}, \\
\tan 2\tilde{\theta}(x) &= \frac{\Delta \sin 2\theta}{\Delta \cos 2\theta - a(x)}
\end{aligned}
\tag{2.42}
$$

where $a(x) \equiv \sqrt{2} G_F n_e(x)$, $n_e(x)$ is the electron number density in the sum depending on the depth, $\Delta = \frac{\Delta m_{21}^2}{2E}$, and θ is mixing angle at vacuum. The important point is that the effective mixing angle can be maximal at the resonance point $a(x) = \Delta \cos 2\theta$. Note that the matter effect changes significantly while neutrinos propagate in the sun, it makes the effective mixing angle depend on distance which dependence cut into a diagonalized evolution equations like

$$
i \frac{\partial}{\partial x} \begin{pmatrix} \nu_1 \\ \nu_2 \end{pmatrix} = \left(\text{diag} \left(\frac{\tilde{\lambda}_1(x)}{2E}, \frac{\tilde{\lambda}_2(x)}{2E} \right) - i \tilde{U}^{-1}(x) \frac{\partial \tilde{U}(x)}{\partial x} \right) \begin{pmatrix} \nu_1 \\ \nu_2 \end{pmatrix}.
\tag{2.43}
$$

The extra term is written by

$$
\tilde{U}^{-1}(x) \frac{\partial \tilde{U}(x)}{\partial x} = \begin{pmatrix} 0 & \frac{\partial \tilde{\theta}(x)}{\partial x} \\ -\frac{\partial \tilde{\theta}(x)}{\partial x} & 0 \end{pmatrix}.
\tag{2.44}
$$

Using (2.42), the time dependence of the effective mixing angle is given as

$$
\frac{\partial \tilde{\theta}(x)}{\partial x} = \frac{\sin^2 2\tilde{\theta}(x)}{2\Delta \sin 2\theta} \frac{\partial a(x)}{\partial x}.
\tag{2.45}
$$

If the off-diagonal element is sufficiently small compared with diagonal element even at the resonance point, the adiabatic condition is satisfied and we can solve the equation. The adiabatic condition are written by

$$\left| \frac{\partial \tilde{\theta}(x)}{\partial x} \right| \ll |\tilde{\Delta}(x)|, \tag{2.46}$$

where $\tilde{\Delta}(x) = \frac{\tilde{\lambda}_2(x) - \tilde{\lambda}_1(x)}{2E}$, and at the resonance point, it is given as

$$\left| \frac{\Delta \sin^2 2\theta}{\cos 2\theta} \frac{a}{\dot{a}} \right|_{\text{resonance}} \gg 1. \tag{2.47}$$

where $\dot{a} = \frac{\partial a(x)}{\partial x}$.

Suppose that the neutrinos are produced at production point x_p. The electron neutrino state on the solar surface L can be written as

$$|\nu_e(L)\rangle = \sum_i \sum_\alpha U_{ei}(L) e^{-i \int_{x_p}^{L} \tilde{\lambda}_i(x) dx} \tilde{U}_{\alpha i}^*(x_p) |\nu_\alpha(x_p)\rangle. \tag{2.48}$$

Thus, the survival probability of the electron neutrinos is written by

$$P(\nu_e \to \nu_e) = \cos^2 \theta \cos^2 \theta_N + \sin^2 \theta \sin^2 \theta_N + \frac{1}{2} \sin 2\theta \sin 2\theta_N \cos \int_{x_p}^{L} \tilde{\Delta}(x) dx \tag{2.49}$$

where $\theta_N = \tilde{\theta}(x_p)$ and we use $U(L)$ is the mixing matrix in vacuum. If the oscillation length of the third term of (2.49) is sufficiently short compare to propagation length, averaging over the production position cancels out the term. Assuming the matter effect at production point is sufficiently large as $\theta_N \simeq \pi/2$, the conclusive survival probability can be written as

$$P_{\text{survival}} \equiv P(\nu_e \to \nu_e) = \sin^2 \theta. \tag{2.50}$$

If neutrino energy is small as $\frac{\Delta m_{31}^2}{2a} \cos 2\theta \gg E$ we can approximate $\theta_N = \theta$. Therefore, the survival probability can be approximated by vacuum oscillation

$$P_{\text{survival}} = 1 - \frac{1}{2} \sin^2 2\theta. \tag{2.51}$$

2.3 Search for neutrino mass

The oscillation experiments successfully measured the difference of mass squared of neutrinos. By contrast, there is no successful experiments measuring the absolute mass of neutrino.

In this section, we would like to show the constraints of absolute neutrino masses from various experiments.

2.3.1 Direct measurement experiments of neutrino mass

The "direct" constraint of the neutrino mass is given as

$$m(\nu_e) \leq 2\text{eV}, \tag{2.52}$$

by the evaluation of Particle Data Group[7].

This constraint comes from the measurement of tritium beta decay. The decay rate Γ of beta decay can be written by

$$d\Gamma \propto F(Z, E)pEp_\nu E_\nu dE \tag{2.53}$$

where E and p is the electron energy and momentum respectively, E_ν and p_ν is the neutrino energy and momentum, and $F(Z, E)$ is the effect of Coulomb field. If we determine the Kurie plot function $K(E)$ as

$$K(E) \equiv \sqrt{\frac{d\Gamma/dE}{F(Z, E)pE}}, \tag{2.54}$$

it is proportional to $(E_0 - E)$ on massless neutrino where E_0 is the mass difference of nuclei before and after decay. But in the case of massive neutrino, the highest energy tail of spectrum can not reach E_0 but $E_0 - m_\nu$. Therefore, in principle, the precise measurement of electron energy spectrum at highest energy tells us the absolute mass of neutrino (See Fig. 2.2).
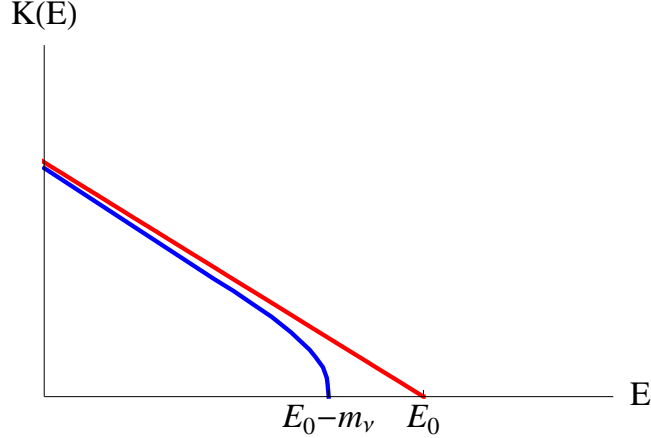
Figure 2.2: The Fermi-Kurie plot. The red line is given by massless neutrino and the blue line for massive neutrino.

There is a lot of experiments using ^{3}T beta decay[9]. The strongest constraint which by the Mainz neutrino mass search is

$$m(\nu_e) \leq 2.3\text{eV} \quad (95\%CL.). \tag{2.55}$$

15

A future experiment with the same method which is expected to reach the highest sensitivity to neutrino mass is KATRIN (KArlsruhe TRItium Neutrino experiment) [10], has a great discovery potential

$$m > 0.35 \text{eV} \tag{2.56}$$

in 5σ significance.

2.3.2 Cosmological constraint on neutrino masses

The cosmological observations have also the constraint on neutrino masses.

Tracing back through the history of universe, neutrinos had been in thermal equilibrium at the early time. As the universe cooled down with expansion, neutrinos are decoupled from equilibrium. After decoupling neutrinos further cooled down and today they are believed to remain as 1.96K cosmic neutrino background similar to CMB. The neutrino oscillation experiments shows the information of difference of mass square, it tells us that sum of three generation neutrino masses are limited as

$$\sum_i m_i \gtrsim 0.06(0.09) \text{ eV} \tag{2.57}$$

for the normal (inverted) hierarchy. This lower bound means that the cosmic neutrino background are non-relativistic and current matter density of universe Ω_m contains mass of neutrinos.

On the other hand, neutrinos ware relativistic in the decoupling epoch. It means that the matter density at the decoupling epoch was smaller than the one which is calculated with massless neutrinos. Changing the matter to radiation ratio at the decoupling epoch accelerate the decay of gravitational potential around the decoupling epoch. Finally, it modifies the power spectrum of CMB as integrated Sachs-Wolfe(ISW) effect.

The 5 year measurement of the Wilkinson Microwave Anisotropy Probe(WMAP) gives us [11]

$$\sum_i m_i < 1.3 \text{ eV} (95 \text{ \% CL}). \tag{2.58}$$

Furthermore, because mass of neutrinos affects the large scale structure of the universe, there is stronger constraint by combining the Lyman-α and other observations [12]

$$\sum_i m_i < 0.17 \text{ eV} (95 \text{ \% CL}). \tag{2.59}$$

But note that the systematic uncertainty of Lyman-α is not well understood.

It is important that this type of constraints from cosmological observations may be able to determine the hierarchy of neutrinos. The Fig. 2.3 shows the plot of sum of neutrino masses with the lightest neutrino mass as horizontal axis, blue line with normal hierarchy and red line with inverted one. One can realize that if upper bound of sum of neutrino masses reaches less than 0.09 eV with sufficient accuracy, it can conclude the neutrino mass hierarchy is the normal one.
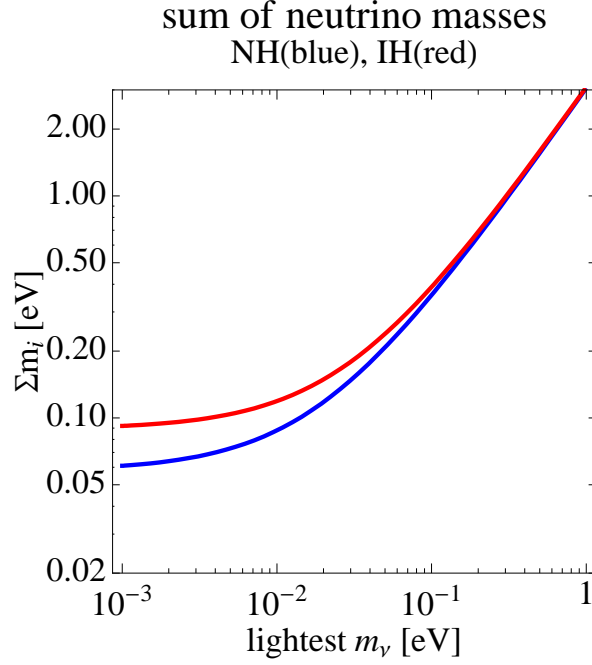
Figure 2.3: The sum of neutrino masses : $\sum_i m_i$. The lightest neutrino is ν_1 for normal hierarchy (blue line) or ν_3 for inverted hierarchy (red line).

2.3.3 Neutrinoless double beta decay experiments

Considering the neutrino masses, one possible form is Dirac mass term as

$$\overline{\nu_R} m_D \nu_L \tag{2.60}$$

where ν_R is new particle but not conflict with the standard model.

By contrast, because neutrinos do not have electric charge neutrinos can be anti-particle of themselves, symbolically $\bar{\nu} = \nu$. Thus there is another possible mass form

$$\overline{(\nu_L)^C} M \nu_L. \tag{2.61}$$

It is the Majorana mass term.

If neutrinos are Majorana particle, neutrinoless double beta decay $(0\nu\beta\beta)$

$$(A, Z) \rightarrow (A, Z+2) + 2e^- \tag{2.62}$$

can occur where (A, Z) is a nucleus consists of Z protons and (A-Z) neutrons if single beta decay is forbidden by kinematics. Note that this process does not conserve lepton number. The main contribution to neutrinoless double beta decay can be understood as Fig. 2.4. This process never happen on Dirac neutrino $\bar{\nu} \neq \nu$.

The half life time of this process is given by

$$(T_{1/2}^{0\nu})^{-1} = G_{0\nu}(Q_{\beta\beta}, Z)|M_{0\nu}|^2 \langle m_{\beta\beta} \rangle^2, \tag{2.63}$$

17
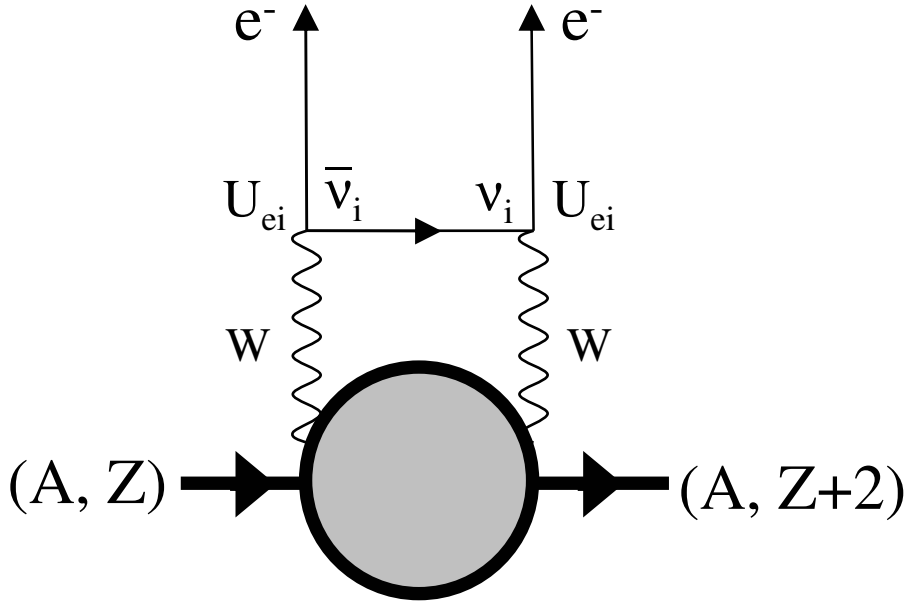
Figure 2.4: Diagram to neutrinoless double beta decay due to Majorana neutrino mass.

where $G_{0\nu}$ is the phase space factor and $M_{0\nu}(Q_{\beta\beta}, Z)$ is nuclear matrix element, and $\langle m_{\beta\beta} \rangle$ is the effective Majorana mass of the electron neutrino for neutrinoless double beta decay. Considering the diagram Fig. 2.4, effective mass is written by

$$\langle m_{\beta\beta} \rangle = \left| \sum_i m_i U_{ei}^2 \right|. \tag{2.64}$$

Fig. 2.5 plotted the effective Majorana mass (2.64) with best fit value of mixing parameters, (2.38), and $\sin^2 2\theta_{23} = 1$. Unknown parameters δ_1, α_2, and α_2 are varied and $\sin^2 2\theta_{13}$ is fix at either 0 or 0.1. One can realize that if the neutrino mass hierarchy is the normal one, there is a possibility that half life time of neutrinoless double beta decay is extremely small.

Many double beta decay experiments were carried out using varying nuclei and still many more are either ongoing or in planning stage. In this subsection we show the result of only one experiment which places strongest bound on the effective mass by the CUORI-CINO. The CUORICINO is an array of 62 bolometers of TeO_2 which tellurium is ^{130}Te with active mass of 40.7 kg. The measurement of an exposure of 11.83 kg · y gives [13]

$$T_{1/2}^{0\nu}(^{130}Te) \leq 3.0 \times 10^{23} \text{ year } (90\%CL), \tag{2.65}$$

in the form of effective mass,

$$\langle m_{\beta\beta} \rangle < (0.19 - 0.68) \text{ eV } (90\%CL) \tag{2.66}$$

where it contains the uncertainty in the nuclear matrix elements. For more results, see the table of PDG[15].

Meanwhile, there is a report of the discovery of the decay in 97% CL (2.2σ). Klapdor-Kleingrothaus et al.. They presented an interpretation of the data taken by the HEIDELBERG-MOSCOW double beta decay experiment which resulted in the claim that

$$T_{1/2}^{0\nu} = (0.8 - 18.3) \times 10^{25} \text{ year } (95\% CL) \tag{2.67}$$

with the best fit value of 1.5×10^{25} y [14]. In terms of effective Majorana mass, it is

$$\langle m_{\beta\beta} \rangle = (0.11 - 0.56) \text{ eV } (95\% CL) \tag{2.68}$$

with the best fit value of 0.39 eV. But this report received critical comments from other researchers[15] and the result is not confirmed by the other experiments.
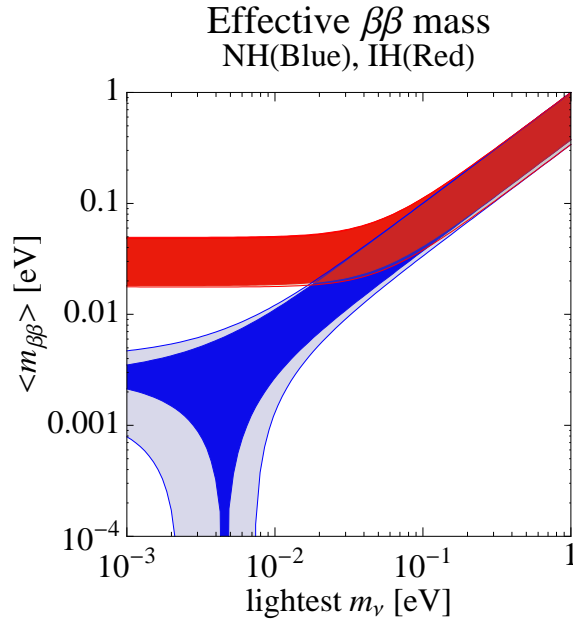
Figure 2.5: Effective Majorana mass which can be observed by neutrinoless double beta decay is plotted as a function of the lightest mass of neutrinos. The region was made by varying the complex phases δ_1, α_1, and α_2. The deep(pale) blue region is for the normal hierarchy for $\sin^2 2\theta_{13} = 0(0.1)$. The deep(pale) red region is for the inverted hierarchy for $\sin^2 2\theta_{13} = 0(0.1)$.

Chapter 3

Neutrino Oscillation Experiments

In this chapter, we review the various neutrino oscillation experiments which determine the oscillation parameters. First, the atmospheric neutrino experiments and accelerator neutrino experiments for the determination of 2-3 sector of the mixing matrix. Next, the solar neutrino experiments and KamLAND experiment for 1-2 sector. At last, the reactor experiments which have the constraint on the element of 1-3 sector.

3.1 Atmospheric scale neutrino oscillation experiments

The atmospheric neutrinos are created during passage of cosmic ray in the atmosphere. Main process of creating the neutrinos is pion decay

$$
\begin{aligned}
\pi^+ &\rightarrow \mu^+ + \nu_\mu \\
&\rightarrow e^+ + \nu_e + \bar{\nu}_\mu + \nu_\mu, \\
\pi^- &\rightarrow \mu^- + \bar{\nu}_\mu \\
&\rightarrow e^- + \bar{\nu}_e + \nu_\mu + \bar{\nu}_\mu.
\end{aligned}
\tag{3.1}
$$

which are produced by interaction of cosmic ray protons and ^{4}He with nuclei in the atmosphere.

Therefore, ignoring distinction of neutrino and anti-neutrino, if muon energy is sufficiently small to decay in the atmosphere the ratio of number of muon neutrino and electron neutrino, $N(\nu_\mu + \bar{\nu}_\mu)/N(\nu_e + \bar{\nu}_e)$, is 2. However, the measurement by Kamiokande showed that it is clearly smaller than 2 [16][17].

In this section, we review the atmospheric neutrino oscillation and its confirmation experiments using accelerator neutrino beam.

3.1.1 Super-Kamiokande

In 1998, the Super-Kamiokande (Super-KAMIOKA Nucleon Decay Experiment or Neutrino Detection Experiment) reported conclusive evidence of the neutrino oscillation at the atmospheric neutrinos[18].

The Super-Kamiokande (SK) is a water Cherenkov detector of total mass of 50 kton, inner 22.5 kton is used for fiducial mass. Both electrons and muons which produced by

the neutrino reactions leave behind the Cherenkov light ring to the SK's photomultiplier. While muons create relatively clear circle, electron's Cherenkov rings have more "irregular" shape because of multiple scattering of electrons in water. Therefore it allows differentiation between the event of electron-neutrinos and muon-neutrinos. The efficiency for identifying quasi-elastic $\nu_e(\nu_\mu)$ events as single-ring was 93.2(95.8)%, and the angular resolution for these events was 3.0° and 1.8° for e-like and μ-like events respectively.[19]

The Fig. 3.1 shows the atmospheric neutrino events observed by SK (black circle) assigning zenith angle at horizontal axis with $\cos\theta_z = 1$ for zenith and $\cos\theta_z = -1$ for nadir. The left panels are the plot of electron-like events and the right panels are muon-like events. The blue boxes are the expected events without neutrino flavor transition. One can realize that unlike the no dependence on the zenith angle at e-like events, the longer propagation of neutrinos, the more mismatch between the data and the Monte Carlo expectation exists in μ-like events. It can be understood that while downward-going ν_μ cannot change their flavor because of short distance ($\sim O(10)$ km), upward-going ν_μ oscillate to ν_τ in propagating through the earth ($L \sim O(10000)$ km).
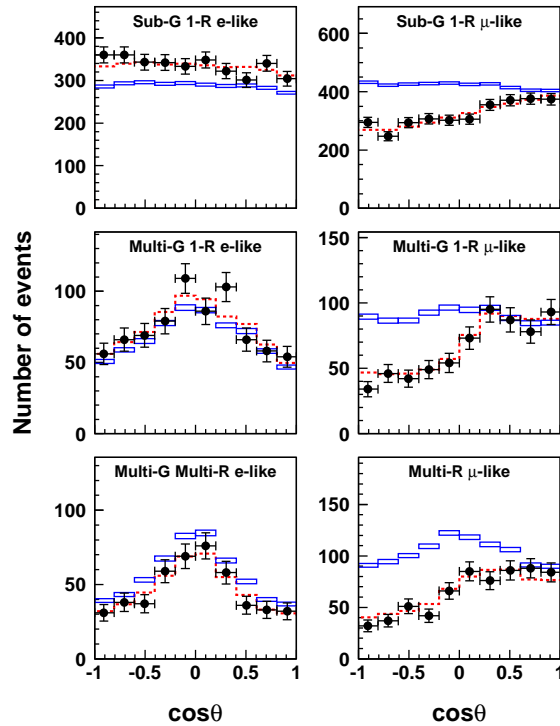
Figure 3.1: Zenith angle distributions of electron-like(left) and muon-like(right) event data(black circle). $\cos\theta = 1$ corresponds to the direction from zenith. Monte Carlo estimation without oscillation(blue box) and best-fit with oscillation(red dashed). This figure is taken from [20]

The survival probability of $\nu_\mu \rightarrow \nu_\mu$ with $\nu_\mu - \nu_\tau$ two generation oscillation can be written as

$$P(\nu_\mu \rightarrow \nu_\mu) = 1 - \sin^2 2\theta \sin^2 \left(\frac{\Delta m^2 L}{4E} \right). \tag{3.2}$$

The two generation formula gives a reasonably good approximation because θ_{13} is small as we will discuss later. The result of SK indicated that mixing angle is large and $\Delta m^2 \sim O(10^{-3})\text{eV}^2$.

The SK group also worked on the analysis of a three-flavor oscillation[20]. The best-fit values of oscillation parameter are given as

$$
\begin{aligned}
\Delta m^2 &= 2.5 \times 10^{-3} \text{ eV}^2 & (3.3) \\
\sin^2 \theta_{23} &= 0.5 & (3.4) \\
\sin^2 \theta_{13} &= 0 & (3.5)
\end{aligned}
$$

with 90% confidence allowed regions of mixing angle,

$$
\begin{aligned}
0.37(0.37) < &\sin^2 \theta_{23} < 0.65(0.69) \\
&\sin^2 \theta_{13} < 0.14(0.27).
\end{aligned} \tag{3.6}
$$

with normal (inverted) hierarchy.

3.1.2   K2K

The K2K (KEK to Kamioka) experiment is the first long baseline experiment which was set up for confirmation of the neutrino oscillation observed by SK (atmospheric neutrinos). The ν_μ beam comes from π^+ decay which are produced by injecting 12 GeV proton beam on target at KEK. The averaged energy of neutrinos is approximately 1.3 GeV. The flux and the energy spectrum of neutrino beam are measured by the near detector which consists of 1 kton water Cherenkov detector and a fine-grained detector system.

The disappearance probability of ν_μ was measured by SK which is located at the distance of 250 km from KEK. Considering the value of L/E of this experiment, the K2K have a good sensitivity to the mass squared difference $\Delta m^2 \simeq 6 \times 10^{-3}\text{eV}^2$ which is similar to the value of atmospheric neutrino oscillation's.

The focus event is one ring μ like event produced by the charged-current quasi elastic scattering $\nu_\mu + n \rightarrow \mu^- + p$, because it allow us to calculate the parent neutrino energy from the muon kinematics. The crucial point of the long baseline experiment is that the events which come from neutrino beam interaction in water can be distinguished from the non beam-induced event by the timing synchronization to beam bunch using the GPS.

The result of μ like events is consistent with SK[21]. The oscillation parameters are given as

$$
\begin{aligned}
\sin^2 2\theta_{13} &= 1.0, \\
\Delta m^2 &= 2.8 \times 10^{-3}\text{eV}^2
\end{aligned} \tag{3.7}
$$

with the allowed Δm^2 region of $(1.9 - 3.5) \times 10^{-3}\text{eV}^2$ at the 90% CL.[22].

Fig. 3.2 shows the observed E_ν distribution. The K2K obtained the evidence of the neutrino oscillation in 4.3σ.
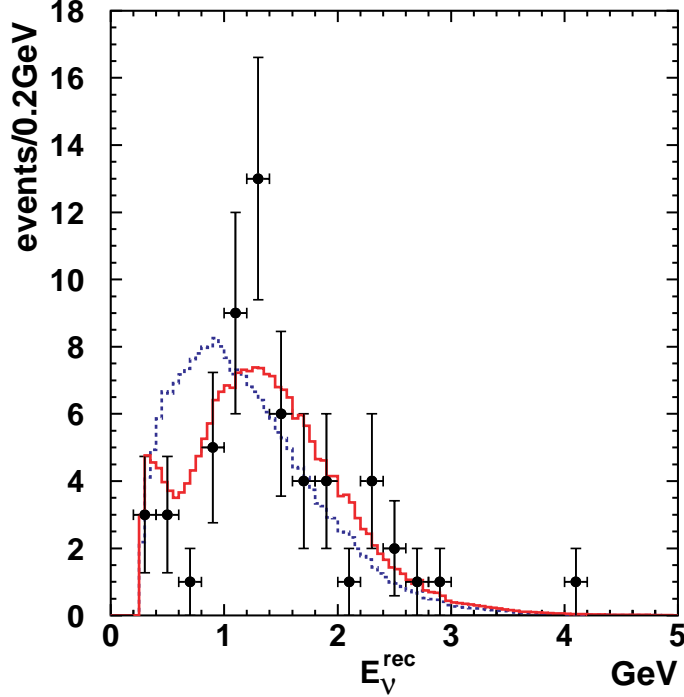
Figure 3.2: The reconstructed spectrum for the 1-ring μ-like sample. Points with error bars are date. The red solid line is the best fit spectrum with neutrino oscillation and the blue dashed line is the expectation without oscillation. This figure is taken from [22]

3.1.3 MINOS

The MINOS (Main Injector Neutrino Oscillation Search) experiment is also the long baseline experiment for confirmation of the atmospheric neutrino oscillation phenomenon. MINOS measures the ν_μ beam coming from the Fermilab at Soudan mine, 735 km away from the production point.

The ν_μ beam is produced by NuMI (Neutrinos at the Main Injector) at the Fermilab. The protons accelerated to 120 GeV by Main Injector hit the target and produce the pions. The pions are focused by the horns in order to obtain collimated π^+ beam which then decay during flight in 675 m decay pipe. The neutrino beam is comprised of 91.8% ν_μ, 6.9% $\bar{\nu}_\mu$ and 1.3% $\nu_e + \bar{\nu}_e$. The advantage point of the MuMI beam is that energy spectrum can be modified by varying the relative position of target and the horns. Basically, low energy configuration, the peak energy is $\simeq 3$ GeV at on-axis, are set for precise determination of Δm^2.

MINOS has the near and the far detectors both of which have the same steel/scintillator layered structure. The detectors have 1 kton total mass at the near site and 5.4 kton total mass at the far site. The focus event is caused by charged-current interaction,

$$\nu_\mu + N \rightarrow \mu^- + N'. \tag{3.8}$$

A muon leaves a long clean track in the detector and there is a hadronic activity at the

23

vertex. Fig. 3.3 shows the energy spectrum of ν_μ event and predicted energy spectrum of ν_μ with and without oscillation.
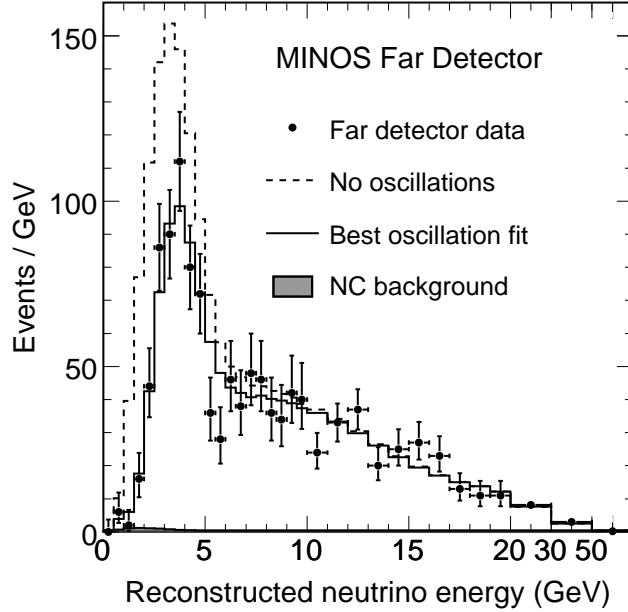
Figure 3.3: The comparison of the far detector data with the prediction of ν_μ spectrum w/ and w/o oscillation. This figure is taken from [23]

The MINOS experiment carried out a precise measurement of Δm^2[23]

$$|\Delta m^2| = (2.43 \pm 0.13) \times 10^{-3} \text{ eV}^2, \tag{3.9}$$

and bound of $\sin^2 2\theta$ as

$$\sin^2 2\theta > 0.90(90\% CL.). \tag{3.10}$$

Those results are consistent with the ones obtained by SK and K2K.

MINOS also measure the events of electron neutrinos appearance in parallel. The ν_e charged-current interaction event produce the electron which has short track and typical EM shower profile in the detector. The appearance probability of electron neutrino are given as (5.29) which depends on $\sin^2 2\theta_{13}$. The recent result of this observation is 35 events with a background of 27 ± 5(stat.) ± 2(syst.)[24]. This is consistent with the value of $\sin^2 2\theta_{13}$ comparable to the CHOOZ limit which will be discussed later.

3.2 Solar scale neutrino oscillation experiments

The sun is shining and emitting neutrinos by nuclear fusion reaction. The reaction network contains ppI, ppII, ppIII chain reactions, the net reaction is very simple,

$$4p^+ \rightarrow {}^4\text{He}^{2+} + 2e^+ + 2\nu_e + \gamma's, \tag{3.11}$$
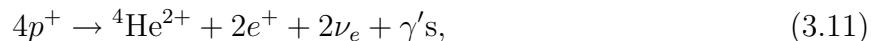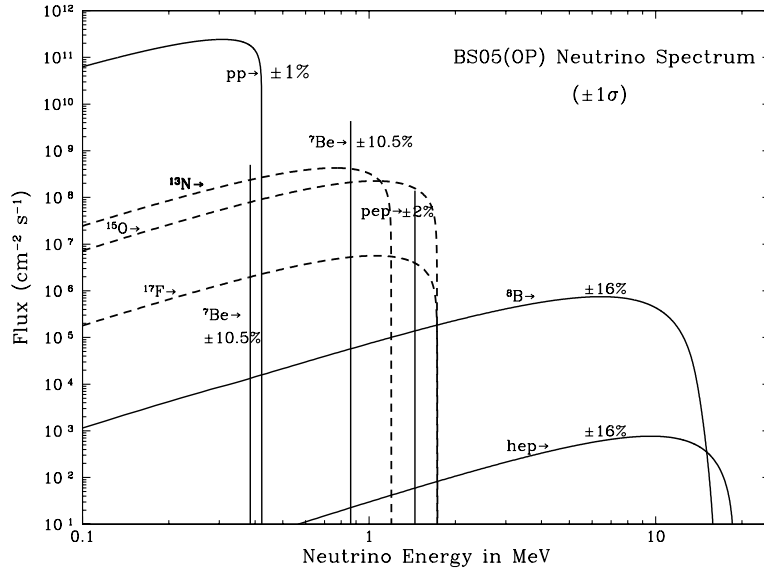
Figure 3.4: The spectrum of ν_e fluxes from various reactions. This figure is taken from [25].

In Fig. 3.4 the neutrino energy spectra from these nuclear reactions calculated by the standard solar model (SSM) are presented.

In 1968, Davis et al. reported that they succeeded to detect solar electron neutrinos [26]. They used ^{37}Cl nucleus as target to detect the solar neutrinos. The reaction is

$$\nu_e + {}^{37}\text{Cl} \rightarrow {}^{37}\text{Ar} + e^-. \tag{3.12}$$

The threshold energy of this reaction is 0.814 MeV. The produced ^{37}Ar atoms, which do not exist in nature, are extracted by bubbling of He gas, and the Auger electrons are counted during a few times the life time of 35 days. The result showed that the flux of the solar neutrinos ν_e is less than the flux expected by the SSM.

In order to measure the solar neutrinos from ppI chain, the main engine of the sun, there are experiments using ^{71}Ga which reaction is

$$\nu_e + {}^{71}\text{Ga} \rightarrow {}^{71}\text{Ge} + e^-, \tag{3.13}$$
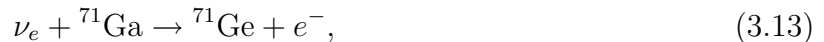
with $E_{\text{thresh}} \geq 0.233$ MeV. The deficit of solar neutrinos is stable throughout exposure of 35 years of ^{37}Cl experiments, which produced a serious problem called "the solar neutrino problem".

The SAGE(Soviet(Russian)-American Gallium Experiment)[28] reported their 7 years result

$$67.2^{+7.2+3.5}_{-7.0-3.0} \text{ SNU}, \tag{3.14}$$

where 1SNU(Solar Neutrino Unit)= 1capture/sec/10^{36}atoms. This is only about half of the predicted SSM rate of 129 SNU. Moreover, GALLEX (GALLium Experiment)[27] + GNO(Gallium Neutrino Observatory)[29] gave the result which is consistent with SAGE,

$$74.1^{+6.7}_{-6.8} \text{ SNU}. \tag{3.15}$$

25

The water Cherenkov detector Kamiokande [30] and Super-Kamiokande [31] have potential of observation of high-energy ($E_{\text{thresh}} \simeq 7 \sim 9$ MeV) solar neutrinos by elastic scattering process

$$\nu + e^- \rightarrow \nu + e^-. \tag{3.16}$$

SK measurement has a great advantage of determining the direction of neutrinos to know from where they come. It means that they can distinguish the solar neutrino events from the background. The results of experiments shows that the flux of the solar neutrinos on the Earth is 46 % of the expected flux.[32, 33]

3.2.1 SNO

SNO (Sudbury Neutrino Observatory) is the solar neutrino experiment using heavy water (D_2O) in Canada. It is able to confirm definitively the oscillation of solar neutrinos come from ^{8}B decay by measuring the three types of events

$$\nu_e + d \rightarrow e^- + 2p \tag{3.17}$$
$$\nu_x + d \rightarrow \nu_x + p + n \tag{3.18}$$
$$\nu_x + e^- \rightarrow \nu_x + e^-. \tag{3.19}$$

The first reaction is caused by the charged-current (CC) interaction is available only at SNO in the direct counting experiments. The CC event is observed by Cherenkov light of the emitted electron. The threshold energy $T_{\text{eff}} = 3.5$ MeV, thus we observe the survival electron neutrinos from ^{8}B decay in the sun.

The second reaction induced by neutral current (NC) can be initiated by all the flavors of neutrinos with the same rate. This process, $E_{\text{thresh}} = 2.2$ MeV, leave not only Cherenkov light but also a neutron which is captured by the deuteron and emit the 6.25 MeV gamma. Therefor SNO can observe not only ν_e but the total flux of solar neutrinos regardless of existence of the flavor transition. The observed ^{8}B flux is perfectly consistent with the prediction of SSM $\Phi_{\text{SSM}} = 5.05^{+1.01}_{-0.81}$ as[35]

$$\Phi_{^8\text{B}} = 5.046^{+0.159}_{-0.152}(\text{stat.})^{+0.107}_{-0.123}(\text{syst.}) \tag{3.20}$$

The final one is the elastic scattering (ES) process as we saw in SK.

The first result of NC event is reported in 2002[34]. It was nothing but direct evidence of neutrino flavor transition in 5.3σ due to the observation of non-ν_e flux

$$\phi_{\mu\tau} = 3.41 \pm 0.45(\text{stat.})^{+0.48}_{-0.45}(\text{syst.}) \times 10^6 \text{ cm}^{-2}\text{s}^{-1}. \tag{3.21}$$

Since the efficiency of neutron capture by deuteron is not large, the salt was added in the 2nd phase. Neutrons are mostly captured by ^{35}Cl with the average efficiency twice larger than that of deuterium. The events are recognized by characteristic signature of producing cascade of 2-3 gammas.

In the 3rd and the final phase, ^{3}He counters are installed which makes the threshold energy of detectable event lower significantly by

$$n + {}^3\text{He} \rightarrow p + \text{T} \tag{3.22}$$

with $Q = 0.76$ MeV and makes it possible to detect neutrinos event-by event. The best-fit point from the SNO is given as[35]

$$\Delta m^2 = 5.50 \times 10^{-5} \text{ eV}^2 \tag{3.23}$$
$$\tan^2 \theta = 0.457. \tag{3.24}$$

3.2.2 Borexino

The Borexino experiment is the first real-time experiment of observing low energy solar neutrinos. The Borexino have the detector of 278 ton of liquid scintillator which consists of pseudocumene doped with 1.5 g/liter of PPO in 2100 ton of ultra-pure water. The main target of observation is the low energy (0.862 MeV) ^{7}Be solar neutrinos which scatter with electrons as in (3.19). The energy of prompt electron can be measured by liquid scintillator.

There is the considerable background from ^{210}Po α which cover the broad energy region of expected event by ^{7}Be neutrinos. They have two methods to analyze this background. First, restricting the fit region between 560 MeV and 800 MeV to avoid the ^{210}Po peak. The second one is the subtraction of the ^{210}Po induced events by distinguishing α and β.

The event rate of the 0.862 MeV ^{7}Be solar neutrinos is measured to be [36]

$$49 \pm 3(\text{stat}) \pm 4(\text{syst})\text{event/day} \cdot 100 \text{ ton.} \tag{3.25}$$

This is inconsistent with the case of non-oscillated, expected ~ 75 event/day·100ton, at the 4σ CL.

3.2.3 KamLAND

KamLAND (Kamioka Liquid scintillator Anti-Neutrino Detector) has 1000 ton of liquid scintillator with composition of 80% Dodecane and 20% Pseudocumene.

Detection mechanism is different from solar neutrinos' because reactor neutrinos are electron anti-neutrinos undergo the reaction

$$\bar{\nu}_e + p \rightarrow e^+ + n. \tag{3.26}$$

In the liquid scintillator, the prompt positron immediately annihilate with electron and emit two gammas, the neutron is captured by free protons with mean capture time $\tau \sim 200$ μsec and emit 2.2 MeV gamma. This is called the delayed coincidence which allows clean detection of $\bar{\nu}_e$s, by which neutrinos are first discovered experimentally[39].

This experiment pinned down the correct parameter region of the MSW solution to be the LMA one, thereby finally settled the long-standing solar neutrino problem. The experiment measures the survival probability, $P(\bar{\nu}_e \rightarrow \bar{\nu}_e)$ whose expression is given using 2-flavor vacuum oscillation approximation as

$$P(\bar{\nu}_e \rightarrow \bar{\nu}_e) = 1 - \sin^2 2\theta \sin^2 \frac{\Delta m^2 L}{4E}. \tag{3.27}$$

KamLAND is in Kamioka site and there are nuclear power stations around it with average distance of $\simeq 180$ km. Because the energy of reactor neutrinos $\bar{\nu}_e$ is sub MeV, order 100

km is close to the first or the second oscillation maxima of solar Δm^2 oscillation

$$\frac{\Delta m_{sol}^2 L}{4E} \simeq \frac{\pi}{2} \text{ or } 3\frac{\pi}{2}. \tag{3.28}$$

Furthermore, we can obtain precise informations of the original flux of $\bar{\nu}_e$ from the reactors by using the data of electric power. Therefore one can, in principle, perform precision measurement of disappearance of $\bar{\nu}_e$ from reactors.

Fig. 3.5 is the most recent result of KamLAND with L_0/E as horizontal axis. L_0 is flux-weighted average distance of baseline, $L_0 = 180$ km. One can identify that there are two clean oscillation peaks.
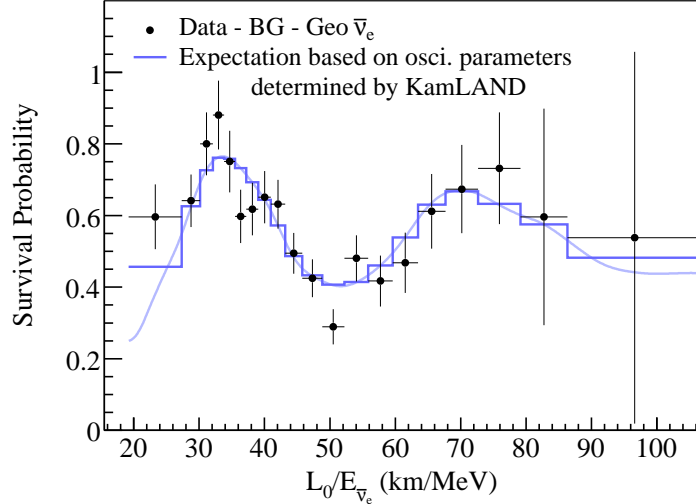
Figure 3.5: The KamLAND result (dot) which are subtracted BG and geo neutrinos as a function of L_0/E. Blue line is expectation of neutrino oscillation with best fit value of the KamLAND. L_0 is the effective baseline distance which determined by flux-weighted average, $L_0 = 180$ km. This figure is taken from [37].

KamLAND have a great sensitivity to the Δm_{21}^2 determination because of having the 2 cycles of oscillation. The recent result of the KamLAND measurement gives the values of the oscillation parameters as[37]

$$\Delta m_{21}^2 = 7.58_{-0.13}^{+0.14}(\text{stat})_{-0.15}^{+0.15}(\text{syst}) \times 10^{-5} \text{ eV}^2 \tag{3.29}$$

$$\tan^2 \theta_{12} = 0.56_{-0.07}^{+0.10}(\text{stat})_{-0.06}^{+0.10}(\text{syst}). \tag{3.30}$$

At low energies ($\lesssim 2.6$ MeV) the neutrino energy spectrum contains geo neutrinos coming from beta decay of ^{238}U and ^{232}Th in the earth. KamLAND also has potential of observe this type of neutrinos[38].

3.3 Reactor neutrino experiment

The CHOOZ experiment is the neutrino oscillation experiment using anti-electron neutrinos emitted from two reactors with a total thermal power of 8.5 GW at the Chooz village. The liquid scintillator detector contains a 5 ton of mineral oil loaded with Gadolinium.

The sub-MeV anti-electron neutrinos are detected via the inverse β-decay

$$\bar{\nu}_e + p \rightarrow e^+ + n. \tag{3.31}$$

The e^+ is detected by prompt signal which consists of the scintillation light and the annihilation γ. The neutron is captured by Gd which produces gamma rays of 8 MeV.

The baseline distances L from two reactors are about 1 km with small difference, $\Delta L = 116.7$ m. The survival probability of anti-electron neutrino at this L/E can be approximated by two generation oscillation for Δm_{31}^2 with the fact that $\frac{\Delta m_{21}^2}{\Delta m_{31}} \ll 1$ is given by 3.27.

Fig. 3.6 is the constraint on these two parameters obtained by the CSHOOZ experiment [40]. Considering the result of the atmospheric neutrino experiments and the long baseline
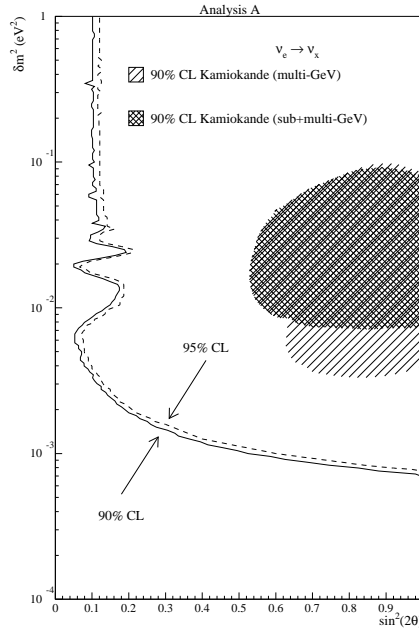
Figure 3.6: The excluded region for the oscillation parameters. This figure is taken from [40].

experiments, we have the upper bound at $\Delta m_{31}^2 \simeq 2 \times 10^{-3} \text{eV}^2$ as

$$\sin^2 2\theta_{13} \lesssim 0.2 \quad 90\% \text{CL}. \tag{3.32}$$

The future reactor experiments similar to CHOOZ, Double CHOOZ, Daya-Bay, and REton are expected to have a great sensitivity reach to $\sin^2 2\theta_{13}$ [42]

$$\sin^2 2\theta_{13} \simeq 0.01 - 0.03. \tag{3.33}$$

Finally, we mention that there is a indication of non-zero θ_{13} at 90% CL. from global analysis(atmospheric, long baseline, CHOOZ, solar, and KamLAND data)[41] with best-fit value of $\sin^2 2\theta_{13}$ is

$$\sin^2 2\theta_{13} = 0.016 \pm 0.010(1\sigma). \tag{3.34}$$

Chapter 4

Ongoing and Future Oscillation Experiments for 1-3 Sector

In this chapter, we briefly mention about the several ongoing and future long baseline experiments. The following experiments aim at measuring θ_{13}, and future experiments target also the CP-phase δ, and determination of the mass hierarchy of neutrinos by using the appearance oscillation channel. They will also improve the accuracy of Δm^2_{31} and θ_{23} determination by using the disappearance mode.

4.1   Ongoing experiments

T2K

T2K (Tokai to Kamioka)[43] is the experiment with conventional muon-neutrino beam from pion decay which are produced by bombarding graphite target by 30 GeV proton beam, from J-PARC, with intensity $\sim 10^2$ times higher than K2K at Tokai village. The far detector is the water Cherenkov detector SK and its baseline distance is 295 km. By setting the detector at $2.5°$ off-axis from beam direction, the neutrino beam have a narrow band energy spectrum peaked at $E \sim 600$ MeV (Fig. 4.1) which energy is nearly the oscillation maximum. In order to accomplish the precision determination of beam direction, T2K has a neutrino beam monitor named INGRID which is composed of iron/scintillator with mass of about 100 ton for near detector at on-axis. T2K has also the near detector at off-axis to measure the flux, energy spectrum, fraction of ν_e, and etc.

The main purpose of this experiment is measuring the $\nu_\mu(\bar{\nu}_\mu) \rightarrow \nu_e(\bar{\nu}_e)$ oscillation probability for determination of the value of θ_{13}.

NOνA

The NOνA (NuMI Off-Axis Neutrino Appearance)[45] experiment has a upgraded NuMI beam and 15 kton scintillator detector in off-axis at Ash River with the baseline distance $L = 810$ km. The peak energy of neutrino beam is taken to be about 2 GeV by using low energy option of NuMI beam and the off-axis detector. This experiment also measures
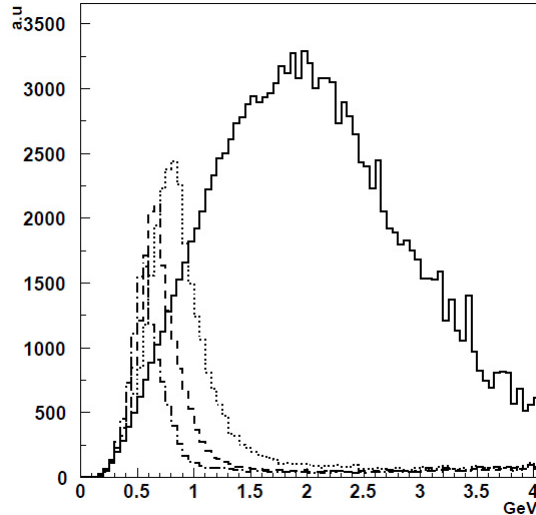
Figure 4.1: Energy spectrum of neutrino beam from J-PARC at various off-axis angles. The solid line shows the on-axis, the dotted, dashed, and dash-dotted lines show the $2.0°, 2.5°, 3.0°$ off-axis angle respectively. This figure is taken from [44].

the appearance oscillation channel $\nu_\mu \to \nu_e$. The sensitivity reach of θ_{13} is expected to be $\sin^2 2\theta_{13} \sim O(10^{-2})$.

OPERA

OPERA (Oscillation Project with Emulsion-tRacking Apparatus)[46] is a long baseline experiment to verify the appearance transition $\nu_\mu \to \nu_\tau$. The muon neutrino beam is produced by the CNGS (CERN Neutrino to Gran Sasso) at the CERN pointing towards the detector at Gran Sasso 730 km away. Averaged neutrino energy $\langle E_{\nu_\mu} \rangle$ is 17 GeV, much higher than the other experiments, which is required by a copious τ production. The detector has about 150,000 ECC(Emulsion Cloud Chamber) bricks with total target mass of 1.25 kton. Each ECC brick consists of 56 lead plates and 57 OPERA Films plates which have two emulsion layers of 44 μm. It has a powerful resolution capability of the event,

$$\nu_\tau + N \to \tau + X, \tag{4.1}$$

with sub-micron for position and mrad for angular resolutions.

It is expected to be observed about 10 events of tau lepton decay after 5 years running $(22.5 \times 10^{19}$ pot) with less than 1 background event for $\sin^2 2\theta_{13} = 0.1$.

4.2   Possible future experiments

T2KII and Hyper Kamiokande in Korea

There is a project of T2K phase II (T2KII) [47]. T2KII has upgraded J-PARC beam of 4 MW which is 5 times larger than T2K and the megaton water Cherenkov detector, Hyper

Kamiokande (HK).

Furthermore, there is a proposal of improvement of T2KII so-called T2KK[79] that have another half Mton water Cherenkov detector in Korea $L \simeq 1000$ km[1]. Using the identical detector helps reducing the systematic error and combining the information of two detectors have great advantage to resolve the parameter degeneracy. Therefore, T2KK have also the sensitivity to determine the mass hierarchy in small value of θ_{13} as $\sin^2 2\theta_{13} \sim O(10^{-2})$.

SPL super beam

There is a super beam project by using the CERN SPL (Super-conducting Proton Linac) which is a 2.2 GeV proton beam of 4 MW power [48]. The muon neutrino beam is produced by pion decay with an average neutrino energy $E_\nu = 0.27$ GeV. The water Cherenkov detector contains a 440 kton as a fiducial mass and to be located in Frejus with beseline distance $L = 130$ km from CERN.

The considerable background of the super beam experiment is 1-ring like 2γ event comes from π^0 decay which is produced by NC interaction. Therefore, when we measure the $\nu_\mu \to \nu_e$ oscillation, tight separation of electron/π^0 is needed. It can be done by using invariant mass of 2 gamma ($m_{\mathrm{inv}} \simeq m_\pi$ for π^0 event) and likelihood analysis for detailed distinction of 1-ring or 2-ring event.

Wide-band super beam

There is a U.S. scientific program of a long baseline experiment from Fermilab to DUSEL[49]. The neutrino beam is produced at BNL [50] or FNAL [51] towards a Mton class water Cherenkov or 100 kton class liquid Argon detector at Homestake with baseline distance $L = 2540(1290)$ km away from BNL (FNAL) to measure the $\nu_\mu(\bar{\nu}_\mu) \to \nu_e(\bar{\nu}_e)$ oscillation probability. If we set the detector at on-axis, neutrino beam have a broad energy spectrum ($E_\nu \lesssim 6$ GeV), similar to the J-PARC beam described in Fig. 4.1. The spectrum of wide-band beam contains not only the first oscillation but also the second oscillation dips in the disappearance channel. It is expected to be a powerful machinery for solving the parameter degeneracy. The experimental accuracy depends on how much we can reduce the π^0 backgrounds which is produced by high energy neutrino NC interaction rolling into the low energy bin.

Beta beam

Beta beam experiment [52] have the (anti-)electron neutrino beam produced by beta decay of accelerated radioisotope. The specific candidates are the beta decay of ${}^6_2\mathrm{He}$,

$$ {}^6_2\mathrm{He} \to {}^6_3\mathrm{Li} + e + \bar{\nu}_e, (4.2)$$

with the lifetime $\tau_{\frac{1}{2}} = 0.8067\mathrm{s}$ for antineutrinos, and the electron capture inverse beta decay of ${}^{18}_{10}\mathrm{Ne}$,

$$ {}^{18}_{10}\mathrm{Ne} \to {}^{18}_9\mathrm{Li} + e^+ + \nu_e, (4.3)$$

---

[1]Because the earth is round and neutrino beams are broadening, events can be observed at Kamioka and Korea simultaneously.

33

with the lifetime $\tau_{\frac{1}{2}} = 17$s for neutrinos. The ν_μ appearance is measured by the water Cherenkov detector for low gamma $\gamma \sim 100$. Because beta beam have clean ν_e beam and measure the muon event, backgrounds can be reduced and we can measure the appearance probability precisely. The work by [53] told that high gamma scenario ($\gamma \sim 2000$ and $L \sim 3000$ km with a 40 kton magnetized calorimeter) can determine the mass hierarchy even in $\sin^2 2\theta_{13} \sim O(10^{-3})$.

There is additional important point that if we combine the beta beam and the super beam experiments, we can have T- or CPT-conjugate measurement of $\nu_\mu \to \nu_e$ oscillation.

Neutrino factory

Neutrino factory[54] is a long future experiment which is expected not only to give the conclusive result on lepton flavor mixing parameters but also to discover some new physics because of its ultra-precise measurement of the golden channel oscillation, $\nu_e(\bar\nu_e) \to \nu_\mu(\bar\nu_\mu)$. Neutrino factory has high intense electron neutrino beam produced by the decay of high energy muons in muon storage ring. The advantage of this beam is that we can predict the flux and the spectrum very precisely. Note that muon decay also creates ν_μ beam, neutrino factory has the magnetized iron detector which can distinguish the correct CC ν_μ event from the wrong-sign muon which comes from non-oscillate $\bar\nu_\mu$ by charge identification. In addition, because the muon leaves long sharp track behind the detector at high energy ($E_\nu \gtrsim 10$ GeV) differ from electron, background can be dramatically reduced. Besides, neutrino factory can also measure the silver channel oscillation, $\nu_e \to \nu_\tau$, by using the OPERA like detector.

The optimized setting discussed by [87] has two detectors at $L = 4000$ and 7500 km and parent muon energy $E_\mu = 25$ GeV, it gives $E_\nu \sim O(10)$ GeV. The high intensity and precise measurement give the great sensitivity reach as $\sin^2 2\theta_{13} \sim O(10^{-4})$.

Chapter 5

Perturbation Formula of the Neutrino Oscillation Probability

In this chapter, we review the perturbation formula of the neutrino oscillation probability and its feature.

5.1 Exact formula of the oscillation probability

In this section, we show the exact formula of the oscillation probability of $\nu_e \to \nu_\mu$ as is known by Kimura-Takamura-Yokomakura[8].

If the electron number density is constant, the Hamiltonian in matter can be written by

$$H_{\mathrm{matt}} = \tilde{U} \frac{1}{2E} \begin{pmatrix} \lambda_1 & 0 & 0 \\ 0 & \lambda_2 & 0 \\ 0 & 0 & \lambda_3 \end{pmatrix} \tilde{U}^{-1}, \tag{5.1}$$

where $\tilde{U}$ is a effective mixing matrix and λ_i are the effective mass eigenvalues in matter.

The oscillation probability in matter can be expressed by putting these effective eigenvalues and mixing matrix into (2.31). Kimura-Takamura-Yokomakura[8] succeeded expressing a exact formula by using the standard oscillation parameters and matter effect.

$$P(\nu_e \to \nu_\mu) = D \cos \delta + B \sin \delta + C, \tag{5.2}$$

with

$$D = \sum_{(i,j)}^{\mathrm{cyclic}} D_{ij} \sin^2 \left(\frac{\Delta \lambda_{ij} L}{4E} \right), \tag{5.3}$$

$$B = \sum_{(i,j)}^{\mathrm{cyclic}} B' \sin \left(\frac{\Delta \lambda_{ij} L}{2E} \right), \tag{5.4}$$

$$C = \sum_{(i,j)}^{\mathrm{cyclic}} C_{ij} \sin^2 \left(\frac{\Delta \lambda_{ij} L}{4E} \right), \tag{5.5}$$

where $\Delta\lambda_{ij} \equiv \lambda_i - \lambda_j$ and cyclic (i,j) means sum over $(1,2),(2,3),(3,1)$,

$$
\begin{aligned}
D_{ij} &= -4\left[2p_1p_2\lambda_i\lambda_j + 2q_1q_2 + (p_1q_2 + q_1p_2)(\lambda_i + \lambda_j)\right] \\
&\quad \times (\Delta\lambda_{ij}\Delta\lambda_{12}\Delta\lambda_{23}\Delta\lambda_{31})^{-1} \tag{5.6}
\end{aligned}
$$

$$
B' = \frac{2(p_1q_2 - p_2q_1)}{\Delta\lambda_{12}\Delta\lambda_{23}\Delta\lambda_{31}} \tag{5.7}
$$

$$
\begin{aligned}
C_{ij} &= -4\left[(p_1^2 + p_2^2)\lambda_i\lambda_j + (q_1^2 + q_2^2) + (p_1q_1 + q_2p_2)(\lambda_i + \lambda_j)\right] \\
&\quad \times (\Delta\lambda_{ij}\Delta\lambda_{12}\Delta\lambda_{23}\Delta\lambda_{31})^{-1} \tag{5.8}
\end{aligned}
$$

$$
\begin{aligned}
p_1 &= (\Delta m_{31}^2 - \Delta m_{21}^2 s_{12}^2)s_{23}s_{13}c_{13} \tag{5.9} \\
p_2 &= \Delta m_{21}^2 s_{12}c_{12}c_{23}c_{13} \tag{5.10} \\
q_1 &= -\Delta m_{31}^2\Delta m_{21}^2 c_{12}^2 s_{23}s_{13}c_{13} \tag{5.11} \\
q_2 &= -\Delta m_{31}^2\Delta m_{21}^2 s_{12}c_{12}c_{23}c_{13} \tag{5.12}
\end{aligned}
$$

The derivation of this formula is done at Appendix A.1.

5.2 Perturbation theory of neutrino oscillation

We already have a exact formula of oscillation probability in matter, but it is too complicated to extract useful informations. Therefore we prepare the perturbative formulas of the oscillation probabilities known as the Cervera et al. formulas [62] using the small expansion parameters

$$
\epsilon \equiv \frac{\Delta m_{21}^2}{\Delta m_{31}^2} \simeq s_{13}, \tag{5.13}
$$

whose last order of magnitude equality is an assumption.

First, B in (5.4) can be transformed to

$$
B = -4B' \sin\left(\frac{\Delta\lambda_{12}L}{4E}\right) \sin\left(\frac{\Delta\lambda_{23}L}{4E}\right) \sin\left(\frac{\Delta\lambda_{31}L}{4E}\right), \tag{5.14}
$$

where we use the relation

$$
\sin 2x + \sin 2y + \sin 2z = -4\sin x \sin y \sin z \tag{5.15}
$$

which consist in $x + y + z = 0$.

Furthermore, using the relation

$$
\sin^2 x = -\sin x \sin y \cos z - \sin x \cos y \sin z, \tag{5.16}
$$

in the same condition, D can be transformed to

$$
D = -\sum_{(i,j,k)}^{\text{cyclic}} (D_{jk} + D_{ki}) \cos\left(\frac{\Delta\lambda_{ij}L}{4E}\right) \sin\left(\frac{\Delta\lambda_{jk}L}{4E}\right) \sin\left(\frac{\Delta\lambda_{ki}L}{4E}\right). \tag{5.17}
$$

They help us transforming the formula to the one easier to find the dependence of Δm_{21}^2 as

$$D = \sum_{(i,j,k)}^{\text{cyclic}} \frac{-8J_r \Delta m_{21}^2 \left[\Delta m_{31}^2 \lambda_k (\lambda_k - \Delta m_{31}^2) - D_k^{(1)}\right]}{(\Delta \lambda_{jk})^2 (\Delta \lambda_{ki})^2}$$

$$\times \cos\left(\frac{\Delta \lambda_{ij} L}{4E}\right) \sin\left(\frac{\Delta \lambda_{jk} L}{4E}\right) \sin\left(\frac{\Delta \lambda_{ki} L}{4E}\right) \tag{5.18}$$

$$B = \frac{8J_r \Delta m_{21}^2 \Delta m_{31}^2 (\Delta m_{31}^2 - \Delta m_{21}^2)}{\Delta \lambda_{12} \Delta \lambda_{23} \Delta \lambda_{31}} \sin\left(\frac{\Delta \lambda_{12} L}{4E}\right) \sin\left(\frac{\Delta \lambda_{23} L}{4E}\right) \sin\left(\frac{\Delta \lambda_{31} L}{4E}\right) \tag{5.19}$$

$$C = \sum_{(i,j)}^{\text{cyclic}} \frac{-4\left[s_{13}^2 \left\{s_{23}^2 c_{13}^2 (\Delta m_{31}^2)^2 \lambda_i \lambda_j + C_{ij}^{(1)} + C_{ij}^{(2a)}\right\} + C_{ij}^{(2b)}\right]}{\Delta \lambda_{ij} \Delta \lambda_{12} \Delta \lambda_{23} \Delta \lambda_{31}} \sin^2\left(\frac{\Delta \lambda_{ij} L}{4E}\right) \tag{5.20}$$

where $J_r = s_{12} c_{12} s_{23} c_{23} s_{13} c_{13}^2$. The superscript (n) means order of Δm_{21}^2 (and hence of ϵ) as

$$D_k^{(1)} = \Delta m_{21}^2 \left[\Delta m_{31}^2 \lambda_k (c_{12}^2 - s_{12}^2) + \lambda_k^2 s_{12}^2 - (\Delta m_{31}^2)^2 c_{12}^2\right] \tag{5.21}$$

$$C_{ij}^{(1)} = \Delta m_{21}^2 \Delta m_{31}^2 \left[-\lambda_i (\lambda_j s_{12}^2 + \Delta m_{31}^2 c_{12}^2) - \lambda_j (\lambda_i s_{12}^2 + \Delta m_{31}^2 c_{12}^2)\right] s_{23}^2 c_{13}^2 \tag{5.22}$$

$$C_{ij}^{(2a)} = (\Delta m_{21}^2)^2 (\lambda_i s_{12}^2 + \Delta m_{31}^2 c_{12}^2)(\lambda_j s_{12}^2 + \Delta m_{31}^2 c_{12}^2) s_{23}^2 c_{13}^2 \tag{5.23}$$

$$C_{ij}^{(2b)} = (\Delta m_{21}^2)^2 (\lambda_i - \Delta m_{31}^2)(\lambda_j - \Delta m_{31}^2) s_{12}^2 c_{12}^2 c_{23}^2 c_{13}^2. \tag{5.24}$$

In order to obtain the oscillation probability to order ϵ^2 (5.13), we need the effective eigenvalues λ_i only in zeroth order in ϵ as

$$\begin{aligned} \lambda_1 &= O(\epsilon) \\ \lambda_2 &= 2Ea + O(\epsilon) \\ \lambda_3 &= \Delta m_{31}^2 + O(\epsilon). \end{aligned} \tag{5.25}$$

Then, we have the approximate formula in up to ϵ^2 order

$$D = 8J_r \cos\left(\frac{\Delta m_{31}^2 L}{4E}\right) \frac{\Delta}{a - \Delta} \sin\left(\frac{a - \Delta}{2} L\right) \frac{\Delta m_{21}^2}{2Ea} \sin\frac{aL}{2} \tag{5.26}$$

$$B = -8J_r \sin\left(\frac{\Delta m_{31}^2 L}{4E}\right) \frac{\Delta}{a - \Delta} \sin\left(\frac{a - \Delta}{2} L\right) \frac{\Delta m_{21}^2}{2Ea} \sin\frac{aL}{2} \tag{5.27}$$

$$C = 4s_{13}^2 c_{13}^2 s_{23}^2 \left(\frac{\Delta}{a - \Delta} \sin\left(\frac{a - \Delta}{2} L\right)\right)^2 + 4s_{12}^2 c_{12}^2 c_{23}^2 c_{13}^2 \left(\frac{\Delta m_{21}^2}{2Ea} \sin\frac{aL}{2}\right)^2, \tag{5.28}$$

where $\Delta \equiv \frac{\Delta m_{31}^2}{2E}$.

Therefore, we obtain the Cervera et al. formula for the oscillation probabilitiy of $\nu_\mu \to \nu_e$ up to second order in ϵ

$$P \equiv P(\nu_\mu \to \nu_e) = X_\pm^2 s^2 \pm 2X_\pm Z s \cos(\delta \pm \Delta_{31}) + Z^2 \tag{5.29}$$

where $s \equiv \sin 2\theta_{13}$, $\Delta_{ij} \equiv \frac{|\Delta m_{ij}^2|L}{4E}$, $A \equiv \frac{aL}{2}$, and the functions $X_\pm$, and Z are defined by

$$
\begin{aligned}
X_\pm &= s_{23}\frac{\Delta_{31}\sin(\Delta_{31} \mp A)}{(\Delta_{31} \mp A)}, \\
Z &= c_{23}\sin 2\theta_{12}\frac{\Delta_{21}\sin A}{A},
\end{aligned}
\tag{5.30}
$$

with $\pm$ for the mass hierarchy, namely, the normal or the inverted hierarchies for the positive and the negative sign of Δm_{31}^2, respectively.

It is notable that (5.29) can be written in a form of amplitude squared,

$$
P = \left| X_\pm s \pm \mathrm{e}^{i(\delta \pm \Delta_{31})}Z \right|^2,
\tag{5.31}
$$

which allows simple interpretation of the δ dependence term as an interference between the atmospheric $(s^2 X_\pm)$ and the solar (Z) oscillations.

Similarly, its CP-conjugate channel $\bar{\nu}_\mu \to \bar{\nu}_e$, the T-conjugate channel $\nu_e \to \nu_\mu$, and the CPT-conjugate channel $\bar{\nu}_e \to \bar{\nu}_\mu$, in matter are given as

$$
\begin{aligned}
P^{CP} &\equiv CP[P(\nu_\mu \to \nu_e)] = P(\bar{\nu}_\mu \to \bar{\nu}_e) &= X_\mp^2 s^2 \pm 2X_\mp Zs\cos\left(\delta \mp \Delta_{31}\right) + Z^2 &(5.32) \\
P^{T} &\equiv T[P(\nu_\mu \to \nu_e)] = P(\nu_e \to \nu_\mu) &= X_\pm^2 s^2 \pm 2X_\pm Zs\cos\left(\delta \mp \Delta_{31}\right) + Z^2 &(5.33) \\
P^{CPT} &\equiv CPT[P(\nu_\mu \to \nu_e)] = P(\bar{\nu}_e \to \bar{\nu}_\mu) &= X_\mp^2 s^2 \pm 2X_\mp Zs\cos\left(\delta \pm \Delta_{31}\right) + Z^2 &(5.34)
\end{aligned}
$$

In this thesis, our emphasis is placed on the oscillation channels between ν_μ and ν_e and their anti-particles. To have a clearer view of the structure of parameter degeneracy, however, we will include the $\nu_e \to \nu_\tau$ appearance channel, which is sometimes called the "silver channel". See Sec. 7.2. The oscillation probability $P(\nu_e \to \nu_\tau)$ is given by

$$
P^S \equiv P(\nu_e \to \nu_\tau) = \cot^2\theta_{23}X_\pm^2 s^2 \mp 2X_\pm Zs\cos\left(\delta \mp \Delta_{31}\right) + \tan^2\theta_{23}Z^2.
\tag{5.35}
$$

Chapter 6

Analytic Solution and Overview of Parameter Degeneracy in CP-conjugate Measurement

In this chapter, we discuss the parameter degeneracy problem in CP-conjugate measurement which may arise in future long baseline experiments.

As we saw before many of the neutrino oscillation parameters are successfully determined. But there still remain the unknown parameters, θ_{13} and δ, in the MNS matrix, and we have to determine the neutrino mass hierarchy in order to complete our understanding of the lepton flavor mixing structure. It was proposed that if θ_{13} is relatively large an intense neutrino beam from nuclear reactors can be used to measure it as discussed in Section 3.3. Alternatively, the accelerator search for nonzero θ_{13} has advantage of potential possibility of extending it to the CP-phase δ search.

It is known that detection of CP violation effect due to the lepton Kobayashi-Maskawa phase δ which is nothing but three flavor effect is suppressed by the two small factors, the ratio $\Delta m_{21}^2 / \Delta m_{31}^2 \simeq 0.03$ and the value of θ_{13} which is known to be small by CHOOZ experiment as discussed in Chapter 3. Therefore, high precision experiments are required to measure the CP violating phase δ. Once precision measurement is required, the experiment is better characterized as a simultaneous determination of θ_{13} and δ.

However, there is a problem of parameter degeneracy [55, 56, 57] that a set of measurement of the oscillation probabilities, $P(\nu_\mu \to \nu_e)$ and its CP conjugate $P(\bar{\nu}_\mu \to \bar{\nu}_e)$ at a particular neutrino energy, can not determine uniquely the values of θ_{13} and δ. The degeneracy can be understood as the so called intrinsic degeneracy [55], sign-Δm_{31}^2 degeneracy [56] duplicated by the unknown sign of Δm_{31}^2, and octant degeneracy [57], which gives the eightfold degeneracy if $\theta_{23} \neq \pi/4$. The Fig. 6.1 shows the feature that the set of different value of θ_{13} and δ can reproduce the same value of $P(\nu_e \to \nu_\mu)$ and $P(\bar{\nu}_e \to \bar{\nu}_\mu)$. A notorious feature of the degeneracy is that it may confuse CP violation with CP conservation or normal mass hierarchy with inverted mass hierarchy.

In this chapter, with use of the approximate form of the oscillation probability obtained in [62] we review the exact analytic expressions of all the degeneracy solutions which are given by [59, 60], and show the explicit form of the mapping.

Before going into the specific discussion, we mention that in mathematical point of view,
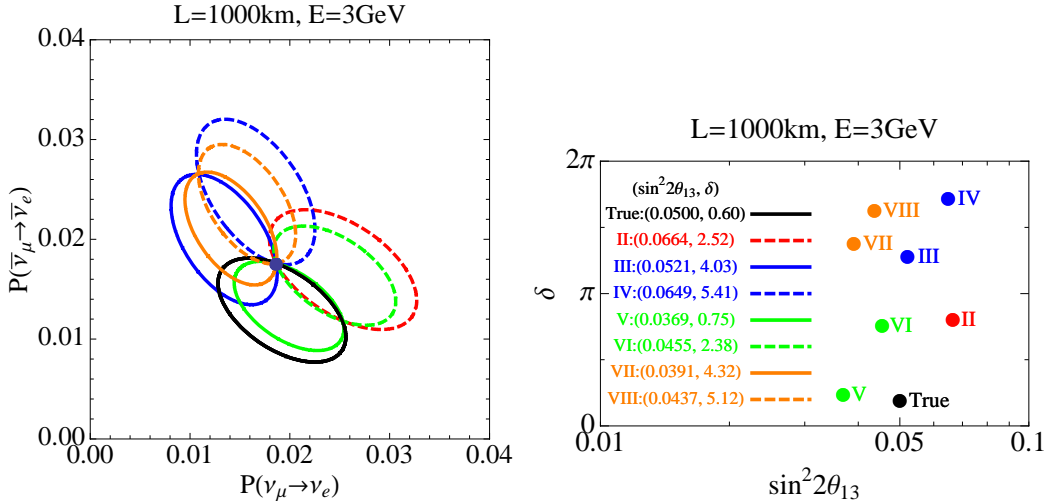
Figure 6.1: Left : An illustrative example of the eightfold degeneracy is represented pictorially in terms of the $P - P^{CP}$ bi-probability plot [56]. The way of illustration first appeared in [58]. The true solution with assumed parameters ($\sin^2 2\theta_{13}$, mass hierarchy type, θ_{23} in degrees) = (0.05, NH, 40) is denoted by a black ellipse, where the hierarchy is denoted as either NH or IH corresponding to the normal and the inverted ones. Right : It shows where the solutions appear at in $\sin^2 2\theta_{13} - \delta/\pi$ plane.

the degeneracy is easy to solve. Bringing in measurement at another energy or baseline, or adding a different oscillation channel can solve the degeneracy. Alternatively, if the spectrum information is available it may resolve the degeneracy. But unfortunately, it is known that some types of the degeneracy that are robust in varying experimental settings. One of the reasons is that, as we will see in Section6.3, the energy dependence of the degenerate solutions is so mild that spectrum information does not help resolving them.

Rather, we focus on a complete understanding of structure of the degeneracy. It will be called for if future neutrino experiments reveal features that may not fit in into the standard three-neutrino mixing. For example, if they can detect the nonstandard neutrino interactions [5, 65, 66, 67, 68], the event structure will be modified by the new ingredients and enriched with new type of the degeneracies [70, 71].

First, we give a complete treatment of the parameter degeneracy with CP-conjugate measurement in vacuum and in matter. Then, using the results, we give an overview the structure of parameter degeneracy.

6.1 Parameter degeneracy in CP-conjugate measurement

In what follows we denote the input true solution with subscript "1" as s_1, the unique case with Arabic numerals, and the degenerate solutions with Roman subscripts "II", "III", etc. We denote the mass hierarchy of the true solution by the $\pm$ signs (+ for the normal and $-$

for the inverted) to make the hierarchy choice always explicit. The relationship between the degeneracy solutions with input true mass hierarchies will be further discussed in Sec. 6.2.

Now, let us start our discussion of parameter degeneracy by taking CP-conjugate measurement. The setting seems to be the most promising one experimentally in the near future.

In this section, we analyze first the case in vacuum which is good practice to get used to parameter degeneracy problem.

6.1.1 The intrinsic and sign-Δm_{31}^2 degenerate solutions in vacuum

We start from the intrinsic degeneracy in vacuum. Next, we discuss the sign-Δm_{31}^2 degeneracy. Because the θ_{23} octant degeneracy solutions do not have simple form even in vacuum, we skip it. In this and the following two subsections the degenerate solutions have the same values of θ_{23} which can be non-maximal.

The intrinsic degeneracy in vacuum

The intrinsic degeneracy solutions (s_i, δ_i) (i=1, 2) are defined by

$$
\begin{aligned}
P &= X_{\text{vac}}^2 s_1^2 \pm 2 X_{\text{vac}} Z_{\text{vac}} s_1 \left(\cos \delta_1 \cos \Delta_{31} \mp \sin \delta_1 \sin \Delta_{31} \right) + Z_{\text{vac}}^2 \\
&= X_{\text{vac}}^2 s_2^2 \pm 2 X_{\text{vac}} Z_{\text{vac}} s_2 \left(\cos \delta_2 \cos \Delta_{31} \mp \sin \delta_2 \sin \Delta_{31} \right) + Z_{\text{vac}}^2 \quad (6.1)
\end{aligned}
$$

and in CP- or T- conjugate channel by

$$
\begin{aligned}
P^{CP} &= X_{\text{vac}}^2 s_1^2 \pm 2 X_{\text{vac}} Z_{\text{vac}} s_1 \left(\cos \delta_1 \cos \Delta_{31} \pm \sin \delta_1 \sin \Delta_{31} \right) + Z_{\text{vac}}^2 \\
&= X_{\text{vac}}^2 s_2^2 \pm 2 X_{\text{vac}} Z_{\text{vac}} s_2 \left(\cos \delta_2 \cos \Delta_{31} \pm \sin \delta_2 \sin \Delta_{31} \right) + Z_{\text{vac}}^2 \quad (6.2)
\end{aligned}
$$

where the functions X_{vac} and Z_{vac} are defined by

$$
\begin{aligned}
X_{\text{vac}} &\equiv \lim_{a \to 0} X_+ = \lim_{a \to 0} X_- = s_{23} \sin \Delta_{31}, \\
Z_{\text{vac}} &\equiv \lim_{a \to 0} Z = c_{23} \sin 2\theta_{12} \Delta_{21}. \quad (6.3)
\end{aligned}
$$

By adding or subtracting (6.1) and (6.2), we obtain for $\sin \delta_2$ and $\cos \delta_2$

$$
\begin{aligned}
s_2 \cos \delta_2 &= s_1 \cos \delta_1 \pm \frac{X_{\text{vac}}^2 (s_1^2 - s_2^2)}{2 X_{\text{vac}} Z \cos \Delta_{31}}, \\
s_2 \sin \delta_2 &= s_1 \sin \delta_1. \quad (6.4)
\end{aligned}
$$

Inserting (6.4) into $\sin^2 \delta_2 + \cos^2 \delta_2 = 1$, we obtain the quartic equation of s_2 as $(s_2^2 - s_1^2)(s_2^2 - s_{\text{II}}) = 0$. Note that $s_2 = s_1$ is a trivial solution of the equations (6.1) and (6.2), the intrinsic degeneracy solution s_{II} is given by

$$
s_{\text{II}}^2 = s_1^2 \pm 4 \left(\frac{Z_{\text{vac}} \cos \Delta_{31}}{X_{\text{vac}}} \right) s_1 \cos \delta_1 + 4 \left(\frac{Z_{\text{vac}} \cos \Delta_{31}}{X_{\text{vac}}} \right)^2. \quad (6.5)
$$

Inserting the solution (6.5) into (6.4), we obtain the simple form of δ_{II} as

$$
\begin{aligned}
s_{\text{II}} \cos \delta_{\text{II}} &= - \left(s_1 \cos \delta_1 \pm \frac{2 Z_{\text{vac}}}{X_{\text{vac}}} \cos \Delta_{31} \right), \\
s_{\text{II}} \sin \delta_{\text{II}} &= s_1 \sin \delta_1. \quad (6.6)
\end{aligned}
$$

The sign-Δm_{31}^2 degeneracy in vacuum

The defining equations of the sign-Δm_{31}^2 degeneracies in vacuum in both the neutrino and the antineutrino channels are as follows:

$$
\begin{aligned}
P &= X_{\text{vac}}^2 s_1^2 \pm 2 X_{\text{vac}} Z_{\text{vac}} s_1 \left(\cos \delta_1 \cos \Delta_{31} \mp \sin \delta_1 \sin \Delta_{31} \right) + Z_{\text{vac}}^2 \\
&= X_{\text{vac}}^2 s_3^2 \mp 2 X_{\text{vac}} Z_{\text{vac}} s_3 \left(\cos \delta_3 \cos \Delta_{31} \pm \sin \delta_3 \sin \Delta_{31} \right) + Z_{\text{vac}}^2
\end{aligned}
\tag{6.7}
$$

$$
\begin{aligned}
P^{CP} &= X_{\text{vac}}^2 s_1^2 \pm 2 X_{\text{vac}} Z_{\text{vac}} s_1 \left(\cos \delta_1 \cos \Delta_{31} \pm \sin \delta_1 \sin \Delta_{31} \right) + Z_{\text{vac}}^2 \\
&= X_{\text{vac}}^2 s_3^2 \mp 2 X_{\text{vac}} Z_{\text{vac}} s_3 \left(\cos \delta_3 \cos \Delta_{31} \mp \sin \delta_3 \sin \Delta_{31} \right) + Z_{\text{vac}}^2.
\end{aligned}
\tag{6.8}
$$

Proceeding the same way as in the intrinsic case, we obtain the same equation as (6.4) apart from the sign in front of $\cos \delta_3$;

$$
\begin{aligned}
s_3 \cos \delta_3 &= - \left(s_1 \cos \delta_1 \pm \frac{X_{\text{vac}}^2 (s_1^2 - s_2^2)}{2 X_{\text{vac}} Z \cos \Delta_{31}} \right), \\
s_3 \sin \delta_3 &= s_1 \sin \delta_1.
\end{aligned}
\tag{6.9}
$$

Then, it is obvious that we obtain exactly the same equation as in the intrinsic degeneracy case, which of course entails in the same solution (6.5). We denote the two solutions $(s_{\text{III}}, \delta_{\text{III}})$ and $(s_{\text{IV}}, \delta_{\text{IV}})$. We can arbitrarily choose them so that $s_{\text{III}} = s_1$ and $s_{\text{IV}} = s_{\text{II}}$.

For the solution $s_{\text{III}} = s_1$ (6.9) leads to

$$
\begin{aligned}
\sin \delta_{\text{III}} &= \sin \delta_1, \\
\cos \delta_{\text{III}} &= -\cos \delta_1,
\end{aligned}
\tag{6.10}
$$

with the obvious solution $\delta_{\text{III}}^{\text{vac}} = \pi - \delta_1$. For $s_3 = s_{\text{IV}} = s_{\text{II}}$ (6.9) takes the form

$$
\begin{aligned}
\sin \delta_{\text{IV}} &= \frac{s_1}{s_{\text{IV}}} \sin \delta_1 \\
\cos \delta_{\text{IV}} &= \frac{1}{s_{\text{IV}}} \left(s_1 \cos \delta_1 \pm \frac{2 Z_{\text{vac}}}{X_{\text{vac}}} \cos \Delta_{31} \right)
\end{aligned}
\tag{6.11}
$$

Since $s_{\text{IV}} = s_{\text{II}}$, it follows that $\cos \delta_{\text{IV}} = -\cos \delta_{\text{II}}$ and $\sin \delta_{\text{IV}} = \sin \delta_{\text{II}}$, which means that $\delta_{\text{IV}} = \pi - \delta_{\text{II}}$. Though it might look trivial these discussions are useful for unambiguous definitions of the degenerate solutions.

6.1.2 The intrinsic degeneracy in matter

After the example of the case in vacuum, let us consider the degenerate solutions in matter as illustrated in Fig. 6.2.

With expression of the oscillation probabilities in (5.29) and (5.32), the intrinsic degeneracy solutions (s_i, δ_i) (i=1, 2) in CP-conjugate measurement in matter are defined by

$$
\begin{aligned}
P &= X_{\pm}^2 s_1^2 \pm 2 X_{\pm} Z s_1 \left(\cos \delta_1 \cos \Delta_{31} \mp \sin \delta_1 \sin \Delta_{31} \right) + Z^2 \\
&= X_{\pm}^2 s_2^2 \pm 2 X_{\pm} Z s_2 \left(\cos \delta_2 \cos \Delta_{31} \mp \sin \delta_2 \sin \Delta_{31} \right) + Z^2
\end{aligned}
\tag{6.12}
$$
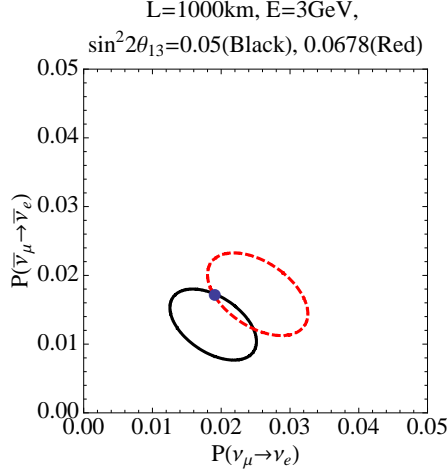
Figure 6.2: Bi-probability plot for intrinsic degeneracy. Black ellipse : $\sin^2 2\theta_{13}^1 = 0.05$. Red dashed line : $\sin^2 2\theta_{13} = 0.0678$. Both ellipses are the case of normal hierarchy.

and in CP-conjugated channel by

$$
\begin{aligned}
P^{CP} &= X_\mp^2 s_1^2 \pm 2X_\mp Z s_1 \left(\cos\delta_1 \cos\Delta_{31} \pm \sin\delta_1 \sin\Delta_{31}\right) + Z^2 \\
&= X_\mp^2 s_2^2 \pm 2X_\mp Z s_2 \left(\cos\delta_2 \cos\Delta_{31} \pm \sin\delta_2 \sin\Delta_{31}\right) + Z^2
\end{aligned}
\tag{6.13}
$$

We remind the readers again that the $\pm$ signs in the subscripts correspond to the true mass hierarchies, $+$ for the normal and $-$ for inverted ones. Assuming $X_\pm \neq 0$, adding or subtracting (6.12) divided by $X_\pm$ and (6.13) divided by $X_\mp$, we obtain

$$
\begin{aligned}
s_2 \cos\delta_2 &= s_1 \cos\delta_1 \pm \frac{(s_1^2 - s_2^2)(X_\pm + X_\mp)}{4Z \cos\Delta_{31}}, \\
s_2 \sin\delta_2 &= s_1 \sin\delta_1 \pm \frac{(s_1^2 - s_2^2)(X_\mp + X_\pm)}{4Z \cos\Delta_{31}}.
\end{aligned}
\tag{6.14}
$$

Inserting (6.14) into $\cos^2\delta_2 + \sin^2\delta_2 = 1$ gives a quartic equation for s_2 as $(s_2^2 - s_1^2)(s_2^2 - s_{\mathrm{II}}^2) = 0$ like the case in vacuum. Of course, we again obtain the trivial solution $s_2 = s_1$, the situation unique to discussions of the intrinsic degeneracy. The genuine intrinsic degeneracy solution is given by

$$
s_{\mathrm{II}}^2 = s_1^2 + \frac{4Z^2 \sin^2 2\Delta_{31} + 4s_1 Z \sin 2\Delta_{31}\{X_\pm \sin(\delta_1 \mp \Delta_{31}) - X_\mp \sin(\delta_1 \pm \Delta_{31})\}}{X_\pm^2 + X_\mp^2 - 2X_\pm X_\mp \cos 2\Delta_{31}}
\tag{6.15}
$$

By using (6.15) into (6.14) we obtain the solution of δ_{II}.

6.1.3 The sign-Δm^2 degeneracy in matter

We turn to the flipped Δm^2-sign degeneracy in CP-conjugate measurement as illustrated in Fig. 6.3. The true input solution (s_1, δ_1) and the opposite Δm_{31}-sign clone solution

43

L=1000km, E=3GeV,
$\sin^2 2\theta_{13}$=0.05(Black) with NH,
$\sin^2 2\theta_{13}$=0.0523(Blue), 0.0639(Green) with IH
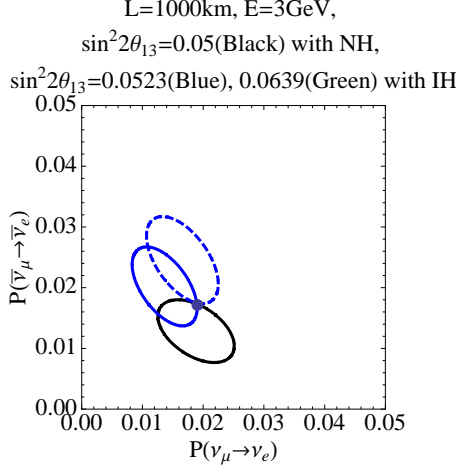
Figure 6.3: Bi-probability plot for sign-Δm_{31}^2 degeneracy. Black ellipse : $\sin^2 2\theta_{13}^1 = 0.05$ with normal hierarchy(NH), and blue solid (dashed) ellipse : $\sin^2 2\theta_{13} = 0.0523(0.0639)$ with inverted hierarchy(IH).

(s_3, δ_3) satisfy the following equations. In the neutrino channel,

$$
\begin{aligned}
P &= X_\pm^2 s_1^2 \pm 2X_\pm Z s_1 \left(\cos\delta_1 \cos\Delta_{31} \mp \sin\delta_1 \sin\Delta_{31}\right) + Z^2, \\
&= X_\mp^2 s_3^2 \mp 2X_\mp Z s_3 \left(\cos\delta_3 \cos\Delta_{31} \pm \sin\delta_3 \sin\Delta_{31}\right) + Z^2,
\end{aligned}
\tag{6.16}
$$

and in CP-conjugated channel

$$
\begin{aligned}
P^{CP} &= X_\mp^2 s_1^2 \pm 2X_\mp Z s_1 \left(\cos\delta_1 \cos\Delta_{31} \pm \sin\delta_1 \sin\Delta_{31}\right) + Z^2, \\
&= X_\pm^2 s_3^2 \mp 2X_\pm Z s_3 \left(\cos\delta_3 \cos\Delta_{31} \mp \sin\delta_3 \sin\Delta_{31}\right) + Z^2.
\end{aligned}
\tag{6.17}
$$

By combining the first and the second equations in (6.16) and (6.17) assuming $X_\pm \neq 0$ as similar to previous subsection, we obtain

$$
\begin{aligned}
&s_3 \cos\delta_3 \\
&= \frac{-s_1^2 X_\pm^2 + s_3^2 X_\mp^2 \mp 2s_1 Z X_\pm \cos(\delta_1 \pm \Delta_{31})}{\pm 4ZX_\mp \cos\Delta_{31}} - \frac{s_1^2 X_\mp^2 - s_3^2 X_\pm^2 \pm 2s_1 Z X_\mp \cos(\delta_1 \mp \Delta_{31})}{\pm 4ZX_\pm \cos\Delta_{31}} \\
&s_3 \sin\delta_3 \\
&= \frac{-s_1^2 X_\pm^2 + s_3^2 X_\mp^2 \mp 2s_1 Z X_\pm \cos(\delta_1 \pm \Delta_{31})}{4ZX_\mp \sin\Delta_{31}} + \frac{s_1^2 X_\mp^2 - s_3^2 X_\pm^2 \pm 2s_1 Z X_\mp \cos(\delta_1 \mp \Delta_{31})}{4ZX_\pm \sin\Delta_{31}}
\end{aligned}
\tag{6.18}
$$

We insert (6.18) into $\cos^2\delta_3 + \sin^2\delta_3 = 1$ we obtain the quartic equation for s_3 as

$$
T_{\text{sign}} s_3^4 - U_{\text{sign}\pm} s_3^2 + V_{\text{sign}\pm} = 0,
\tag{6.19}
$$

where

$$
T_{\text{sign}} \equiv \frac{X_+^2 + X_-^2 - 2X_+ X_- \cos 2\Delta_{31}}{(2Z \sin 2\Delta_{31})^2}
\tag{6.20}
$$

44

$$U_{\text{sign}} \equiv 1 - s_1 \frac{(X_{\mp} - X_{\pm})\{s_1(X_{\mp}^3 - X_{\pm}^3) \pm 2X_{\mp}^2 Z \cos(\delta_1 \mp \Delta_{31}) \mp 2X_{\pm}^2 Z \cos(\delta_1 \pm \Delta_{31})\}}{8X_{\pm}X_{\mp}Z^2 \sin^2 \Delta_{31}}$$
$$- s_1 \frac{(X_{\mp} + X_{\pm})\{s_1(X_{\mp}^3 + X_{\pm}^3) \pm 2X_{\mp}^2 Z \cos(\delta_1 \mp \Delta_{31}) \pm 2X_{\pm}^2 Z \cos(\delta_1 \pm \Delta_{31})\}}{8X_{\pm}X_{\mp}Z^2 \cos^2 \Delta_{31}}$$

$$(6.21)$$

$$V_{\text{sign}\pm} \equiv s_1^2 \frac{\pm s_1(X_{\mp}^3 - X_{\pm}^3) + 2X_{\mp}^2 Z \cos(\delta_1 \mp \Delta_{31}) - 2X_{\pm} Z \cos(\delta_1 \pm \Delta_{31})}{(4X_{\pm}X_{\mp}Z \sin \Delta_{31})^2}$$
$$+ s_1^2 \frac{\pm s_1(X_{\mp}^3 + X_{\pm}^3) + 2X_{\mp}^2 Z \cos(\delta_1 \mp \Delta_{31}) + 2X_{\pm} Z \cos(\delta_1 \pm \Delta_{31})}{(4X_{\pm}X_{\mp}Z \cos \Delta_{31})^2} \quad (6.22)$$

Equation (6.19) has the obvious solutions

$$s_3^2 = \frac{1}{2T_{\text{sign}}} \left[U_{\text{sign}\pm} \, [\pm]^* \, \sqrt{U_{\text{sign}\pm}^2 - 4T_{\text{sign}}V_{\text{sign}\pm}} \right] \quad (6.23)$$

where $[\pm]^*$ denotes a temporary sign which is independent of the hierarchy sign. We discuss immediately below (Sec. 6.1.3) the way how to determine the sign convention. If the content of square root of (6.23) is positive, there are four real solutions of s_3 and the two positive ones are physical; The sign-Δm_{31}^2 degeneracy is two-fold.

On the other hand, if it is negative there is no degenerate solution. Therefore the region specified by $D_{\pm}^{\text{sign}} \equiv U_{\text{sign}\pm}^2 - 4T_{\text{sign}}V_{\text{sign}\pm} \leq 0$ defines the region in which there is no sign-Δm_{31}^2 degeneracy solution. The region of no sign-degeneracy solution is displayed in Fig. 6.4 by taking four typical values of baseline distances and neutrino energies. In this figure the true mass hierarchy is taken to be the normal one. If we take the input inverted hierarchy we must have the figure with δ shifted by π. The reason of its feature will be discussed in Sec. 6.2.2
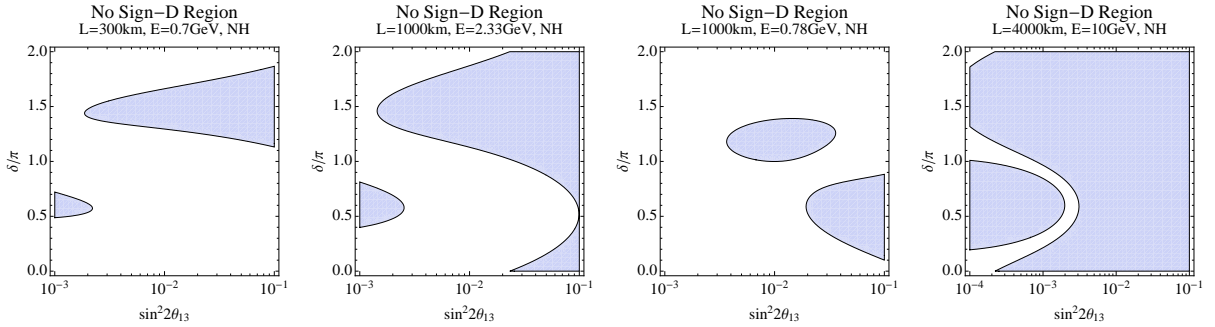
Figure 6.4: Depicted as the shaded areas in the $\sin^2 2\theta_{13} - \delta/\pi$ space are the regions where no sign-Δm_{31}^2 degeneracy solution exists for four set of the baselines and the neutrino energies. The true mass hierarchy is taken to be the inverted one.

The notable feature that the region of absent solution occupies mostly around $\delta \sim 3\pi/2$ can be understood by bi-probability plot (Fig. 6.5). The green line show the line of $\delta = \frac{3\pi}{2}$ with normal hierarchy it is the farthest region from the region inverted hierarchy fill
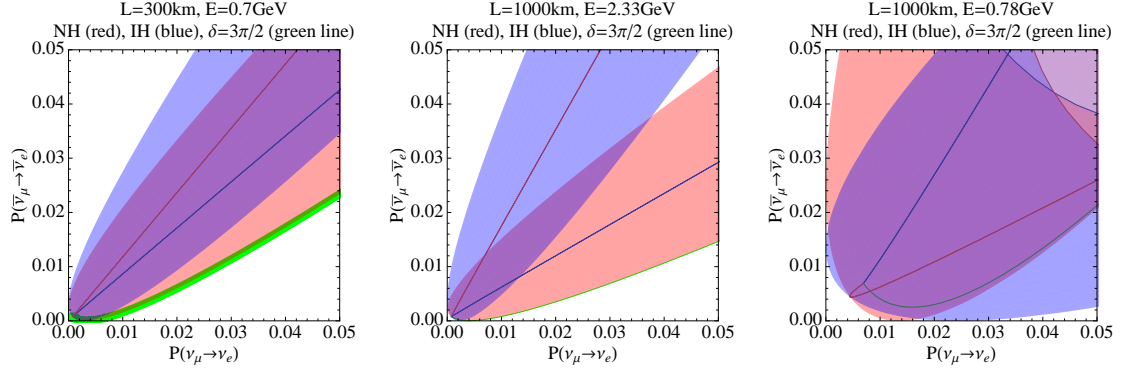
Figure 6.5: Shown by the red and the blue shaded areas in the $P - P^{CP}$ bi-probability space are the regions spanned by the ellipses with normal and inverted hierarchy, respectively. The green line of the left panel shows the region varying θ_{13} with $\delta = \frac{3\pi}{2}$ and normal hierarchy.

in. It is the region of lucky resolution of the sign-Δm_{31}^2 degeneracy [76] for the normal ($\delta \sim \pi/2$ for the inverted) mass hierarchy. Generally speaking the no sign-degeneracy region grows for longer baseline, and the tendency continues to e.g., $L = 4000$ km and $E = 10$ GeV, the fourth panel of Fig. 6.4. Comparing the left and middle panels of Fig. 6.5, it can be understood that longer baseline separates the normal hierarchy region from the inverted hierarchy region. However, the feature changes for region near the second oscillation maximum as seen in the third panel in Fig. 6.4. There are much better chance of having the sign-Δm_{31}^2 degeneracy.

Problem of convention of labeling the sign-Δm_{31}^2 degenerate solution

We denote the two solutions in (6.23) as s_{III} and s_{IV}. It is a highly nontrivial issue how to define these two solutions. In principle there are two ways:

Convention A: One can take the convention such that always $s_{\mathrm{IV}} \geq s_{\mathrm{III}}$. That is, the plus and the minus signs in (6.23) correspond to s_{IV} and s_{III}, respectively.

Convention B: One may choose the other convention such that the vacuum limit of the degenerate solutions can be taken smoothly.

For reasons explained below we adopt the convention B. We note that $D_{\pm}^{\mathrm{sign}}$ defined as $D_{\pm}^{\mathrm{sign}} \equiv U_{\mathrm{sign}\pm}^2 - 4T_{\mathrm{sign}}V_{\mathrm{sign}\pm}$ which can be simplified in the vacuum oscillation limit, $a \to 0$, as

$$D_{\pm}^{\mathrm{oct\text{-}vac}} \equiv \lim_{a \to 0} D_{\pm}^{\mathrm{sign}} = (d_{\pm}^{\mathrm{sign}})^2 \tag{6.24}$$

where

$$d_{\pm}^{\mathrm{sign}} = 1 \pm \frac{s_1 X_{\mathrm{vac}} \cos \delta_1}{Z_{\mathrm{vac}} \cos \Delta_{31}}. \tag{6.25}$$

The smooth limit to the sign-Δm_{31}^2 degenerate solution in vacuum can be achieved by taking the sign convention

$$s_{\mathrm{III}}^2 = \frac{1}{2T_{\mathrm{sign}}} \left[U_{\mathrm{sign}\pm} - d_\pm^{\mathrm{sign}} \sqrt{\frac{D_\pm^{\mathrm{sign}}}{(d_\pm^{\mathrm{sign}})^2}} \right],$$

$$s_{\mathrm{IV}}^2 = \frac{1}{2T_{\mathrm{sign}}} \left[U_{\mathrm{sign}\pm} + d_\pm^{\mathrm{sign}} \sqrt{\frac{D_\pm^{\mathrm{sign}}}{(d_\pm^{\mathrm{sign}})^2}} \right]. \tag{6.26}$$

It is obvious that the positive or negative Δm_{31}^2 ellipses get separated due to the larger matter effect at longer baselines. In (6.26) we have taken the convention such that in $a \to 0$ limit s_{III} and s_{IV} smoothly tend to the vacuum solution $s_{\mathrm{III}}^{\mathrm{vac}}$ and $s_{\mathrm{IV}}^{\mathrm{vac}}$, respectively. Once the solutions of s_3 are specified with the well defined convention the solutions δ_{III} and δ_{IV} can be obtained by inserting s_{III} and s_{IV}, respectively, into (6.18).

Despite the discontinuity of degenerate solution exist, we take the convention B because of number of desirable features. The matter perturbation theory of degenerate solution [85, 86] which will be derived in following subsection can be formulated only with this convention because it requires the existence of smooth limit $a \to 0$ in each solution. More importantly, another reason is that the convention B makes the structure of the degenerate solution more transparent. If we denote s_{III} in (6.26) and δ_{III} in (6.18) in the function as

$$s_{\mathrm{III}} = \xi_\pm^{\mathrm{CP\ sign}}(s_1, \delta_1), \qquad \delta_{\mathrm{III}} = \eta_\pm^{\mathrm{CP\ sign}}(s_1, \delta_1). \tag{6.27}$$

Then, one can show that

$$s_{\mathrm{IV}} = \xi_\pm^{\mathrm{CP\ sign}}(s_{\mathrm{II}}, \delta_{\mathrm{II}}), \qquad \delta_{\mathrm{IV}} = \eta_\pm^{\mathrm{CP\ sign}}(s_{\mathrm{II}}, \delta_{\mathrm{II}}). \tag{6.28}$$

In this sense there is the one-to-one correspondence between the (true, intrinsic degeneracy solution) and two sign-Δm_{31}^2 degeneracy solutions.

However, there exists a somewhat disturbing feature of this convention; As we mentioned, the solutions have discontinuity as a function of oscillation parameters. But it does not means that the solutions defined by convention B are unphysical. The discontinuity means that the two solutions interchange themselves at the discontinuous point (See Fig. 6.6).

Matter perturbation formula of sign-Δm_{31}^2 solutions

At the end of this subsection, we derive the matter perturbation formula of the sign-Δm_{31}^2 solution. As we saw at subsection 6.1.1, sign-Δm_{31}^2 degenerate solution in vacuum is very simple. Considering the some future long baseline experiments have small matter effect as

$$\epsilon_{\mathrm{MP}} \equiv \frac{A}{|\Delta_{31}|} \ll 1, \tag{6.29}$$

like

$$\epsilon_{\mathrm{MP}} \simeq 0.085 \left(\frac{\rho}{2.8 \mathrm{g/cc}} \right) \left(\frac{E}{1 \mathrm{GeV}} \right), \tag{6.30}$$
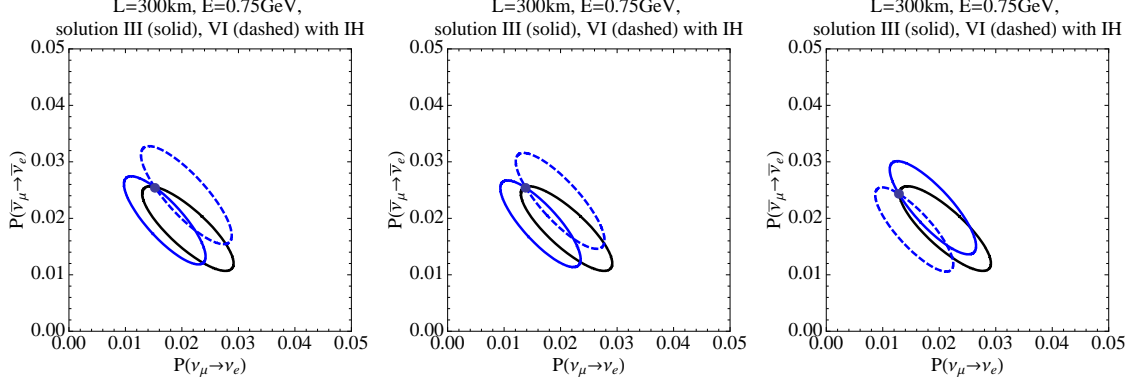
Figure 6.6: The example of discontinuity point in the $P - P^{CP}$ bi-probability space. Black ellipse is drawn with $\sin^2 2\theta_{13} = 0.05$ and normal hierarchy. Blue solid and dashed line with inverted hierarchy. Changing the true value of δ (left to right), the role of two blue ellipse which is III or VI exchange each other.

where ρ is the averaged matter density along the neutrino trajectory.

Perturbing (6.26) with ϵ_{MP} parameter, we obtain the perturbative formula of $\sin^2 2\theta_{13}^{\mathrm{III}}$

$$
\sin^2 2\theta_{13}^{\mathrm{III}}
= \sin^2 2\theta_{13}^1 \left(1 + \frac{A}{\Delta_{31}} \frac{4\sin\delta_1(\Delta_{31}\cos\Delta_{31} - \sin\Delta_{31})(\pm s_1 X_{\mathrm{vac}}\cos\Delta_{31} + Z_{\mathrm{vac}}\cos\delta_1)}{\sin^2\Delta_{31}(\pm 2s_1 X_{\mathrm{vac}}\cos\delta_1 + Z_{\mathrm{vac}}\cos\Delta_{31})} \right)
\tag{6.31}
$$

and

$$
\begin{aligned}
\cos\delta_{\mathrm{III}} &= -\cos\delta_1 \\
&\quad + 2\frac{A}{\Delta_{31}} \frac{\sin\delta_1(\Delta_{31}\cos\Delta_{31} - \sin\Delta_{31})}{\sin^2\Delta_{31}} \\
&\quad \times \frac{s_1^2 X_{\mathrm{vac}}^2 + Z_{\mathrm{vac}}^2\cos(\delta_1 \mp \Delta_{31})\cos(\delta_1 \pm \Delta_{31}) \pm 2s_1 X_{\mathrm{vac}} Z_{\mathrm{vac}}\cos\delta_1\cos\Delta_{31}}{(\pm s_1 X_{\mathrm{vac}} Z_{\mathrm{vac}}\cos\delta_1 + Z_{\mathrm{vac}}^2\cos\Delta_{31})} \\
\sin\delta_{\mathrm{III}} &= \sin\delta_1 \\
&\quad + 2\frac{A}{\Delta_{31}} \frac{\cos\delta_1(\Delta_{31}\cos\Delta_{31} - \sin\Delta_{31})}{\sin^2\Delta_{31}} \\
&\quad \times \frac{s_1^2 X_{\mathrm{vac}}^2 + Z_{\mathrm{vac}}^2\cos(\delta_1 \mp \Delta_{31})\cos(\delta_1 \pm \Delta_{31}) \pm 2s_1 X_{\mathrm{vac}} Z_{\mathrm{vac}}\cos\delta_1\cos\Delta_{31}}{(\pm s_1 X_{\mathrm{vac}} Z_{\mathrm{vac}}\cos\delta_1 + Z_{\mathrm{vac}}^2\cos\Delta_{31})},
\end{aligned}
\tag{6.32}
$$

where, X_{vac} and Z_{vac} are same in Section 6.1.1. Note that the first terms are nothing but the solution in vacuum.

Thanks to the relation of one to one correspondence, one can easily obtain the formula of $\theta_{13}^{\mathrm{IV}}$ and δ_{IV} by exchanging $(s_1, \delta_1) \to (s_{\mathrm{II}}, \delta_{\mathrm{II}})$ of (6.31) and (6.32) respectively.

6.1.4 Intrinsic degeneracy across the θ_{23} octant in matter

In this and the following two subsections, we discuss the parameter degeneracy caused by the ambiguity of which octant θ_{23} lives, assuming that $\theta_{23} \neq \pi/4$. Our treatment of the octant degeneracy will be done under the approximation that the two solutions of θ_{23} has the same value of $\sin 2\theta_{23}$. If we introduce $X'_{\pm}$ and Z' as

$$
\begin{aligned}
X'_{\pm} &\equiv X_{\pm}/s_{23} = \frac{\Delta_{31} \sin(\Delta_{31} \mp A)}{(\Delta_{31} \mp A)}, \\
Z' &\equiv Z/c_{23} = \sin 2\theta_{12} \frac{\Delta_{21} \sin A}{A}
\end{aligned}
\tag{6.33}
$$

$X_{\pm}$ and Z for the true and the false θ_{23} octant solutions are given by

$$
\begin{aligned}
X^{\text{true}}_{\pm} = s_{23} X'_{\pm} &\quad, \quad X^{\text{false}}_{\pm} = c_{23} X'_{\pm} \\
Z^{\text{true}} = c_{23} Z' &\quad, \quad Z^{\text{false}}_{\prime} = s_{23} Z'.
\end{aligned}
\tag{6.34}
$$
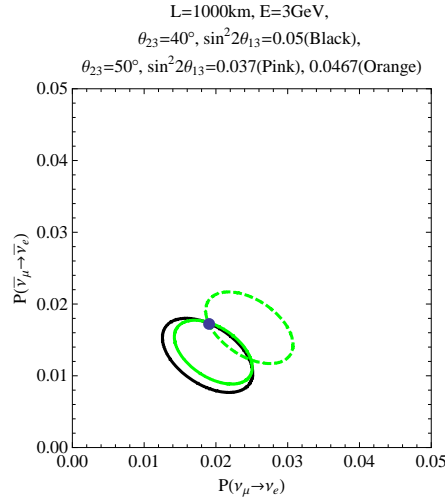
Figure 6.7: Bi-probability plot for octant degeneracy. Black ellipse : $\sin^2 2\theta^1_{13} = 0.05$ with first octant ($\theta_{23} = 40°$) and normal hierarchy. Green solid (dashed) ellipse : $\sin^2 2\theta^{\text{V,VI}}_{13} = 0.037(0.0467)$ with second octant ($\theta_{23} = 50°$) and normal hierarchy.

We first discuss the case in which the intrinsic degeneracy solutions exist in different θ_{23} octants (See Fig. 6.7). The input solution (s_1, δ_1) and the different octant clone solution (s_5, δ_5) satisfy the following equations

$$
\begin{aligned}
P &= s^2_{23} X'^2_{\pm} s^2_1 \pm 2 s_{23} c_{23} X'_{\pm} Z' s_1 \left(\cos \delta_1 \cos \Delta_{31} \mp \sin \delta_1 \sin \Delta_{31}\right) + c^2_{23} Z'^2, \\
&= c^2_{23} X'^2_{\pm} s^2_5 \pm 2 s_{23} c_{23} X'_{\pm} Z' s_5 \left(\cos \delta_5 \cos \Delta_{31} \mp \sin \delta_5 \sin \Delta_{31}\right) + s^2_{23} Z'^2,
\end{aligned}
\tag{6.35}
$$

in the neutrino channel, and

$$
\begin{aligned}
P^{CP} &= s^2_{23} X'^2_{\mp} s^2_1 \pm 2 s_{23} c_{23} X'_{\mp} Z' s_1 \left(\cos \delta_1 \cos \Delta_{31} \pm \sin \delta_1 \sin \Delta_{31}\right) + c^2_{23} Z'^2, \\
&= c^2_{23} X'^2_{\mp} s^2_5 \pm 2 s_{23} c_{23} X'_{\mp} Z' s_5 \left(\cos \delta_5 \cos \Delta_{31} \pm \sin \delta_5 \sin \Delta_{31}\right) + s^2_{23} Z'^2.
\end{aligned}
\tag{6.36}
$$

in the CP-conjugated channel. The way of obtaining s_5 and δ_5 is same as the sign-Δm_{31}^2 degeneracy solutions in Sec. 6.1.3. Combining (6.35) and (6.36) assuming $X'_\pm \neq 0$, we obtain the equations for δ_5 as

$$
\begin{aligned}
s_5 \cos \delta_5 &= s_1 \cos \delta_1 \pm \frac{(s_{23}^2 s_1^2 - c_{23}^2 s_5^2)(X'_\pm + X'_\mp)}{4 s_{23} \cos \Delta_{31}} \pm Z' \frac{(c_{23}^2 - s_{23}^2)(\frac{1}{X'_\pm} + \frac{1}{X'_\mp})}{4 c_{23} \cos \Delta_{31}} \\
s_5 \sin \delta_5 &= s_1 \sin \delta_1 + \frac{(s_{23}^2 s_1^2 - c_{23}^2 s_5^2)(X'_\pm + X'_\mp)}{4 s_{23} \sin \Delta_{31}} - Z' \frac{(c_{23}^2 - s_{23}^2)(\frac{1}{X'_\pm} + \frac{1}{X'_\mp})}{4 c_{23} \sin \Delta_{31}} \quad (6.37)
\end{aligned}
$$

Inserting (6.37) into $\cos^2 \delta_5 + \sin^2 \delta_5 = 1$ we obtain the quartic equation for s_5 as

$$
T_{\mathrm{oct}} s_5^4 - U_{\mathrm{oct}\pm} s_5^2 + V_{\mathrm{oct}\pm} = 0 \qquad (6.38)
$$

which is actually a quadratic equation of s_{13}^2 because of the quadratic dependence on s_{13} of $s_5 \cos \delta_5$ and $s_5 \sin \delta_5$. Thus, there exist only two physical solutions, which implies that the octant degeneracy in the same hierarchy is two-fold. The definition of T_{oct} etc. is given as

$$
T_{\mathrm{oct}} \equiv \left(\frac{c_{23}}{4 s_{23} Z'} \right)^2 \left[\left(\frac{X'_+ + X'_-}{\cos \Delta_{31}} \right)^2 + \left(\frac{X'_+ - X'_-}{\sin \Delta_{31}} \right)^2 \right] \qquad (6.39)
$$

$$
\begin{aligned}
U_{\mathrm{oct}\pm} \equiv{}& 1 + \frac{1}{8} \left(\frac{X'_\pm - X'_\mp}{\sin^2 \Delta_{31}} \right)^2 \left(\frac{s_1^2}{Z'^2} - \frac{\cos 2\theta_{23}}{s_{23}^2 X'_\pm X'_\mp} \right) + \frac{1}{8} \left(\frac{X'_\pm + X'_\mp}{\cos^2 \Delta_{31}} \right)^2 \left(\frac{s_1^2}{Z'^2} + \frac{\cos 2\theta_{23}}{s_{23}^2 X'_\pm X'_\mp} \right) \\
&- \frac{c_{23} s_1}{s_{23} Z' \sin 2\Delta_{31}} \{ X'_\pm \sin(\delta_1 \mp \Delta_{31}) - X'_\mp \sin(\delta_1 \pm \Delta_{31}) \} \qquad (6.40)
\end{aligned}
$$

$$
\begin{aligned}
V_{\mathrm{oct}\pm} \equiv{}& s_1^2 + \left(\frac{(X'_\pm + X'_\mp)(s_1^2 s_{23}^2 X'_\pm X'_\mp + \cos 2\theta_{23} Z'^2)}{2 \sin 2\theta_{23} X'_\pm X'_\mp Z' \cos \Delta_{31}} \right)^2 \\
&\pm \left(\frac{(X'_\pm + X'_\mp)(s_1^2 s_{23}^2 X'_\pm X'_\mp + \cos 2\theta_{23} Z'^2)}{\sin 2\theta_{23} X'_\pm X'_\mp Z' \cos \Delta_{31}} \right) \cos \delta_1 \\
&+ \left(\frac{(X'_\pm - X'_\mp)(s_1^2 s_{23}^2 X'_\pm X'_\mp - \cos 2\theta_{23} Z'^2)}{2 \sin 2\theta_{23} X'_\pm X'_\mp Z' \sin \Delta_{31}} \right)^2 \\
&+ \left(\frac{(X'_\pm - X'_\mp)(s_1^2 s_{23}^2 X'_\pm X'_\mp - \cos 2\theta_{23} Z'^2)}{\sin 2\theta_{23} X'_\pm X'_\mp Z' \sin \Delta_{31}} \right) \sin \delta_1 \qquad (6.41)
\end{aligned}
$$

Then, the octant degeneracy solution s_5 is given by

$$
s_5^2 = \frac{1}{2 T_{\mathrm{oct}}} \left[U_{\mathrm{oct}\pm} \, [\pm]^* \sqrt{D_\pm^{\mathrm{oct\text{-}intr}}} \right], \qquad (6.42)
$$

where $[\pm]^*$ is the temporary sign to be specified below and $D_\pm^{\mathrm{oct\text{-}intr}}$ is defined as

$$
D_\pm^{\mathrm{oct\text{-}intr}} = U_{\mathrm{oct}\pm}^2 - 4 T_{\mathrm{oct}} V_{\mathrm{oct}\pm} \qquad (6.43)
$$
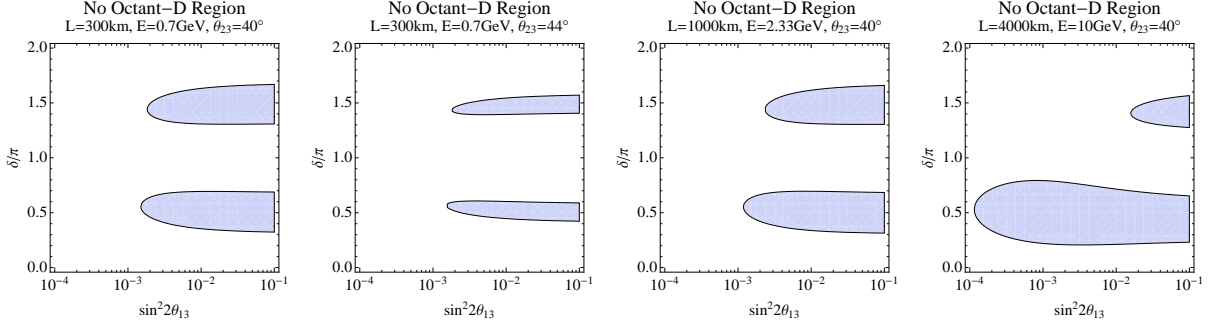
Figure 6.8: Depicted as the shaded region in the $\sin^2 2\theta_{13} - \delta/\pi$ space is the region where no θ_{23} octant degeneracy solution exists for baselines and neutrino energies typical to superbeam or neutrino factory settings. The true mass hierarchy is taken to be the normal.

If $D_\pm^{\text{oct-intr}} \le 0$, there is no octant degeneracy. The region of no θ_{23} octant degeneracy solution is displayed in Fig. 6.8 by taking $\theta_{23}^{\text{true}}$ in first octant.

One can realize from the left and second panel of Fig. 6.8 that reaching the maximal mixing value of θ_{23}, the region of no-octant degeneracy shrinks.

In addition, the regions of no-octant degeneracy are around $\delta \sim \pi/2$ and $3\pi/2$ that disappear into the small θ_{13} as $\sin^2 2\theta_{13} \sim 10^{-3}$. The feature can be easily understood by the bi-probability plot, the right panel of Fig. 6.9. The octant degeneracy exists the region overlapping blue ($\theta_{23} = 40°$) and red ($\theta_{23} = 90° - 40°$). The blue and red solid line show the region of $\delta = 0$, $\theta_{23}^{\text{true}} = 40°$ (blue) does not have the octant degeneracy around $\delta = \pm\pi/2$ with large θ_{13}.

The bi-probability plot also tells us the difference between the features of the octant degeneracy with true θ_{23} in the first and the second octants. The left panel of Fig. 6.9 shows the region of no degenerate solution with θ_{23} in the second octant. The location and the shape of no-solution region is completely different from the ones in the first octant. Note the region of small P and P^{CP}; i.e. small θ_{13}, there are the region where the red shadowed region only exists. Therefore, if θ_{23} lives in second octant, octant degeneracy exists all value of δ with large θ_{23} as $\sin^2 2\theta_{13} \gtrsim 10^{-3}$.

Problem of convention of labeling the octant degeneracy solution

Now, we have to revisit the issue of convention to define unambiguously the octant degeneracy solutions. We use the following new convention :

Convention C: We define (s_V, δ_V) and (s_{VI}, δ_{VI}) such that they have a smooth limit to the true and intrinsic degeneracy solutions (s_1, δ_1) and (s_{II}, δ_{II}), respectively, when the maximum θ_{23} limit $\theta_{23} \to \pi/4$ is taken. It can be understood as a consistency condition.

In the maximum θ_{23} limit, $D_\pm^{\text{oct-intr}}$ can be written by

$$D_\pm^{\text{oct-intr-max}} \equiv \lim_{\theta_{23} \to \pi/4} D_\pm^{\text{oct-intr}} = (d_\pm^{\text{oct-intr}})^2 \tag{6.44}$$
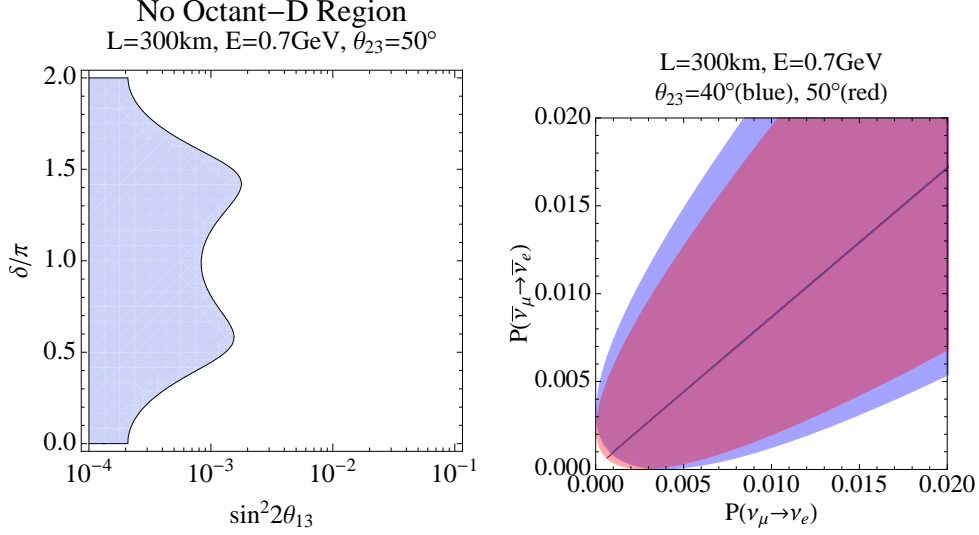
Figure 6.9: Left : the region where no θ_{23} octant degeneracy exists for $\theta_{23}^{\text{true}} = 50°$ with normal hierarchy. Right : Shown by the blue and the red shaded areas in the $P - P^{CP}$ bi-probability space are the regions spanned by the ellipses with $\theta_{23} = 40$ and 50 degrees, respectively.

where

$$
d_{\pm}^{\text{oct-intr}} \equiv 1 + s_1 \frac{X'_{\mp}\sin(\delta_1 \pm \Delta_{31}) - X'_{\pm}\sin(\delta_1 \mp \Delta_{31})}{Z'\sin 2\Delta_{31}} \tag{6.45}
$$

The smooth limit to the same-octant intrinsic degeneracy solution can be achieved by taking the sign convention

$$
\begin{aligned}
s_{\text{V}}^2 &= \frac{1}{2T_{\text{oct}}}\left[U_{\text{oct}\pm} - d_{\pm}^{\text{oct-intr}}\sqrt{\frac{D_{\pm}^{\text{oct-intr}}}{(d_{\pm}^{\text{oct-intr}})^2}}\right], \\
s_{\text{VI}}^2 &= \frac{1}{2T_{\text{oct}}}\left[U_{\text{oct}\pm} + d_{\pm}^{\text{oct-intr}}\sqrt{\frac{D_{\pm}^{\text{oct-intr}}}{(d_{\pm}^{\text{oct-intr}})^2}}\right].
\end{aligned} \tag{6.46}
$$

One can easily verify that in the maximum θ_{23} limit s_{V} and s_{VI} tend to s_1 and s_{II}, respectively.

If we denote the function in the first line of (6.46) and the ones for δ in (6.37) as

$$
s_{\text{V}} = \xi_{\pm}^{\text{CP oct}}(s_1, \delta_1), \qquad \delta_{\text{V}} = \eta_{\pm}^{\text{CP oct}}(s_1, \delta_1). \tag{6.47}
$$

Then, one can show that s_{IV} and δ_{IV} can be written as

$$
s_{\text{VI}} = \xi_{\pm}^{\text{CP oct}}(s_{\text{II}}, \delta_{\text{II}}), \qquad \delta_{\text{VI}} = \eta_{\pm}^{\text{CP oct}}(s_{\text{II}}, \delta_{\text{II}}). \tag{6.48}
$$

Maximal θ_{23} perturbation of octant degeneracy solution

At the end of this subsection, we derive the maximal θ_{23} perturbation formula of octant degeneracy solutions. Assuming that the true value of θ_{23} is close to $\frac{\pi}{4}$, we denote the difference from maximal as

$$\theta_{23}^{\text{true}} = \frac{\pi}{4} + \epsilon_{\text{oct}}. \tag{6.49}$$

Expanding (6.46) by ϵ_{oct}, we obtain

$$
\begin{aligned}
\sin^2 2\theta_{13}^{\text{V}} = \;& \sin^2 2\theta_{13}^1 (1 + 4\epsilon_{\text{oct}}) \\
& + 4\epsilon_{\text{oct}} s_1 Z' \frac{s_1 X'_\pm X'_\mp \sin 2\Delta_{31} + X'_\pm Z' \sin(\delta_1 \pm \Delta_{31}) - X'_\mp Z' \sin(\delta_1 \mp \Delta_{31})}{X'_\pm X'_\mp \{ s_1 X'_\pm \sin(\delta_1 \mp \Delta_{31}) - s_1 X'_\mp \sin(\delta_1 \pm \Delta_{31}) - Z' \sin 2\Delta_{31} \}}
\end{aligned}
\tag{6.50}
$$

and

$$
\begin{aligned}
\cos \delta_{\text{V}} = \;& \cos \delta_1 - 2\epsilon_{\text{oct}} \sin \delta_1 \\
& \times \frac{(s_1^2 X'^2_\mp - Z'^2) X'_+ \cos(\delta_1 \pm \Delta_{31}) - (s_1^2 X'^2_\pm - Z'^2) X'_\mp \cos(\delta_1 \mp \Delta_{31}) \pm s_1 Z' (X'^2_\pm - X'^2_\mp)}{s_1 X'_\pm X'_\mp \Big\{ s_1 X'_\mp \sin(\delta_1 \pm \Delta_{31}) - s_1 X'_\pm \sin(\delta_1 \mp \Delta_{31}) + Z' \sin 2\Delta_{31} \Big\}} \\
\sin \delta_{\text{V}} = \;& \sin \delta_1 + 2\epsilon_{\text{oct}} \cos \delta_1 \\
& \times \frac{(s_1^2 X'^2_\mp - Z'^2) X'_+ \cos(\delta_1 \pm \Delta_{31}) - (s_1^2 X'^2_\pm - Z'^2) X'_\mp \cos(\delta_1 \mp \Delta_{31}) \pm s_1 Z' (X'^2_\pm - X'^2_\mp)}{s_1 X'_\pm X'_\mp \Big\{ s_1 X'_\mp \sin(\delta_1 \pm \Delta_{31}) - s_1 X'_\pm \sin(\delta_1 \mp \Delta_{31}) + Z' \sin 2\Delta_{31} \Big\}}.
\end{aligned}
\tag{6.51}
$$

One can obtain the solution for VI by exchanging $(s_1, \delta_1) \to (s_{\text{II}}, \delta_{\text{II}})$. Note that limit of maximal θ_{23}; $\epsilon_{\text{oct}} \to 0$ leads the true value of (θ_{13}, δ) for the solution V and $(\theta_{\text{II}}, \delta_{\text{II}})$ for the solution VI.

6.1.5 Sign-Δm_{31}^2 degeneracy across the θ_{23} octant in matter

We next discuss the sign-Δm_{31}^2 degeneracy across the θ_{23} octant displayed in Fig. 6.10.

The input solution (s_1, δ_1) and the different octant clone solution (s_7, δ_7) satisfy the following equations

$$
\begin{aligned}
P &= s_{23}^2 X'^2_\pm s_1^2 \pm 2 s_{23} c_{23} X'_\pm Z' s_1 (\cos \delta_1 \cos \Delta_{31} \mp \sin \delta_1 \sin \Delta_{31}) + c_{23}^2 Z'^2, \\
&= c_{23}^2 X'^2_\mp s_7^2 \mp 2 s_{23} c_{23} X'_\mp Z' s_7 (\cos \delta_7 \cos \Delta_{31} \pm \sin \delta_7 \sin \Delta_{31}) + s_{23}^2 Z'^2,
\end{aligned}
\tag{6.52}
$$

in the neutrino channel, and

$$
\begin{aligned}
P^{CP} &= s_{23}^2 X'^2_\mp s_1^2 \pm 2 s_{23} c_{23} X'_\mp Z' s_1 (\cos \delta_1 \cos \Delta_{31} \pm \sin \delta_1 \sin \Delta_{31}) + c_{23}^2 Z'^2, \\
&= c_{23}^2 X'^2_\pm s_7^2 \mp 2 s_{23} c_{23} X'_\pm Z' s_7 (\cos \delta_7 \cos \Delta_{31} \mp \sin \delta_7 \sin \Delta_{31}) + s_{23}^2 Z'^2. \tag{6.53}
\end{aligned}
$$

L=1000km, E=3GeV,
$\theta_{23}=40°$, $\sin^2 2\theta_{13}=0.05$(Black) w/ NH,
$\theta_{23}=50°$, $\sin^2 2\theta_{13}=0.0398$(Pink), 0.0421(Orange) w/ IH
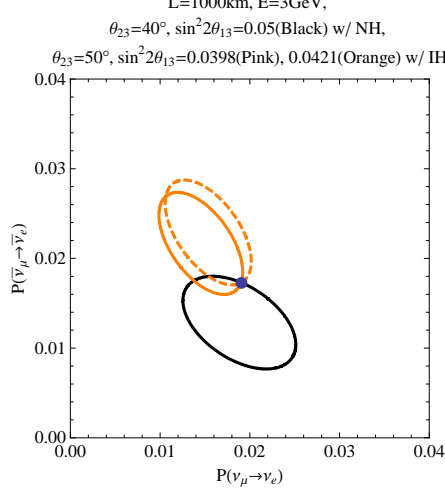
Figure 6.10: Bi-probability plot for octant degeneracy. Black ellipse : $\sin^2 2\theta_{13}^{\rm I} = 0.05$ with first octant ($\theta_{23} = 40°$) and normal hierarchy. Orange solid (dashed) ellipse : $\sin^2 2\theta_{13}^{\rm V,VI} = 0.0398(0.0421)$ with second octant ($\theta_{23} = 50°$) and inverted hierarchy.

in the CP-conjugated channel. Proceeding along the same way as in Secs. 6.1.3 and 6.1.4 we obtain

$$
\begin{aligned}
s_7 \cos \delta_7 &= \frac{-1}{4s_{23}c_{23}X'_\pm X'_\mp Z' \cos \Delta_{31}} \Big[2s_{23}c_{23}s_1 Z' \left\{ X'^2_\pm \cos(\delta_1 \pm \Delta_{31}) + X'^2_\mp \cos(\delta_1 \mp \Delta_{31}) \right\} \\
&\quad \pm (X'_\pm + X'_\mp)\{ Z'^2 \cos 2\theta_{23} + s_{23}^2 s_1^2 (X'^2_\pm + X'^2_\mp) - X'_\pm X'_\mp (s_{23}^2 s_1^2 + c_{23}^2 s_7^2) \} \Big] \\
s_7 \sin \delta_7 &= \frac{\mp 1}{4s_{23}c_{23}X'_\pm X'_\mp Z' \sin \Delta_{31}} \Big[2s_{23}c_{23}s_1 Z' \left\{ X'^2_\pm \cos(\delta_1 \pm \Delta_{31}) - X'^2_\mp \cos(\delta_1 \mp \Delta_{31}) \right\} \\
&\quad \pm (X'_\pm - X'_\mp)\{ Z'^2 \cos 2\theta_{23} + s_{23}^2 s_1^2 (X'^2_\pm + X'^2_\mp) + X'_\pm X'_\mp (s_{23}^2 s_1^2 + c_{23}^2 s_7^2) \} \Big] . (6.54)
\end{aligned}
$$

Inserting (6.54) into $\sin^2 \delta_7 + \cos^2 \delta_7 = 1$, we obtain the quartic equation of s_{13},

$$
T_{\rm sign\text{-}oct} s_7^4 - U_{\rm sign\text{-}oct\pm} s_7^2 + V_{\rm sign\text{-}oct\pm} = 0 \tag{6.55}
$$

which is actually a quadratic equation of s_{13}^2 because of the quadratic dependence on s_{13} of $s_7 \cos \delta_7$ and $s_7 \sin \delta_7$. Thus, there exist only two physical solutions, which implies that the octant degeneracy in different hierarchy is two-fold. In (6.55) $T_{\rm sign\text{-}oct}$ etc. are defined as

$$
T_{\rm sign\text{-}oct} \equiv \left(\frac{c_{23}(X'_+ - X'_-)}{4s_{23}Z' \sin \Delta_{31}} \right)^2 + \left(\frac{c_{23}(X'_+ + X'_-)}{4s_{23}Z' \cos \Delta_{31}} \right)^2 \tag{6.56}
$$

54

$$
\begin{aligned}
U_{\text{sign-oct}\pm} \quad \equiv \quad & 1 \\
& \pm \frac{1}{8 s_{23}^2 X'_\pm X'_\mp Z'^2 \sin^2 \Delta_{31}} \Big[2 s_{23} c_{23} s_1 Z' \left\{ X'^2_\pm \cos(\delta_1 \pm \Delta_{31}) - X'^2_\mp \cos(\delta_1 \mp \Delta_{31}) \right\} \\
& \quad \pm (X'_\pm - X'_\mp)\{ Z'^2 \cos 2\theta_{23} + s_{23}^2 s_1^2 (X'^2_\pm + X'_\pm X'_\mp + X'^2_\mp) \} \Big] \\
& + \frac{1}{8 s_{23}^2 X'_\pm X'_\mp Z'^2 \cos^2 \Delta_{31}} \Big[2 s_{23} c_{23} s_1 Z' \left\{ X'^2_\pm \cos(\delta_1 \pm \Delta_{31}) + X'^2_\mp \cos(\delta_1 \mp \Delta_{31}) \right\} \\
& \quad \pm (X'_\pm + X'_\mp)\{ Z'^2 \cos 2\theta_{23} + s_{23}^2 s_1^2 (X'^2_\pm - X'_\pm X'_\mp + X'^2_\mp) \} \Big] \quad (6.57)
\end{aligned}
$$

$$
\begin{aligned}
V_{\text{sign-oct}\pm} \quad \equiv \quad & \left(\frac{1}{4 s_{23} c_{23} X'_\pm X'_\mp Z' \cos \Delta_{31}} \Big[2 s_{23} c_{23} s_1 Z' \left\{ X'^2_\pm \cos(\delta_1 \pm \Delta_{31}) + X'^2_\mp \cos(\delta_1 \mp \Delta_{31}) \right\} \right. \\
& \quad \left. \pm (X'_\pm + X'_\mp)\{ Z'^2 \cos 2\theta_{23} + s_{23}^2 s_1^2 (X'^2_\pm - X'_\pm X'_\mp + X'^2_\mp) \} \Big] \right)^2 \\
& + \left(\frac{1}{4 s_{23} c_{23} X'_\pm X'_\mp Z' \sin \Delta_{31}} \Big[2 s_{23} c_{23} s_1 Z' \left\{ X'^2_\pm \cos(\delta_1 \pm \Delta_{31}) - X'^2_\mp \cos(\delta_1 \mp \Delta_{31}) \right\} \right. \\
& \quad \left. \pm (X'_\pm - X'_\mp)\{ Z'^2 \cos 2\theta_{23} + s_{23}^2 s_1^2 (X'^2_\pm + X'_\pm X'_\mp + X'^2_\mp)) \} \Big] \right)^2 . \quad (6.58)
\end{aligned}
$$

Then, the sign-Δm_{31}^2 degeneracy solution across θ_{23} octant is given by

$$
s_7^2 = \frac{1}{2 T_{\text{sign-oct}}} \left[U_{\text{sign-oct}\pm} \, [\pm]^* \, \sqrt{D_\pm^{\text{sign-oct}}} \right], \quad (6.59)
$$

where $[\pm]^*$ is the temporary sign to be specified below and $D_\pm^{\text{sign-oct}}$ is defined as

$$
D_\pm^{\text{sign-oct}} \quad \equiv \quad U_{\text{sign-oct}\pm}^2 - 4 T_{\text{sign-oct}} U_{\text{sign-oct}\pm} \quad (6.60)
$$

If $D_\pm^{\text{sign-oct}} \leq 0$, it means that there is no degenerate solutions in sign-octant degeneracy. The region of no sign-octant degeneracy solution is displayed in Fig. 6.11. The feature of the region can also be understood by the bi-probability plots as in the previous subsection. Once there is a solution, the same argument as before assures that the solutions for s_7^2 in (6.59) are positive definite.

Problem of convention of labeling the sign-octant degeneracy solution

To define unambiguously the sign-Δm_{31}^2 degeneracy solutions across θ_{23} octant we need the following new convention. That is, we need to take both the maximum θ_{23} and the vacuum limits.

Convention D: We take the convention such that $(s_{\text{VII}}, \delta_{\text{VII}})$ and $(s_{\text{VIII}}, \delta_{\text{VIII}})$ tend to $(s_{\text{III}}^{\text{vac}}, \delta_{\text{III}}^{\text{vac}})$ and $(s_{\text{IV}}^{\text{vac}}, \delta_{\text{IV}}^{\text{vac}})$, respectively, in the simultaneous maximum-θ_{23} and the vacuum limit.
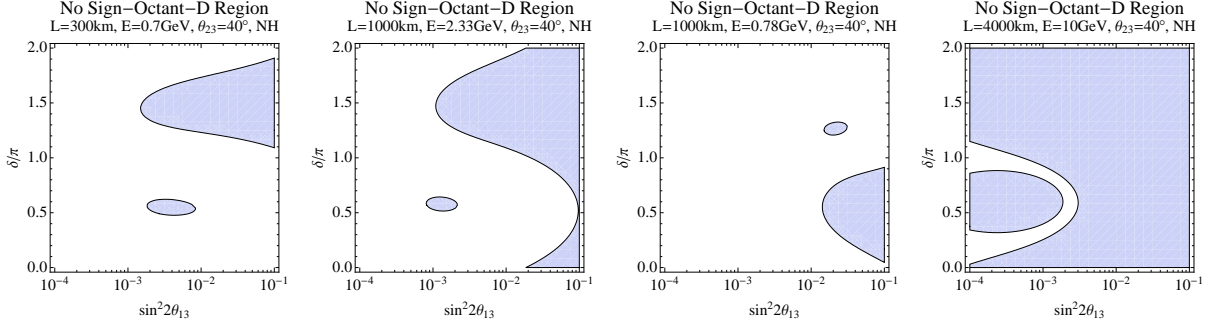
Figure 6.11: Depicted as the shaded region in the $\sin^2 2\theta_{13} - \delta/\pi$ space is the region where no solution of the sign-Δm_{31}^2 degeneracy across θ_{23} octant exists. The true mass hierarchy is taken to be the normal one.

One can easily show in the combined limit that $\lim_{\theta_{23}\to\pi/4, a\to 0} D_{\pm}^{\text{sign-oct}} = (d_{\pm}^{\text{sign-oct}})^2$, where $d_{\pm}^{\text{sign-oct}}$ has the same form $d_{\pm}^{\text{sign}}$ defined in (6.25) except for taking $\theta_{23} = \pi/4$ of it. Therefore, the temporary sign of (6.59) is determined by this convention, we have

$$
\begin{aligned}
s_{\text{VII}}^2 &= \frac{1}{2T_{\text{sign-oct}}}\left[U_{\text{sign-oct}\pm} - d_{\pm}^{\text{sign-oct}}\sqrt{\frac{D_{\pm}^{\text{sign-oct}}}{(d_{\pm}^{\text{sign-oct}})^2}}\right], \\
s_{\text{VIII}}^2 &= \frac{1}{2T_{\text{sign-oct}}}\left[U_{\text{sign-oct}\pm} + d_{\pm}^{\text{sign-oct}}\sqrt{\frac{D_{\pm}^{\text{sign-oct}}}{(d_{\pm}^{\text{sign-oct}})^2}}\right].
\end{aligned}
\tag{6.61}
$$

In this convention, we determine the function of first line of (6.61) and for δ in (6.54) as

$$
s_{\text{VII}} = \xi_{\pm}^{\text{CP sign-oct}}(s_1, \delta_1), \qquad \delta_{\text{VII}} = \eta_{\pm}^{\text{CP sign-oct}}(s_1, \delta_1).
\tag{6.62}
$$

Then, one can show that

$$
s_{\text{VIII}} = \xi_{\pm}^{\text{CP sign-oct}}(s_{\text{II}}, \delta_{\text{II}}), \qquad \delta_{\text{VIII}} = \eta_{\pm}^{\text{CP sign-oct}}(s_{\text{II}}, \delta_{\text{II}}).
\tag{6.63}
$$

6.2 Structure of parameter degeneracy

In this section, we discuss the structure of parameter degeneracy which describe the relationships between the degenerate solutions.

First, we show the structure of eightfold degeneracy, and we summarize the relationship of the solutions with the normal and the inverted hierarchies.

6.2.1 Mappings between the true and the degeneracy solutions

First, we show the relationship between each intrinsic degeneracy pair of the solutions in order. If we denote the relationship between the intrinsic degeneracy solution derived in

Sec. 6.1.2 as $s_{\mathrm{II}} = \xi_\pm^{\mathrm{CP\ intr}}(s_1, \delta_1, \theta_{23}^{\mathrm{true}})$ and $\delta_{\mathrm{II}} = \eta_\pm^{\mathrm{CP\ intr}}(s_1, \delta_1, \theta_{23}^{\mathrm{true}})$ then the other intrinsic degeneracy pairs of the solutions satisfy

$$
\begin{aligned}
s_{\mathrm{IV}} &= \xi_\mp^{\mathrm{CP\ intr}}(s_{\mathrm{III}}, \delta_{\mathrm{III}}, \theta_{23}^{\mathrm{true}}), & \delta_{\mathrm{IV}} &= \eta_\mp^{\mathrm{CP\ intr}}(s_{\mathrm{III}}, \delta_{\mathrm{III}}, \theta_{23}^{\mathrm{true}}), \\
s_{\mathrm{VI}} &= \xi_\pm^{\mathrm{CP\ intr}}(s_{\mathrm{V}}, \delta_{\mathrm{V}}, \pi/2 - \theta_{23}^{\mathrm{true}}), & \delta_{\mathrm{VI}} &= \eta_\pm^{\mathrm{CP\ intr}}(s_{\mathrm{V}}, \delta_{\mathrm{V}}, \pi/2 - \theta_{23}^{\mathrm{true}}), \\
s_{\mathrm{VIII}} &= \xi_\mp^{\mathrm{CP\ intr}}(s_{\mathrm{VII}}, \delta_{\mathrm{VII}}, \pi/2 - \theta_{23}^{\mathrm{true}}), & \delta_{\mathrm{VIII}} &= \eta_\mp^{\mathrm{CP\ intr}}(s_{\mathrm{VII}}, \delta_{\mathrm{VII}}, \pi/2 - \theta_{23}^{\mathrm{true}}).
\end{aligned}
\tag{6.64}
$$

The reason that first line of (6.64) does not have the hierarchy sign $\pm$ but $\mp$ can be understood as following. If the true mass hierarchy is normal, the solution III consists of the inverted hierarchy. Therefore, the partner of solution III, i.e. IV, is given by the intrinsic degenerate solution with inverted hierarchy. The argument $\pi/2 - \theta_{23}^{\mathrm{true}}$ in the second and the third lines arise for the similar reason.

We then summarize the one-to-one correspondence relations between the same octant and the different octant solutions:

$$
\begin{aligned}
s_{\mathrm{III}} &= \xi_\pm^{\mathrm{CP\ sign}}(s_1, \delta_1, \theta_{23}^{\mathrm{true}}), & s_{\mathrm{IV}} &= \xi_\pm^{\mathrm{CP\ sign}}(s_{\mathrm{II}}, \delta_{\mathrm{II}}, \theta_{23}^{\mathrm{true}}), \\
s_{\mathrm{V}} &= \xi_\pm^{\mathrm{CP\ oct}}(s_1, \delta_1, \theta_{23}^{\mathrm{true}}), & s_{\mathrm{VI}} &= \xi_\pm^{\mathrm{CP\ oct}}(s_{\mathrm{II}}, \delta_{\mathrm{II}}, \theta_{23}^{\mathrm{true}}), \\
s_{\mathrm{VII}} &= \xi_\pm^{\mathrm{CP\ sign\text{-}oct}}(s_1, \delta_1, \theta_{23}^{\mathrm{true}}), & s_{\mathrm{VIII}} &= \xi_\pm^{\mathrm{CP\ sign\text{-}oct}}(s_{\mathrm{II}}, \delta_{\mathrm{II}}, \theta_{23}^{\mathrm{true}}), \\
s_{\mathrm{VII}} &= \xi_\pm^{\mathrm{CP\ sign}}(s_{\mathrm{V}}, \delta_{\mathrm{V}}, \pi/2 - \theta_{23}^{\mathrm{true}}), & s_{\mathrm{VIII}} &= \xi_\pm^{\mathrm{CP\ sign}}(s_{\mathrm{VI}}, \delta_{\mathrm{VI}}, \pi/2 - \theta_{23}^{\mathrm{true}}), \\
s_{\mathrm{VII}} &= \xi_\mp^{\mathrm{CP\ oct}}(s_{\mathrm{III}}, \delta_{\mathrm{III}}, \theta_{23}^{\mathrm{true}}), & s_{\mathrm{VIII}} &= \xi_\mp^{\mathrm{CP\ oct}}(s_{\mathrm{IV}}, \delta_{\mathrm{IV}}, \theta_{23}^{\mathrm{true}}), \\
s_{\mathrm{V}} &= \xi_\mp^{\mathrm{CP\ sign\text{-}oct}}(s_{\mathrm{III}}, \delta_{\mathrm{III}}, \theta_{23}^{\mathrm{true}}), & s_{\mathrm{VI}} &= \xi_\mp^{\mathrm{CP\ sign\text{-}oct}}(s_{\mathrm{IV}}, \delta_{\mathrm{IV}}, \theta_{23}^{\mathrm{true}}).
\end{aligned}
\tag{6.65}
$$

where the functional form of $\xi_\pm^{\mathrm{CP\ sign}}$, $\xi_\pm^{\mathrm{CP\ oct}}$, and $\xi_\pm^{\mathrm{CP\ sign\text{-}oct}}$ are defined in (6.27), (6.47), and (6.62), respectively. There are the similar relationships between δ's through the function $\eta_\pm^{\mathrm{CP\ sign}}$, but we do not display them explicitly here. Fig. 1.1 shows the connection of degenerate solutions in a simple way.

It is easy to prove (6.65) by considering the original defining equations for the degeneracy. For example, it is easy to show that $\xi_\pm^{\mathrm{CP\ sign}}(s_{\mathrm{V}}, \delta_{\mathrm{V}}, \pi/2 - \theta_{23}^{\mathrm{true}}) \equiv s_{\mathrm{X}}$ and $\eta_\pm^{\mathrm{CP\ sign}}(s_{\mathrm{V}}, \delta_{\mathrm{V}}, \pi/2 - \theta_{23}^{\mathrm{true}}) \equiv \delta_{\mathrm{X}}$ are solutions of the equation

$$
\begin{aligned}
c_{23}^2 X_\pm'^2 s_{\mathrm{V}}^2 &\pm 2 s_{23} c_{23} X_\pm' Z' s_{\mathrm{V}} \cos(\delta_{\mathrm{V}} \pm \Delta_{31}) + s_{23}^2 Z'^2 \\
&= c_{23}^2 X_\mp'^2 s_{\mathrm{X}}^2 \mp 2 s_{23} c_{23} X_\mp' Z' s_{\mathrm{X}} \cos(\delta_{\mathrm{X}} \mp \Delta_{31}) + s_{23}^2 Z'^2 \\
c_{23}^2 X_\mp'^2 s_{\mathrm{V}}^2 &\pm 2 s_{23} c_{23} X_\mp' Z' s_{\mathrm{V}} \cos(\delta_{\mathrm{V}} \mp \Delta_{31}) + s_{23}^2 Z'^2 \\
&= c_{23}^2 X_\pm'^2 s_{\mathrm{X}}^2 \mp 2 s_{23} c_{23} X_\pm' Z' s_{\mathrm{X}} \cos(\delta_{\mathrm{X}} \pm \Delta_{31}) + s_{23}^2 Z'^2.
\end{aligned}
\tag{6.66}
$$

Note that left hand side of Eq.(6.66) is invariant by the replacement

$$
(s_{\mathrm{V}}, \delta_{\mathrm{V}}, s_{23}, c_{23}) \rightarrow (s_1, \delta_1, c_{23}, s_{23})
\tag{6.67}
$$

from Eq.(6.35) and (6.36). Hence, s_{X} and δ_{X} are nothing but the solutions of sign-octant degeneracy.

Though we do not present explicit formulas the same structure exists in all the degeneracy solutions in other settings, T-conjugate, Golden-Silver, and CPT-conjugate measurement to be discussed in the following sections.

6.2.2 Relation between the cases of true normal vs. true inverted mass hierarchies

Here, we note an important property of the degeneracy solutions. Namely, if we know the degeneracy solutions for the true normal mass hierarchy, then the degeneracy solutions for the true inverted mass hierarchy can be obtained from the true normal ones. We give an explicit proof of this statement.

Let us take the sign-Δm_{31}^2 degeneracy (without θ_{23} octant flip) for definiteness. For clarity, we denote the degeneracy solution for the case of true normal and true inverted mass hierarchies as $(s_{3\mathrm{N}}, \delta_{3\mathrm{N}})$ and $(s_{3\mathrm{I}}, \delta_{3\mathrm{I}})$, respectively, where the subscript "3" implies either III or IV. For a given set of the probabilities P and P^{CP}, assuming that the true mass hierarchy is normal, the true solution (s_1, δ_1) and the fake one $(s_{3\mathrm{N}}, \delta_{3\mathrm{N}})$ satisfy

$$
\begin{aligned}
(P =)\ X_+^2 s_1^2 + 2X_+ Z s_1 \cos(\delta_1 + \Delta_{31}) + Z^2 &= X_-^2 s_{3\mathrm{N}}^2 - 2X_- Z s_{3\mathrm{N}} \cos(\delta_{3\mathrm{N}} - \Delta_{31}) + Z^2, \\
\left(P^{CP} =\right)\ X_-^2 s_1^2 + 2X_- Z s_1 \cos(\delta_1 - \Delta_{31}) + Z^2 &= X_+^2 s_{3\mathrm{N}}^2 - 2X_+ Z s_{3\mathrm{N}} \cos(\delta_{3\mathrm{N}} + \Delta_{31}) + Z^2.
\end{aligned}
\tag{6.68}
$$

If the true mass hierarchy is inverted, then the degeneracy solution satisfies a different set of equations as

$$
\begin{aligned}
(P =)\ X_-^2 s_1^2 - 2X_- Z s_1 \cos(\delta_1 - \Delta_{31}) + Z^2 &= X_+^2 s_{3\mathrm{I}}^2 + 2X_+ Z s_{3\mathrm{I}} \cos(\delta_{3\mathrm{I}} + \Delta_{31}) + Z^2, \\
\left(P^{CP} =\right)\ X_+^2 s_1^2 - 2X_+ Z s_1 \cos(\delta_1 + \Delta_{31}) + Z^2 &= X_-^2 s_{3\mathrm{I}}^2 + 2X_- Z s_{3\mathrm{I}} \cos(\delta_{3\mathrm{I}} - \Delta_{31}) + Z^2.
\end{aligned}
\tag{6.69}
$$

We define $\delta_{1\mathrm{new}}$ and $\delta_{3\mathrm{Inew}}$ as $\delta_1 = \delta_{1\mathrm{new}} + \pi$ and $\delta_{3\mathrm{I}} = \delta_{3\mathrm{Inew}} + \pi$, respectively, and rewrite (6.69) by using them. It reads

$$
\begin{aligned}
X_-^2 s_1^2 - 2X_- Z s_1 \cos(\delta_{1\mathrm{new}} - \Delta_{31}) + Z^2 &= X_+^2 s_{3\mathrm{I}}^2 + 2X_+ Z s_{3\mathrm{I}} \cos(\delta_{3\mathrm{Inew}} + \Delta_{31}) + Z^2, \\
X_+^2 s_1^2 - 2X_+ Z s_1 \cos(\delta_{1\mathrm{new}} + \Delta_{31}) + Z^2 &= X_-^2 s_{3\mathrm{I}}^2 + 2X_- Z s_{3\mathrm{I}} \cos(\delta_{3\mathrm{Inew}} - \Delta_{31}) + Z^2.
\end{aligned}
\tag{6.70}
$$

Comparison between (6.68) and (6.70) tells us that if the set $(s_{3\mathrm{N}}, \delta_{3\mathrm{N}})$ is the solution to the sign-Δm_{31}^2 degeneracy equation for the true normal hierarchy, then the set $(s_{3\mathrm{I}}, \delta_{3\mathrm{Inew}})$ is the solution for the true inverted hierarchy, provided that the true value of $\delta(= \delta_1)$ is replaced by $\delta_{1\mathrm{new}}$. This is because that the oscillation probabilities (P, P^{CP}) exchange their role under the transformation $\Delta m_{31}^2 \to -\Delta m_{31}^2, \delta \to \delta + \pi$, i.e. the equations which determine the degenerate solutions is invariance under the transformation. Stated more explicitly, if we denote the sign-Δm_{31}^2 degeneracy solution for the true normal hierarchy as,

$$
s_{3\mathrm{N}} = \xi_3(s_1, \delta_1), \qquad \delta_{3\mathrm{N}} = \eta_3(s_1, \delta_1),
\tag{6.71}
$$

then, the degeneracy solution for the true inverted hierarchy is given, if expressed in terms of the true input parameters, as

$$
s_{3\mathrm{I}} = \xi_3(s_1, \delta_1 - \pi), \qquad \delta_{3\mathrm{I}} = \eta_3(s_1, \delta_1 - \pi) + \pi.
\tag{6.72}
$$

It is easy to show that this result can be extended for all type of degeneracy. In other word, the mapping functions $\xi_\pm$ and $\eta_\pm$ are related with each other as

$$
\begin{aligned}
\xi_-^{\text{CP type}}(s_1, \delta_1) &= \xi_+^{\text{CP type}}(s_1, \delta_1 - \pi), \\
\eta_-^{\text{CP type}}(s_1, \delta_1) &= \eta_+^{\text{CP type}}(s_1, \delta_1 - \pi) + \pi.
\end{aligned}
\tag{6.73}
$$

where "CP type" has the form of "CP intr", "CP sign", "CP oct", or "CP sign-oct". Thus, the sign-Δm_{31}^2 degeneracy solutions for the true inverted hierarchy are essentially determined by the solutions for the true normal hierarchy.

6.2.3 Asymptotic expansion

At the end of this section, we make comments on high-energy behavior of the degenerate solutions. It would help clarifying some features of the energy dependence of the degeneracy solutions which are discussed in the next section.

It can be easily verified that all the degeneracy solutions s_N and δ_N (N=II−VIII) in CP-conjugate measurement have finite asymptotic limit as $E \to \infty$. Then, we note an interesting property that they are invariant under the transformation $E \to -E$, because P and P^{CP} exchange their role with the transformation $\Delta_{j1} \to -\Delta_{j1}$ $(j = 2, 3)$, i.e. the degeneracy equations are invariant. It means that when we do asymptotic expansion of the degeneracy solutions as $s_N = \sum_{n=0} a_n^N (\Delta_{31})^n$ the odd terms are absent:

$$
\begin{aligned}
s_N &= a_0^N + a_2^N \Delta_{31}^2 + \mathcal{O}\left(\Delta_{31}^4\right), \\
\delta_N &= b_0^N + b_2^N \Delta_{31}^2 + \mathcal{O}\left(\Delta_{31}^4\right).
\end{aligned}
\tag{6.74}
$$

Absence of the first-order term in $1/E$ implies that onset to the high-energy asymptotic behavior of the degeneracy solutions is relatively fast, as we will confirm in the next section.

6.3 Overview of the eightfold parameter degeneracy

In this section, we try to give an overview of the intrinsic, the sign-Δm_{31}^2, and the θ_{23} octant degeneracies. In fact, the features of the degeneracy solutions are quite different for differing baselines and neutrino energies, which makes the overview in a genuine sense extremely difficult. Therefore, we restrict ourselves in this paper into a few typical settings which may be relevant for the settings of future neutrino experiments discussed in the literatures. If the readers want to examine features of the degeneracy with some alternative experimental parameters, they can do it quite easily by using the analytic solutions presented in this paper.

We also want to warn the readers that all of our comments to be made in this section are qualitative in nature. Therefore, when we say, "spectrum analysis would resolve the degeneracy" it actually means that it may be possible to resolve it *if* appropriate experimental settings are provided. Similarly, when we say "the degeneracy A is easier to lift than the degeneracy B" it actually means so *provided that* an appropriate experimental condition is prepared such that the similar sensitivities would be expected for both the solutions A and

B. Yet, we try to be based the experiences gained in some previous analyses. The readers may still wonder whether the discussion of degeneracy based on the probability makes sense because the observable in the experiments must be obtained after convolution with neutrino fluxes and cross sections. However, this is *not* the only possible attitude to take. One can, in principle, obtain the "experimental data of probability" by de-convoluting the fluxes and cross sections as shown in [75].

6.3.1 Variables used for display and baselines and neutrino energies adopted

We try to illuminate some characteristic features of the degeneracy by presenting the differences between the true solution and the fake ones. To display the difference between the solutions we define the ratio R_N as

$$R_N \equiv \frac{\sin^2 2\theta_{13}^N - \sin^2 2\theta_{13}^{\text{true}}}{\sin^2 2\theta_{13}^{\text{true}}} \tag{6.75}$$

where N = II-VIII denote the degeneracy solution labels. Similarly, we define the quantity D_N to represent the differences between the true and the clone solutions. For this purpose, there are two appropriate ways to define it, the types (1) and (2);

$$D_N^{(1)} \equiv \frac{(\delta^N - \delta^{\text{true}})}{\pi}, \qquad D_N^{(2)} \equiv \frac{\delta^N - (\pi - \delta^{\text{true}})}{\pi}. \tag{6.76}$$

We use either one of $D_N^{(1)}$ or $D_N^{(2)}$ whichever appropriate depending upon the degeneracy types.

As typical experimental settings, we use the following four cases of baselines and neutrino energies:

- SB1: $L = 300$ km, $E = 700$ MeV; A short baseline low energy ν_μ (and $\bar{\nu}_\mu$) superbeam near the first oscillation maximum

- MB1: $L = 1000$ km, $E = 2.33$ GeV; A medium baseline superbeam near the first oscillation maximum

- MB2: $L = 1000$ km, $E = 780$ MeV; A medium baseline superbeam near the second oscillation maximum

- NF: $L = 4000$ km, $E = 20$ GeV; A typical setting for neutrino factory

The first three settings, SB1, MB2, and MB1, are examined in the following three subsections (Secs. 6.3.2, 6.3.3, and 6.3.4), while the last one, NF, in Sec. 6.3.5. The energies taken for SB1, MB1, MB2 and NF settings are determined by the following considerations : To avoid the energy of perfect oscillation maximum of about 600 MeV at 300 km, where the features of the degeneracy are special, we tentatively added 100 MeV. Hence, ϵ, the deviation of Δ_{31} from $\pi/2$ is given by $\Delta_{31}(L = 300$ km $, E = 700$ MeV$) = \pi/2 - \epsilon$ from which ϵ is determined as $\epsilon = \frac{\pi}{2}\frac{1}{7} = 0.224$. For the second oscillation maximum, we have

arbitrarily chosen that $\Delta_{31}(L = 1000 \text{ km}, E) = 3(\pi/2 - \epsilon)$, that is $E = 780$ MeV. In some limited cases, the features of degeneracy solutions of the first two cases, SB1 and MB1, are so similar as can be seen in Figs. 6.12 and 6.13. Comparison between MB1 and MB2 settings, former (latter) being around the first (second) oscillation maximum, would be interesting to know physics behind the potential of the two-detector setting [78] and/or the BNL-type wide band beam approach [81].

The key to resolve the degeneracy is to utilize spectrum informations. Therefore, we also present the energy dependence of the difference between the true and the degeneracy solutions. A point of interest is how the energy dependence differs among the three different types of the degeneracies.

We note that in all the figures presented in this section we take the normal mass hierarchy as the input true solution. If one wants to have the corresponding informations for the inverted mass hierarchy, one can do it just by changing the ordinate label of the figures as $\delta^{\text{true}} - \pi$ not δ^{true}. This is discussed in detail in Sec. 6.2.2.

We use the following values for the mixing parameters as summarized below: $\Delta m_{21}^2 = 7.9 \times 10^{-5}$ eV^2, $\sin^2 \theta_{12} = 0.31$, and $\Delta m_{31}^2 = 2.5 \times 10^{-3}$ eV^2. The matter density is taken as $\rho = 2.8$g/cm^3 for SB1, MB1, and MB2 settings, and $\rho = 3.6$g/cm^3 for NF setting.

Method for presentation

A color variation is used to clearly represent the ratio R_{II} and $D_{\text{II}}^{(2)}$ in a visual way, which will be used later also to all of R_{N} and $D_{\text{N}}^{(i)}$. From blue to red R_{II} and $D_{\text{II}}^{(2)}$ vary from -1 to $+1$. The only exception to this rule is R_{N} at color graduation of the deepest red; It contains the region with R_{N} greater than 1. Notice that there is no region of $R_{\text{N}} < -1$ by definition in (6.75). We should note that in the case of $D_{\text{N}}^{(i)}$, unlike R_{N}, the deep blue region smoothly continues to the deep red because of the periodicity in δ. 20 color graduation are used to draw R_{N} and $D_{\text{N}}^{(i)}$ so that a single color graduation spans 5% of the entire region.

6.3.2   Intrinsic degeneracy in the true θ_{23} octant

In Figs. 6.12 and 6.13, we present R_{II}, the normalized difference of $\sin^2 2\theta_{13}$, and $D_{\text{II}}^{(2)}$, a difference of δ/π defined in (6.76), respectively, between the true and the intrinsic degeneracy solutions for the three typical cases of energies and baselines, SB1, MB1, and MB2.

One can easily realize that the feature of SB1 (left panel) and MB1 (middle panel) setting is so similar. One of the most notable features in Fig. 6.12 is a clear difference between SB1 (or MB1) and MB2 (right panel) settings. In large θ_{13} region in SB1 setting, $\sin^2 2\theta_{13} \gtrsim 10^{-2}$, R_{II} is small. At small θ_{13} in SB1 setting and at large θ_{13} in MB2 setting, R_{II} is large and positive (negative) at $\delta \sim 0$ (π). In small θ_{13} region in MB2 setting, $\sin^2 2\theta_{13} \lesssim 10^{-2}$, R_{II} is large and positive independent of δ.[1] Let us understand these features.

We start from the above first feature. It can be understood by the analytic solution (6.15). If θ_{13} is relatively large, $s_{13} \gg \Delta m_{21}^2/\Delta m_{31}^2$, s_1 is the dominant term in s_{II} in (6.15),

---

[1]At extremely small θ_{13}, the left plot in Fig. 6.12 for SB1 almost looks like the right plot for MB2, but with scale of $\sin^2 2\theta_{13}$ two orders of magnitude smaller than that of the right panel in Fig. 6.12.
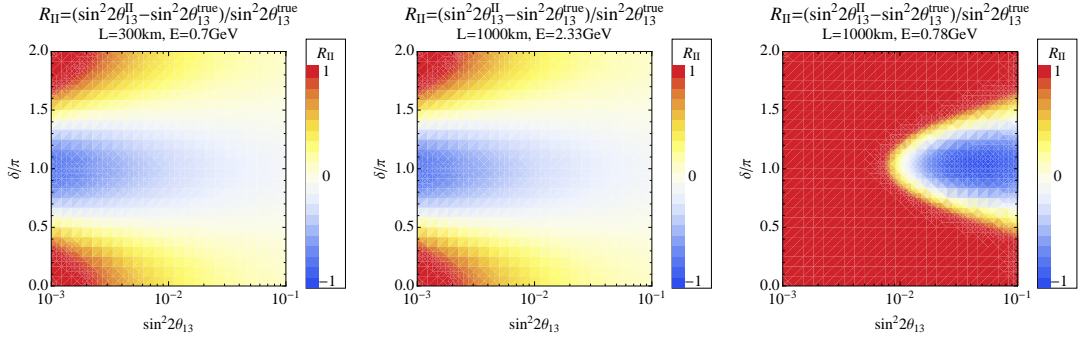
Figure 6.12: The ratio $R_{\mathrm{II}} = [\sin^2 2\theta_{13}^{\mathrm{N}} - \sin^2 2\theta_{13}^{\mathrm{true}}] / \sin^2 2\theta_{13}^{\mathrm{true}}$ defined in (6.75) is presented in $\sin^2 2\theta_{13}^{\mathrm{true}} - \delta^{\mathrm{true}}/\pi$ space for the three typical cases of energies and baselines, SB1, MB1, and MB2, defined in Sec. 6.3.1.
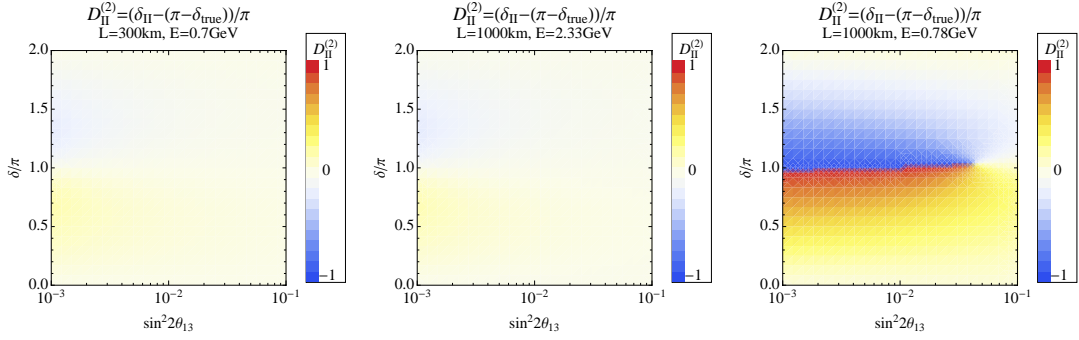
Figure 6.13: The normalized difference $D_{\mathrm{II}}^{(2)} \equiv [\delta^{\mathrm{II}} - (\pi - \delta^{\mathrm{true}})]/\pi$, defined in (6.76) is presented in $\sin^2 2\theta_{13}^{\mathrm{true}} - \delta^{\mathrm{true}}/\pi$ space for the three typical settings SB1, MB1, and MB2 defined in Sec. 6.3.1.
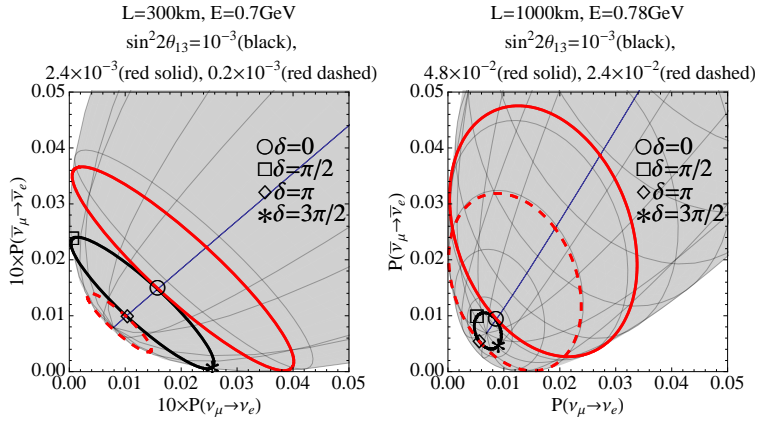
Figure 6.14: Bi-probability plot for settings of SB1 (left panel) and MB2 (right panel). In both plots the true value of θ_{13} is taken to be $\sin^2 2\theta_{13} = 10^{-3}$. The ellipses of the intrinsic degeneracy solutions are depicted by the red solid and red dashed lines.

62

and $R_{\mathrm{II}} \sim O\left(s_1^{-1}\Delta m_{21}^2/\Delta m_{31}^2\right)$. Therefore, R_{II} is small at large θ_{13} in SB1 setting. Now, the behavior of R_{II} at small θ_{13} can be easily understood by looking into the bi-probability plot, the left panel in Fig. 6.14. The degeneracy ellipse which shares the point around $\delta = 0$ ($\delta = \pi$) of the true ellipse is the dashed (solid) one with considerably larger (smaller) θ_{13}. The similar consideration explains the feature of R_{II} at large θ_{13} in MB2 setting. The remaining feature that needs explanation is the large positive R_{II} at small θ_{13} in MB2 setting. At such small θ_{13} as $\sin^2 2\theta_{13} \sim 10^{-3}$ and the baseline $L = 1000$ km, the oscillation probability is dominated by the solar term Z^2. Since it is independent of δ the probability ellipse shrinks to a small "circle", as can be seen in the right panel in Fig. 6.14. Then, the degeneracy solution ellipses are inevitably large as indicated by the red solid and dashed lines, resulting degenerate solutions much larger than the true s_{13}.

We observe for $D_{\mathrm{II}}^{(2)}$ plotted in Fig. 6.13 that in SB1 (and MB1) setting $D_{\mathrm{II}}^{(2)}$ is small in the entire region of $\sin^2 2\theta_{13} - \delta/\pi$ space covered.[2] It means that the approximate formula $\delta^{\mathrm{II}} \simeq \pi - \delta^{\mathrm{true}}$ works well [55]. It is a nice feature of measurement of SB1 setting because CP violation is unlikely to be confused with CP conservation. Whereas for MB2 setting $D_{\mathrm{II}}^{(2)}$ is small only in a limited region $-0.2 \lesssim \delta/\pi \lesssim 0.2$, and in a small strip around $\delta \simeq 0$ at large θ_{13}. The deviation from the approximation $\delta^{\mathrm{II}} \simeq \pi - \delta^{\mathrm{true}}$ is significant in the second and the third quadrants of δ, in particular in region $\sin^2 2\theta_{13} \lesssim$ a few $\times 10^{-2}$ in MB2 setting. It is possible to understand this behavior of $D_{\mathrm{II}}^{(2)}$ qualitatively at very small θ_{13}, $\sin^2 2\theta_{13} \sim 10^{-3}$ by using the bi-probability plot for MB2 setting (right panel in Fig. 6.14). For the true value of $\delta^{\mathrm{true}} \simeq 0$ the degeneracy ellipse is depicted by the solid line and $\delta_{\mathrm{II}} \simeq \pi$, which implies $D_{\mathrm{II}}^{(2)} \ll 1$. On the other hand, for $\delta^{\mathrm{true}} \simeq \pi$ the degeneracy ellipse depicted by the dashed line touches to the true ellipse also at around $\delta \simeq \pi$, hence $D_{\mathrm{II}}^{(2)}$ is of order unity. Notice again that the deep blue region smoothly continues to the deep red because of the periodicity in δ.

Now, let us show the similar plots with a different energy for the three settings. Fig. 6.15 and 6.16 show R_{II} and $D_{\mathrm{II}}^{(2)}$ respectively at, $E = 530$ MeV, 1.8 GeV, and 600 MeV for SB1, MB1, and MB2 setting respectively, the energy bit lower than the oscillation maximum. One can realize that they have very similar feature with Fig. 6.12 and 6.13 but with replacement $\delta \to \pi - \delta$. This feature can be understood by Fig. 6.15. Choice of energies higher or lower than the oscillation maximum alters the relative positions of $\delta = 0$ and $\delta = \pi$ in the bi-probability ellipse, and hence the behavior follows as $\delta \to \pi - \delta$.

The existence of difference of intrinsic solution between different energy setting tells us that intrinsic degeneracy may be resolved by spectrum analysis. Therefore, let us see the energy dependence of it. We present in Fig. 6.18 the energy dependence of $\sin^2 2\theta_{13}^{\mathrm{II}}$ for SB1 (left panel), MB1 (middle panel), and MB2 (right panel) settings, assuming the true value of $\sin^2 2\theta_{13} = 0.05$. It may be regarded as a typical value for relatively large θ_{13} to which we will have an access by the ongoing experiments. Notice that here the color labels are not monotonic from $\delta = 0$ to 2π. Similarly, in Fig. 6.19 the energy dependence of $D_{\mathrm{II}}^{(2)}$ is plotted for the same settings, SB1, MB1, and MB2, with the same true value of θ_{13}. Again, SB1 and MB1 setting have very similar feature in the energy region we plot.

---

[2]Hereafter, when we talk about $\sin^2 2\theta_{13}$ and δ such as $\sin^2 2\theta_{13} - \delta/\pi$ space, it actually means the $\sin^2 2\theta_{13}^{\mathrm{true}}$ and δ^{true}, respectively. We use the simpler notation to avoid cumbersome superscript "true" as much as possible.
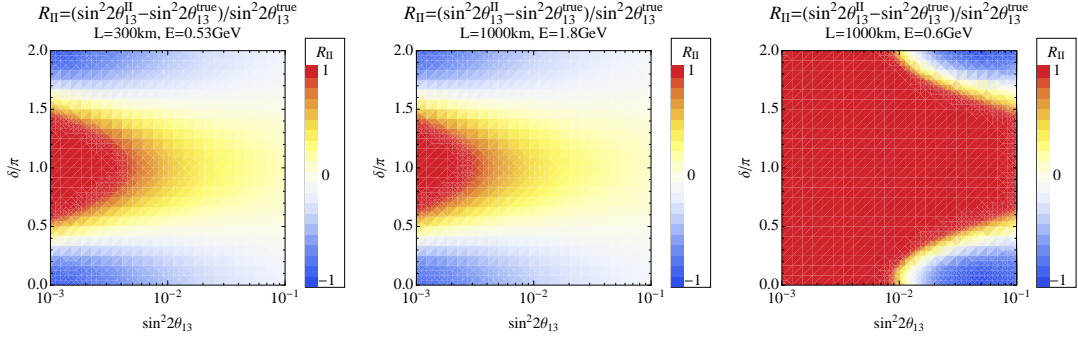
Figure 6.15: R_{II} plots similar to Fig. 6.12 but with different energy. $E = 530$ MeV, 1.8 GeV, and 600 MeV for left, middle, and right panel respectively.
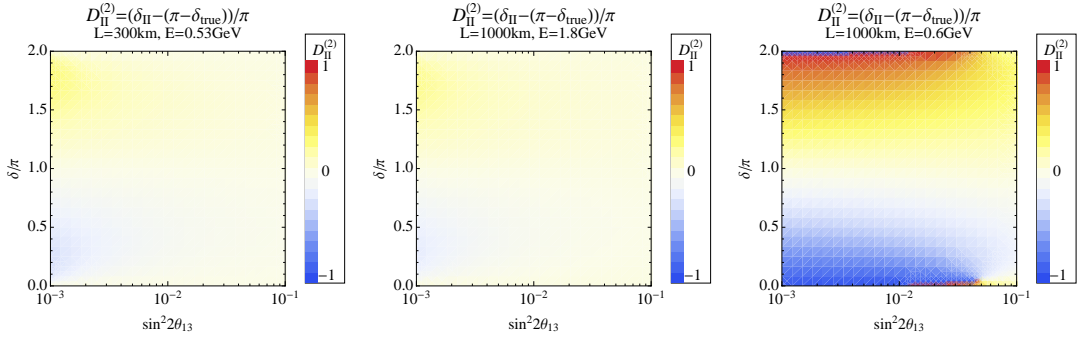
Figure 6.16: $D_{\mathrm{II}}^{(2)}$ plots similar to Fig. 6.13 but with different energy as same as Fig. 6.15.
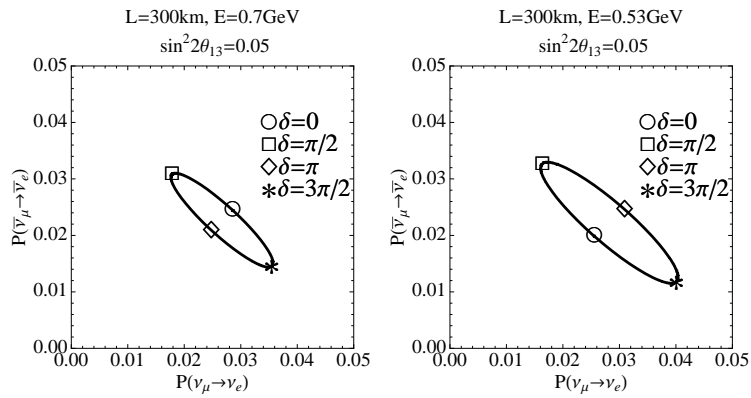
Figure 6.17: Bi-probability plot for settings of E=700 MeV (left panel) and E=530 MeV (right panel). In both plots the true value of θ_{13} is taken to be $\sin^2 2\theta_{13} = 0.05$.
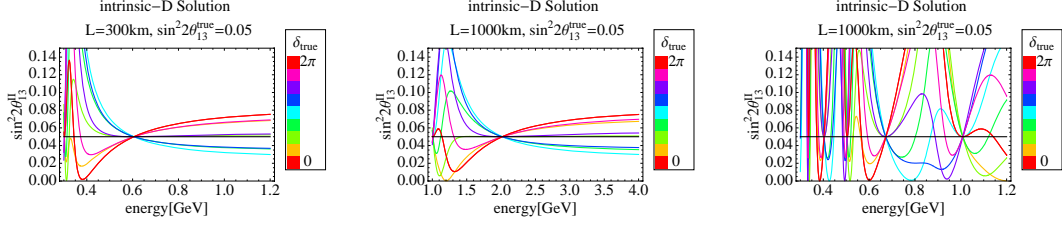
Figure 6.18: The energy dependence of $\sin^2 2\theta_{13}^{\mathrm{II}}$ is plotted for the two typical settings SB1 (left panel), MB1 (center panel), and MB2 (right panel) defined in Sec. 6.3.1. The true value of θ_{13} is taken as $\sin^2 2\theta_{13} = 0.05$, which is indicated by the horizontal solid line in the figure.
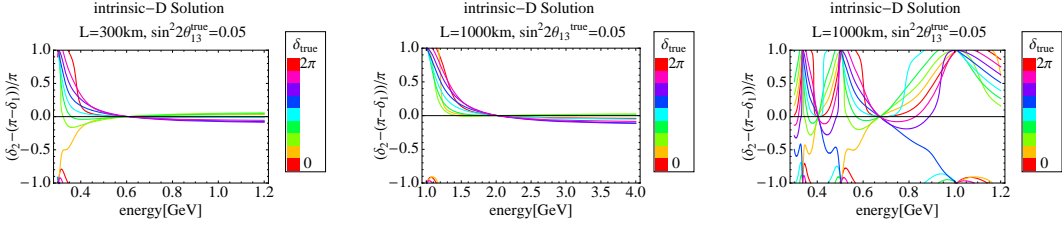
Figure 6.19: The energy dependence of the ratio $D_{\mathrm{II}}^{(2)}$ defined in (6.76) is plotted for the two typical settings SB1 (left panel), MB1 (center panel) and MB2 (right panel) defined in Sec. 6.3.1. The true value of θ_{13} is taken as $\sin^2 2\theta_{13} = 0.05$.

Clearly, there exist a significant energy dependence of $\sin^2 2\theta_{13}^{\mathrm{II}}$ even for SB1 setting. One can see that they vary by a factor of $2-4$ ($30\% - 40\%$), or more at low (high) energies depending upon δ in region of $E = 0.4 - 1.2$ GeV for $L = 300$ km. It must be contrasted to almost flat curves of energy dependence given in the following subsections, Figs. 6.21 (Sec. 6.3.3) and 6.26 (Sec. 6.3.4) for the sign-Δm_{31}^2 and the octant degeneracies, respectively. Then, the spectrum analysis must be powerful in resolving the intrinsic degeneracy. It has been seen to be the case in the analysis of T2K II experiment [43] done in [79]. For $D_{\mathrm{II}}^{(2)}$ the energy dependence is significant only at low energies, below the first oscillation maximum, where usually the signal-to-background ratio is not helpful. But it does not means that intrinsic degenerate solution δ_{II} remains after the spectrum analysis, because if spectrum information resolve the solution s_{II} its pair parameter, δ_{II}, is forbidden.

For MB2 setting, which is at around the second oscillation maximum, the energy dependence is far more pronounced and depends on δ. As we can see in the R_{II} plot, intrinsic degenerate solutions at SB1 and MB2 setting are very different in broad region. Therefore, combination of MB2 with SB1 settings is expected as an ideal machinery for resolving the degeneracy. This was observed in [79, 80] which utilizes the informations at the second oscillation maximum by a Korean detector.

6.3.3 Sign-Δm_{31}^2 degeneracy in the true θ_{23} octant

We now turn to the sign-Δm_{31}^2 degeneracy which exists in the same θ_{23} octant as the true one. Since there are two solutions, $(s_{\mathrm{III}}, \delta_{\mathrm{III}})$ and $(s_{\mathrm{IV}}, \delta_{\mathrm{IV}})$, we present them in the same figures. In Fig. 6.20, R_{III} and R_{IV} defined in (6.75) are plotted in $\sin^2 2\theta_{13} - \delta/\pi$ space. White region is the region of no degenerate solution as discussed in Sec. 6.1.3. We mention that MB1 setting is different from SB1 setting unlike the case of intrinsic degeneracy, in particular in small θ_{13} region. Nevertheless, the difference is not so significant at large θ_{13} $\sin^2 2\theta_{13} \gtrsim 10^{-2}$ apart from the change in the no-solution region.

By comparing Fig. 6.20 with Fig. 6.12, it is evident that the difference of $\sin^2 2\theta_{13}$ between the true solution s_1 and s_{III} is much smaller than the case of intrinsic degeneracy solutions for SB1 and MB1 settings.
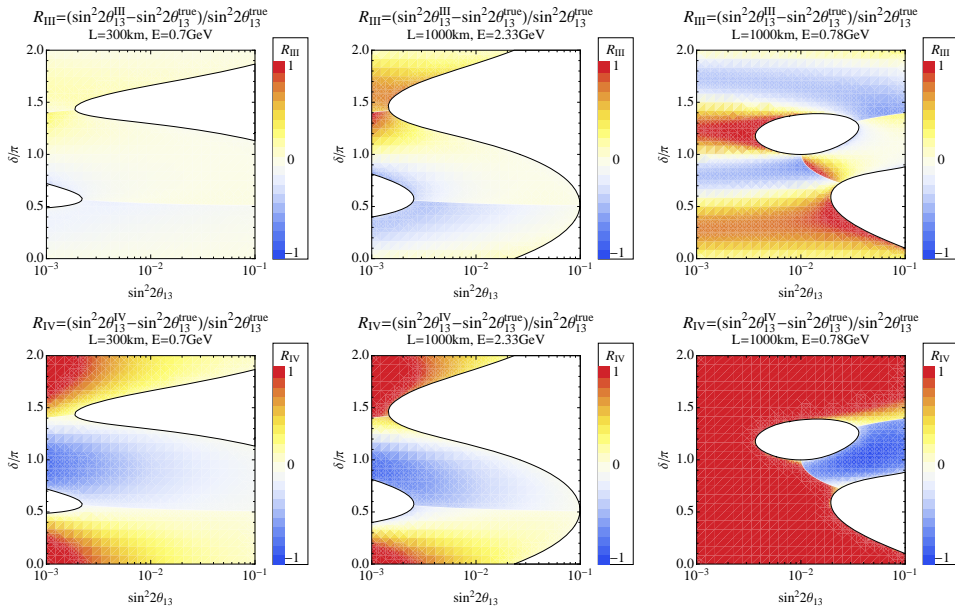
Figure 6.20: The ratios $R_{\mathrm{III}} = [\sin^2 2\theta_{13}^{\mathrm{III}} - \sin^2 2\theta_{13}^{\mathrm{true}}]/\sin^2 2\theta_{13}^{\mathrm{true}}$ (upper two panels) and R_{IV} (lower two panels) defined in (6.75) in $\sin^2 2\theta_{13} - \delta/\pi$ space is presented for the three typical settings SB1 (left panel), MB1 (middle panel), and MB2 (right panel) defined in Sec. 6.3.1. The regions of white color denote the regions of no sign-degeneracy solution.

One can realize that the energy dependence of $\sin^2 2\theta_{13}^{\mathrm{III}}$ is much milder than the case of solution $(s_{\mathrm{II}}, \delta_{\mathrm{II}})$ of the intrinsic degeneracy, as one can clearly see by comparing Fig. 6.21 with Fig. 6.18. These features make resolution of the sign-Δm_{31}^2 degeneracy much more difficult compared to the intrinsic degeneracy in these settings.

The difference between energy dependences of the intrinsic and the sign-Δm_{31}^2 degeneracies in SB1 and MB1 settings can be easily understood at least qualitatively. As we learned in Sec. 6.2.3 reach to high-energy asymptotic behavior is relatively fast by lacking $\sim 1/E$ terms. This feature can be seen in most of the plots of energy dependence of the degeneracy solutions for SB1 and MB1 settings. Notice, however, that the asymptotic energy
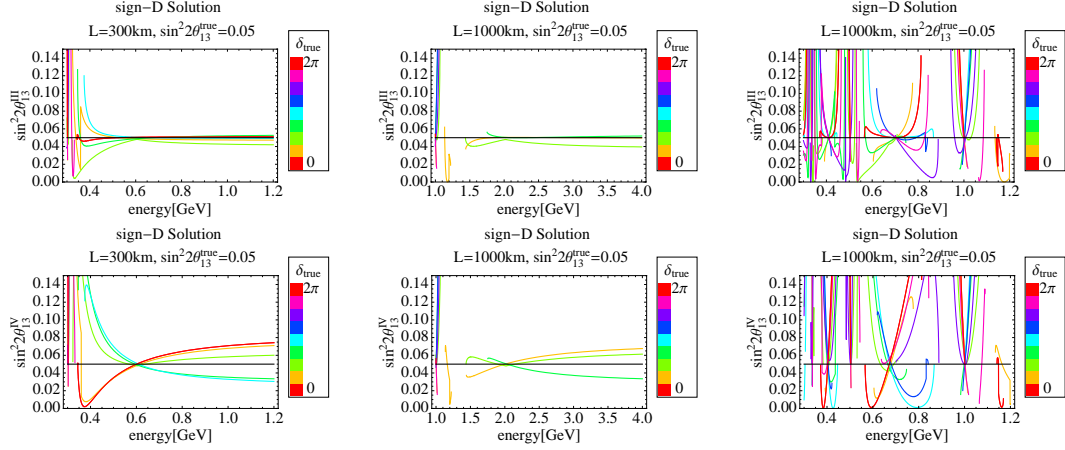
Figure 6.21: The energy dependence of $\sin^2 2\theta_{13}^{\mathrm{III}}$ (upper two panels) and $\sin^2 2\theta_{13}^{\mathrm{IV}}$ (lower two panels) are plotted for the three typical settings SB1 (left panel), MB1 (middle panel), and MB2 (right panel) defined in Sec. 6.3.1. The true value of θ_{13} is taken as $\sin^2 2\theta_{13} = 0.05$, which is indicated by the horizontal solid line in the figure.

can be reached at much higher energies for MB2 setting. The difference between $\sin^2 2\theta_{13}^{\mathrm{III}}$ and $\sin^2 2\theta_{13}^{\mathrm{II}}$ is that the former is constrained to be small at low energies, as one can show by the formulas based on the matter perturbation theory given in Section 6.1.3. The first order correction term, from which the energy dependence comes in is small, of the order of $A/\Delta_{31} \simeq 0.06 - 0.07(0.2)$ for SB1 and MB2 (MB1) settings. Whereas for $\sin^2 2\theta_{13}^{\mathrm{II}}$ there is no small parameter which forces it small. The mild energy dependence and the pinning to a small value makes $\sin^2 2\theta_{13}^{\mathrm{III}}$ small in the entire region of energy.

Here are comments on the solution $(s_{\mathrm{IV}}, \delta_{\mathrm{IV}})$: R_{IV} essentially looks like R_{II} apart from the presence of no-solution regions. Given smallness of R_{III}, R_{IV} must looks like R_{II} because they are the intrinsic degeneracy pairs. It is also true that the energy dependence of $\sin^2 2\theta_{13}^{\mathrm{IV}}$ is very similar to the behavior of $\sin^2 2\theta_{13}^{\mathrm{II}}$. Therefore, lifting degeneracy between $\theta_{13}^{\mathrm{IV}}$ and $\theta_{13}^{\mathrm{III}}$ can be done with spectrum analysis via a similar manner as in the case of intrinsic degeneracy. If powerful enough the spectrum informations would solve both the degeneracy between the true solution and $\theta_{13}^{\mathrm{II}}$, and the one between $\theta_{13}^{\mathrm{IV}}$ and $\theta_{13}^{\mathrm{III}}$ at the same time.

Next, we discuss $D_{\mathrm{III}}^{(2)}$ and $D_{\mathrm{IV}}^{(1)}$ which are presented in the upper and lower three panels, respectively, in Fig. 6.22. We note that they are small in SB1 setting, leaving the sign-Δm_{31}^2 degeneracy intact in this short baseline setting. Notice, however, that it is not all bad, because the smallness of $D_{\mathrm{III}}^{(2)}$ implies that no severe confusion takes place between CP violation and CP conservation. Now, the difference between SB1 and MB1 settings further develops in particular in large θ_{13} region. The clear distinction between SB1 and MB1 settings is also prominent in the energy dependence presented in Fig. 6.23. Of course, it is basically due to larger matter effect in MB1 setting. It is interesting to observe that the difference shows up first in δ, but not quite for θ_{13} at large θ_{13}.

In the SB1 and MB1 settings, as can be seen in Fig. 6.22, $D_{\mathrm{III}}^{(2)}$ and $D_{\mathrm{IV}}^{(1)}$ are largest in region of the largest possible θ_{13} for which the sign-Δm_{31}^2 degeneracy solution exist. In
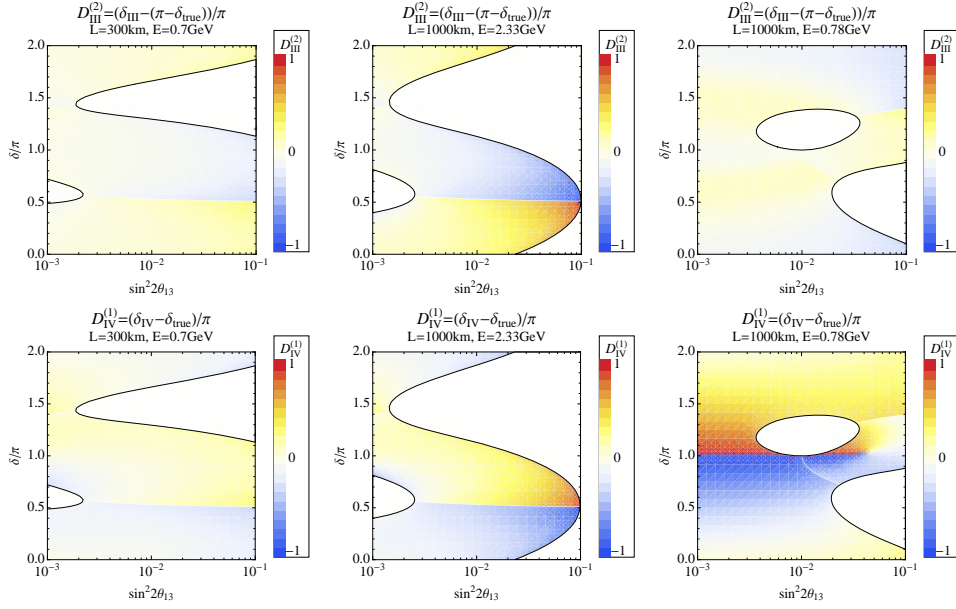
Figure 6.22: $D_{\mathrm{III}}^{(2)} \equiv [\delta^{\mathrm{III}} - (\pi - \delta^{\mathrm{true}})]/\pi$ (upper two panels) and $D_{\mathrm{IV}}^{(1)} \equiv (\delta^{\mathrm{IV}} - \delta^{\mathrm{true}})/\pi$ (lower two panels) defined in (6.76) is presented in $\sin^2 2\theta_{13} - \delta/\pi$ space for the three typical settings SB1 (left panel), MB1 (middle panel), and MB2 (right panel) defined in Sec. 6.3.1. The regions of white color denote the regions of no sign-degeneracy solution.
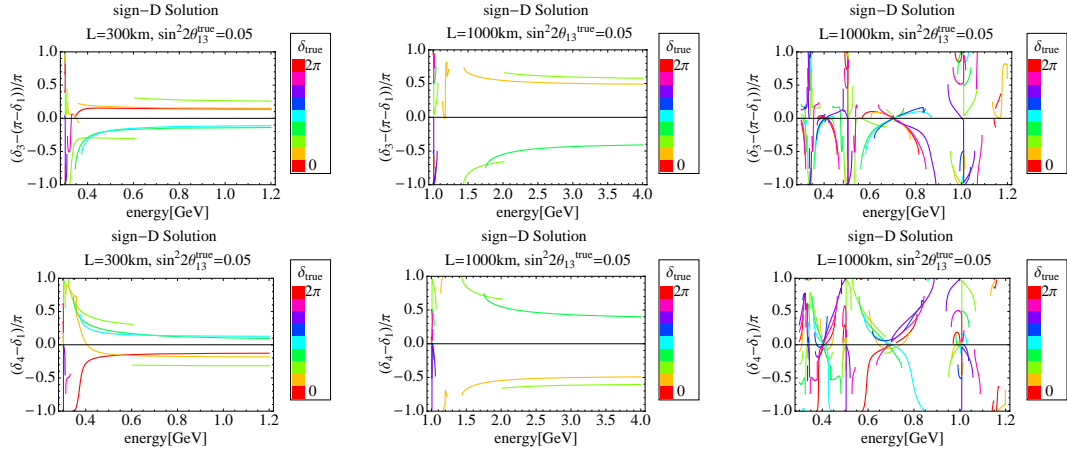
Figure 6.23: The energy dependence of the ratios $D_{\mathrm{III}}^{(2)}$ (upper two panels) and $D_{\mathrm{IV}}^{(1)}$ (lower two panels) defined in (6.76) are plotted for the three typical settings SB1 (left panel), MB1 (middle panel), and MB2 (right panel) defined in Sec. 6.3.1. The true value of θ_{13} is taken as $\sin^2 2\theta_{13} = 0.05$.

this region $\delta \sim \pi/2$. On the other hand, R_{III} and R_{IV} are small in the region as is seen in Fig. 6.20. It is easy to understand these features. At around the largest value of θ_{13} which allows the sign-Δm_{31}^2 degeneracy the two ellipses, the ones with normal and inverted mass hierarchies, barely overlap with each other. This is shown in Fig. 6.24. The general feature
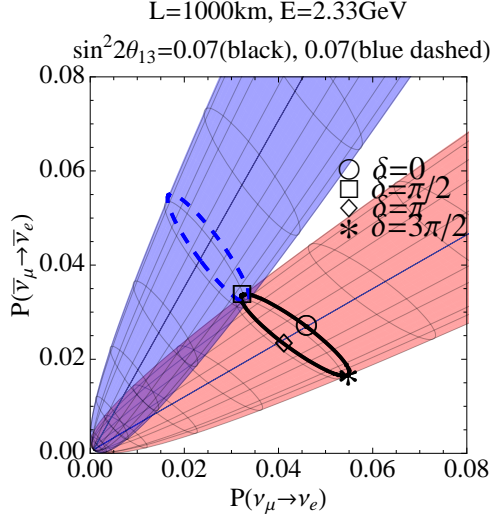
Figure 6.24: The bi-probability plot with the true value of θ_{13} as $\sin^2 2\theta_{13} = 0.07$ and normal (inverted) hierarchy for black solid (blue dashed) line. Red (blue) shaded area show the region spanned the ellipse with normal (inverted) hierarchy.

of the bi-probability plot [56] tells us that in the overlap regions of the two ellipses the point of $\delta \sim \pi/2$ in the positive Δm_{31}^2 ellipse is close to point of $\delta \sim 3\pi/2$ of the negative Δm_{31}^2 ellipse. Therefore, $D_{\mathrm{III}}^{(2)} \simeq 1$ and $D_{\mathrm{IV}}^{(1)} \simeq 1$ hold, explaining the above features. Because the center of the two ellipses are located at almost the same distances from the origin (which is equal to $s_{23}^2 \sin^2 2\theta_{13}$), $s_{\mathrm{III}} \simeq s_{\mathrm{IV}} \simeq s_1$.

We want to note that the energy dependences of $D_{\mathrm{III}}^{(2)}$ and $D_{\mathrm{IV}}^{(1)}$ are quite mild in energy region above the first oscillation maximum for SB1 and MB1 settings. Considering the almost no energy dependence of $\sin^2 2\theta_{13}^{\mathrm{III}} - \sin^2 2\theta_{13}^{\mathrm{true}}$ as given in Fig. 6.21, and noting that spectrum analysis is highly challenging at low energies, it would be difficult to resolve the sign-Δm_{31}^2 degeneracy by a single detector setting of either SB1 or MB1.

We notice that the difference between SB1-MB1 and MB2 settings is always evident as can be seen in Figs. 6.20, 6.21, 6.22 and 6.23. Therefore, MB2 setting alone may have chance to resolve the sign-Δm_{31}^2 degeneracy [89, 90]. Or, if the informations gained at around the second oscillation maximum can somehow be combined it would greatly help resolving the sign-Δm_{31}^2 degeneracy [79, 80, 81, 91]. It may be expected even from our formulas obtained for a "mono-energetic neutrino beam" because the parameter regions with degeneracy solutions in SB1 and MB2 settings tend to "repel" (avoid to overlap) with each other at large θ_{13} in Fig. 6.20, though not completely.

6.3.4 Intrinsic and sign-Δm_{31}^2 degeneracies in the false θ_{23} octant

Now, we turn to the θ_{23} octant degeneracy with solutions which lives in the different θ_{23} octant from the true solution. Having the overview at hand, we present the intrinsic and the sign-Δm_{31}^2 degeneracy solutions at the same time. Presented in Fig. 6.25 in $\sin^2 2\theta_{13} - \delta/\pi$ space are the ratios $R_{\rm V} = \left(\sin^2 2\theta_{13}^{\rm V} - \sin^2 2\theta_{13}^{\rm true}\right)/\sin^2 2\theta_{13}^{\rm true}$ (top three panels), $R_{\rm VI}$ (next to top panels), $R_{\rm VII}$ (next next to top panels), and $R_{\rm VIII}$ (bottom three panels) defined in (6.75) for three typical cases of energies and baselines, SB1 (left panels), MB1 (middle panels), and MB2 (right panels) defined in Sec. 6.3.1. In Fig. 6.26, from the top row to the bottom, the energy dependences of degeneracy solutions of $\sin^2 2\theta_{13}^{\rm N}$ are presented for the same set of solutions N=V−VIII.

One of the most notable features in Fig. 6.25 is again quite distinct behaviors in the MB2 setting. In general, $R_{\rm N}$ are large (apart from the strips where $R_{\rm N}$ switches its sign) with notable exceptions of $R_{\rm V}$ for SB1 and MB1 settings, and $R_{\rm VII}$ for SB1 setting. It is also notable that behavior of $R_{\rm VI}$ and $R_{\rm VIII}$ is reminiscent of the one of $R_{\rm II}$ in Fig. 6.13 in SB1 and MB1 settings in small θ_{13} region, except for the presence of no-solution region. Considering the small values of $R_{\rm V}$ and $R_{\rm VII}$ (except for $R_{\rm VII}$ for MB1), it is quite natural to see the behavior given the fact that they are the intrinsic degeneracy partners. The feature that $R_{\rm VI}$ and $R_{\rm VIII}$ trace the behavior of their intrinsic degeneracy partners also applies to MB2 setting. The behavior of $R_{\rm V}$ and $R_{\rm VII}$ ($R_{\rm VI}$ and $R_{\rm VIII}$) is somewhat similar, apart from the presence of no-solution region, to that of $R_{\rm II}$ for SB1 (MB2) setting. It may be understood by the similar consideration using the bi-probability plot. Therefore, we concentrate below on SB1 and MB1 settings.

As mentioned above $R_{\rm V}$ for SB1 and MB1 settings, and $R_{\rm VII}$ for SB1 setting are small in region $\sin^2 2\theta_{13} \gtrsim 10^{-2}$. The region of θ_{13}, however, is nothing but a good target for superbeam experiments, and it will be a challenge for them to lift the degeneracy solutions. Here, we try to understand this feature, but in a wider perspective which includes the energy dependence of $\sin^2 2\theta_{13}^{\rm V}$ and $\sin^2 2\theta_{13}^{\rm VII}$ for SB1 and MB1 settings. In Fig. 6.26, we observe that the difference between $\sin^2 2\theta_{13}^{\rm V}$ (or, $\sin^2 2\theta_{13}^{\rm VII}$) and $\sin^2 2\theta_{13}^{\rm true}$ is nonzero but energy independent in a wide region except for at very low energies, a somewhat unexpected behavior to see.

Now, we point out that the behaviors mentioned above can be understood by formulating the θ_{23} perturbation theory, as done in Section 6.1.4. Namely, one can derive the perturbative expression of $\sin^2 2\theta_{13}^{\rm N}$ and other quantities by assuming that deviation of θ_{23} from $\pi/4$ is small, $\theta_{23} - \pi/4 \equiv \epsilon_{\rm oct} \ll 1$. One can expect that the expansion by $\epsilon_{\rm oct}$ is indeed a good approximation because e.g., $\epsilon_{\rm oct} = 0.05$ for $\theta_{23} = 42°$. Then, we obtain

$$\sin^2 2\theta_{13}^{\rm V} - \sin^2 2\theta_{13}^{\rm true} = 4\epsilon_{\rm oct} \sin^2 2\theta_{13}^{\rm true} \tag{6.77}$$

for which we have used the fact that the last term in (6.50) is negligibly small as far as we remain in a region $\sin^2 2\theta_{13}^{\rm true} \gg Z^2$. In fact, we confirmed that the correction term becomes non-negligible at small θ_{13} around $\sin 2\theta_{13}^{\rm true} = 10^{-3}$. Certainly, the condition is fulfilled for the settings SB1 and MB1. The similar equation holds for $\theta_{13}^{\rm VII}$ but with replacement of $\theta_{13}^{\rm true}$ to $\theta_{13}^{\rm III}$ because their relation as the intrinsic degeneracy partner. Therefore, $R_{\rm V}$ and $R_{\rm VII}$ are small and the difference in (6.77) is approximately energy independent. One may ask why the feature does not exist in MB2 setting with small θ_{13}. As mentioned before, the

solar term is dominant in this region. Therefore, if $\epsilon_{\text{oct}} Z$ is comparable to s_1 the difference $s_{\text{V}} - s_1$ is no more small.

Another notable point is that no degeneracy solution region is not additive, as can be seen by comparing Figs. 6.20 and 6.25. That is, the region of no degeneracy solution with Δm^2_{31}-sign and θ_{23} octant flips (VII and VIII) is not the union of no-solution regions of the sign-Δm^2_{31} (III) and the θ_{23} octant (V) degeneracies. It is simply because the degeneracy solution with both sign and octant flips can exist even in a region of θ_{13} and δ where e.g., the octant degeneracy solution does not exist.

In Fig. 6.27, from the top to the bottom, the normalized differences between the true and fake solutions of phases, $D_{\text{V}}^{(1)}$, $D_{\text{VI}}^{(2)}$, $D_{\text{VII}}^{(2)}$, and $D_{\text{VIII}}^{(1)}$ defined in (6.76) are presented for SB1 (left panels), MB1 (middle panels), MB2 (right panels) settings. In Fig. 6.28, the energy dependences of $D_{\text{V}}^{(1)}$, $D_{\text{VI}}^{(2)}$, $D_{\text{VII}}^{(2)}$, and $D_{\text{VIII}}^{(1)}$ are plotted in the same rows corresponding to Fig. 6.27. One notices that for SB1 setting $D_{\text{N}}^{(i)}$ (i either 1 or 2) is small in most of the regions of true values of δ for all the solutions V-VIII. For MB1 setting the same statement applies for the solutions V and VI. A notable feature is that $D_{\text{V}}^{(1)}$ (and $D_{\text{VII}}^{(2)}$) is small in MB2 setting. It can also be understood from the θ_{23} perturbative formula for δ given in Section 6.1.4; The difference between δ_1 and δ_{V} is always suppressed by ϵ_{oct}.

As discussed above the energy dependence is very mild for most of the solutions V−VIII, except for at low energies, $E \lesssim 0.4$ GeV, in SB1 and MB1 settings. Therefore, it may be extremely challenging for experiments with the settings to lift the degeneracy. Because of the likely difficulty in resolving the θ_{23} octant degeneracy several methods have been proposed; the reactor-accelerator combined method [82, 96], the various ways to detect solar Δm^2_{21} scale oscillations, using atmospheric [92, 93, 94, 95] or accelerator neutrinos [89, 90, 80], or both combined [98, 100]. The silver channel could be of help [99]. As in the previous cases the behavior of degeneracy solutions are far more violent in MB2 setting. It by itself might mean the great sensitivity to resolve the degeneracy. Or, it is a natural way of thinking to combine it with the measurement at the first oscillation maximum.

We give here a brief summary of the characteristic features of the degeneracy in superbeams, SB1, MB1, and MB2 settings.

- A prominent difference between the true and the clone solutions exists in R_{N} defined in (6.75) as the normalized difference of $\sin^2 2\theta_{13}$, in the intrinsic degeneracy, while for the sign-Δm^2_{31} degeneracy it is in the phase difference $D_{\text{N}}^{(i)}$.

- The solutions III for the sign-Δm^2_{31} degeneracy appears to be difficult to resolve for SB1 setting even if spectrum information is available, because energy dependences are so weak for both R_{III} and $D_{\text{III}}^{(2)}$. The similar difficulty exists for MB1 if θ_{13} is large, $\sin^2 2\theta_{13} \gtrsim 10^{-2}$. For the same reason, the solutions V and VII of the θ_{23} octant degeneracy is difficult to lift.

- The short baseline SB1 option is unique among the three superbeam settings in the sense that it by itself may not be able to lift the sign-Δm^2_{31} and the θ_{23} octant degeneracies, but can provide a clean discovery of CP violation without confusion with CP conservation. This is in accord with the basic motivation for low energy superbeam [72].
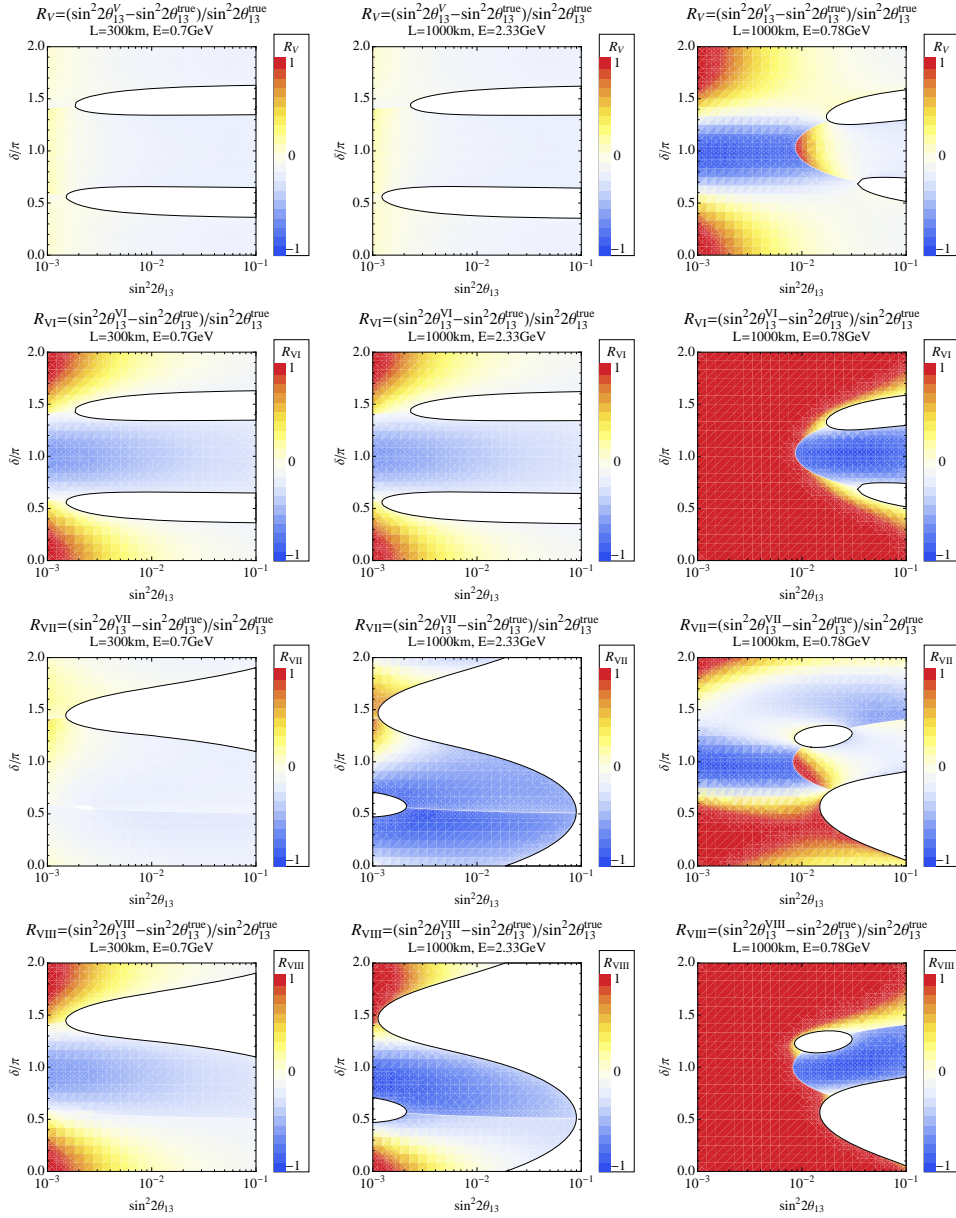
Figure 6.25: Plotted are the ratios $R_{\mathrm{V}} = [\sin^2 2\theta_{13}^{\mathrm{V}} - \sin^2 2\theta_{13}^{\mathrm{true}}]/\sin^2 2\theta_{13}^{\mathrm{true}}$ (top three panels), R_{VI} (next to top panels), R_{VII} (next next to top panels), and R_{VIII} (bottom three panels) defined in (6.75) in $\sin^2 2\theta_{13} - \delta/\pi$ space is presented for three typical cases of energies and baselines, SB1 (left panels), MB1 (middle panels), and MB2 (right panels) defined in Sec. 6.3.1. The regions of white color denote the regions of no degeneracy solution.
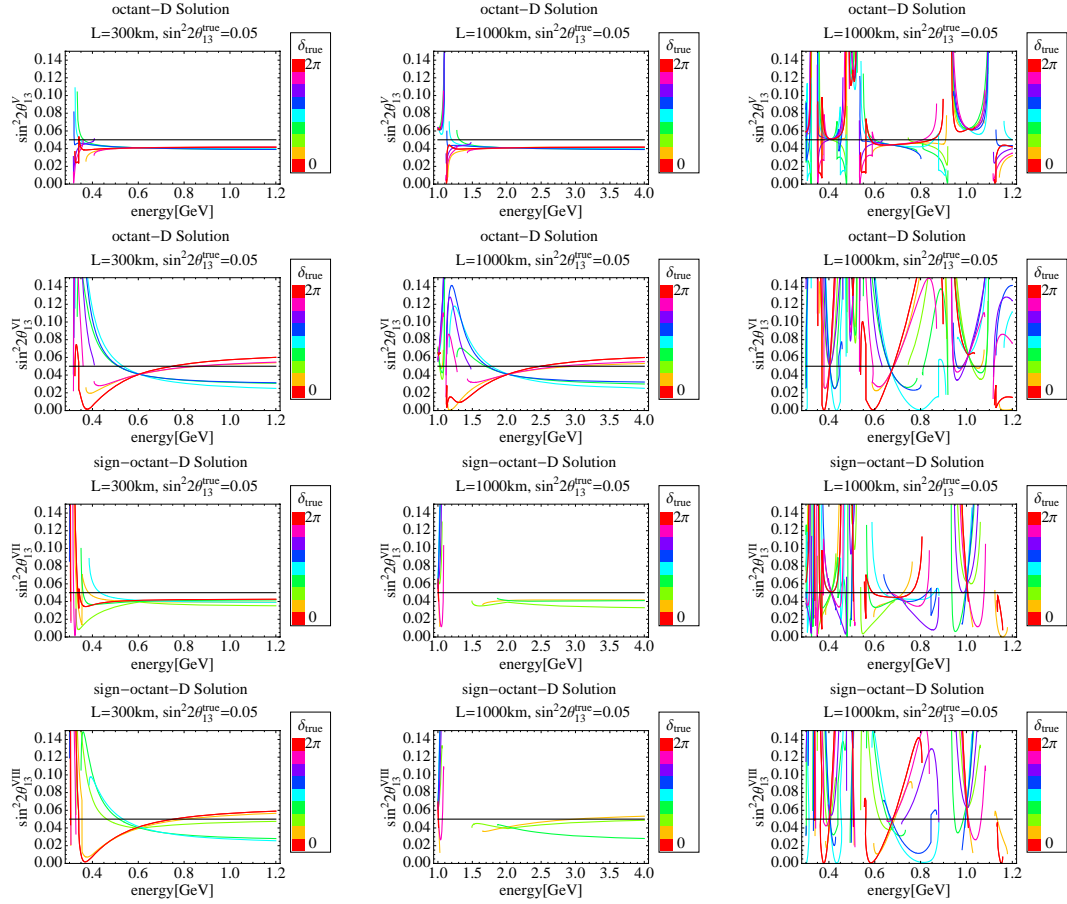
Figure 6.26: The energy dependence of $\sin^2 2\theta_{13}^{\text{V}}$ (top three panels), $\sin^2 2\theta_{13}^{\text{VI}}$ (next to top panels), $\sin^2 2\theta_{13}^{\text{VII}}$ (next next to top panels), and $\sin^2 2\theta_{13}^{\text{VIII}}$ (bottom three panels) are plotted for the three typical cases of energies and baselines SB1 (left panels), MB1 (middle panels), and MB2 (right panels) defined in Sec. 6.3.1. The true value of θ_{13} is taken as $\sin^2 2\theta_{13} = 0.05$, which is indicated by the horizontal solid line in the figure. The true value of θ_{23} is $42°$.
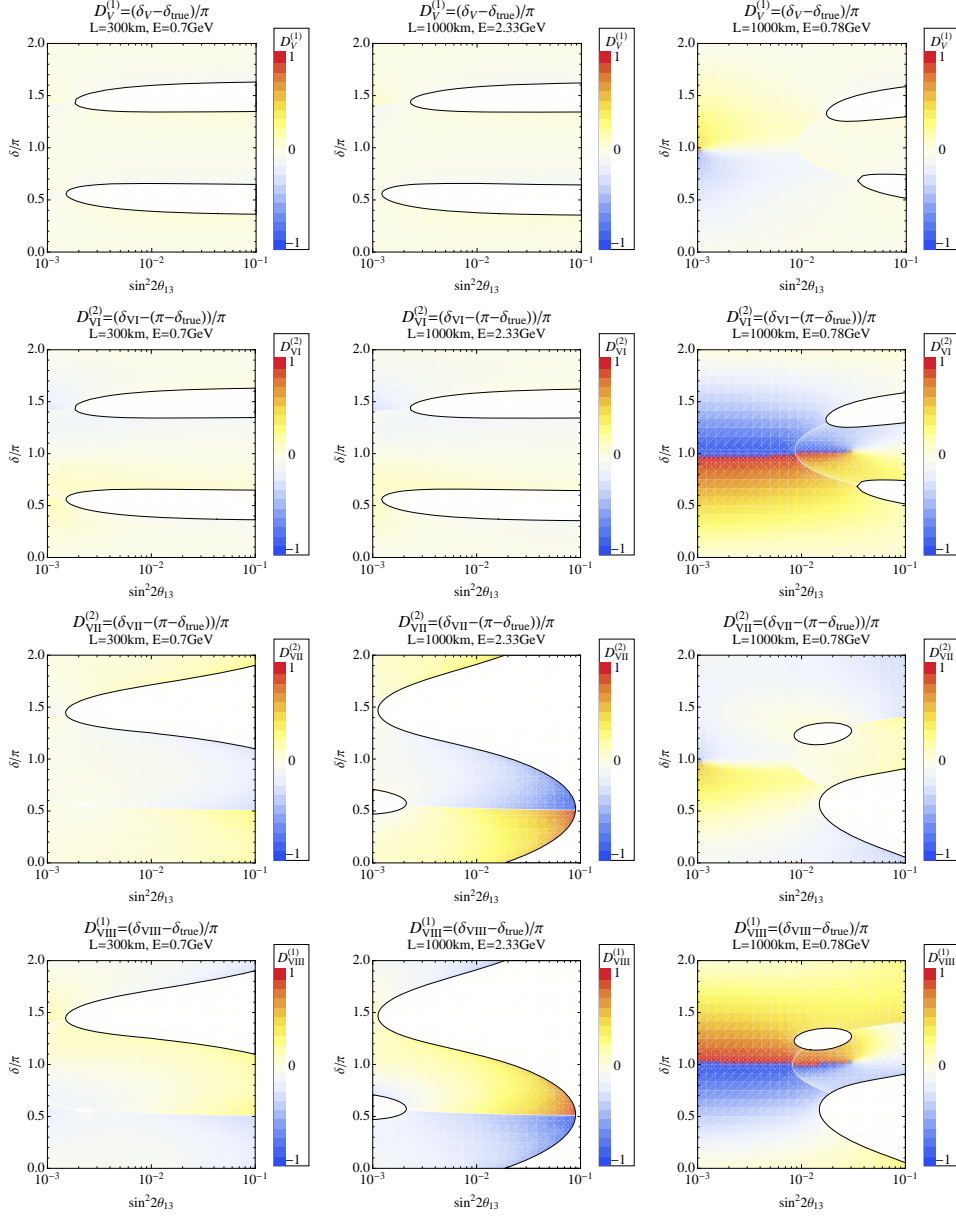
Figure 6.27: From top panels to bottom panels presented are in order: $D_V^{(1)} \equiv (\delta^V - \delta^{\text{true}})/\pi$, $D_{VI}^{(2)} \equiv [\delta^{VI} - (\pi - \delta^{\text{true}})]/\pi$, $D_{VII}^{(2)} \equiv [\delta^{VII} - (\pi - \delta^{\text{true}})]/\pi$, and $D_{VIII}^{(1)} \equiv (\delta^{VIII} - \delta^{\text{true}})/\pi$ defined in (6.76) for three typical cases of energies and baselines in $\sin^2 2\theta_{13}^{\text{true}} - \delta^{\text{true}}/\pi$ space. The regions of white color denote the regions of no sign-degeneracy solution.

74
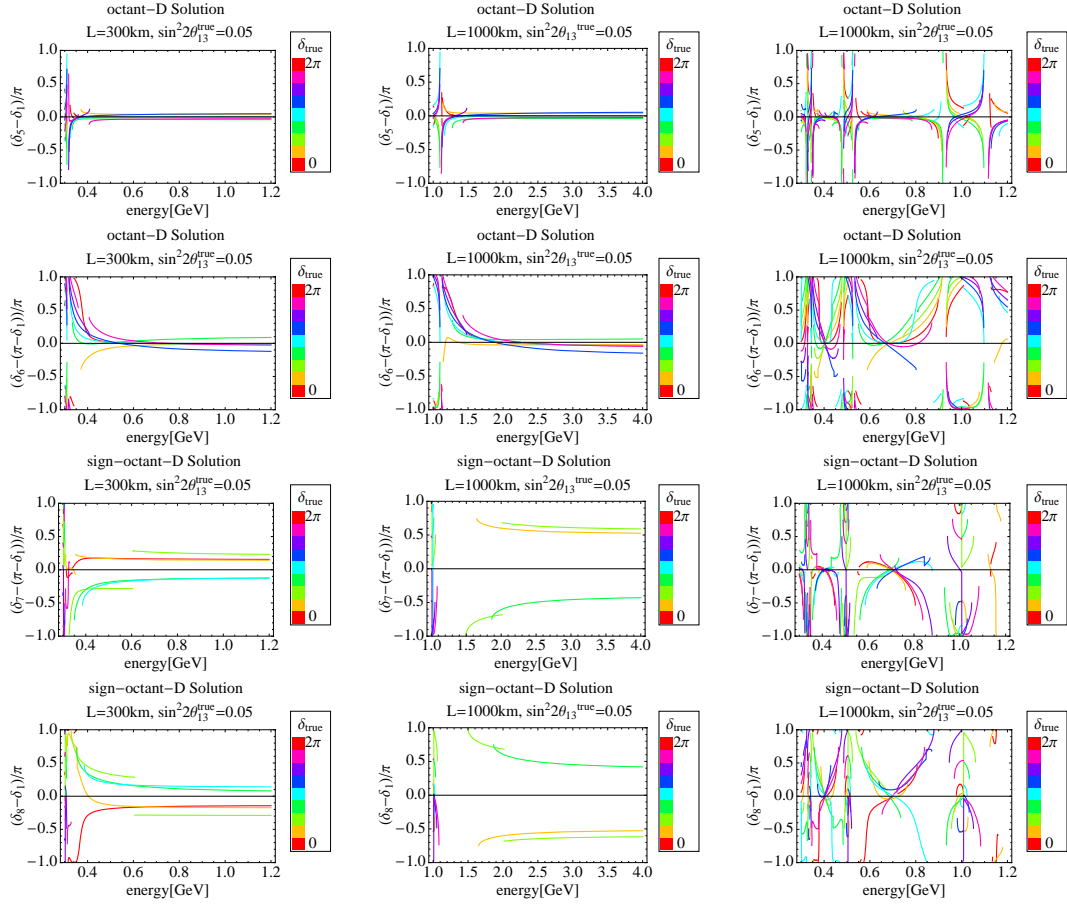
Figure 6.28: From top panels to bottom panels presented are in order: the energy dependence of $D_V^{(1)}$, $D_{VI}^{(2)}$, $D_{VII}^{(2)}$, and $D_{VIII}^{(1)}$ defined in (6.76) for the three typical cases of energies and baselines.

- In comparison with SB1 and MB1 settings, the features of degeneracy solutions are always quite distinct at MB2 setting, where the energy region around the second oscillation maximum is explored. It by itself, or combined with other settings, would provide ways to help resolving the eightfold degeneracy.

6.3.5 Parameter degeneracy in neutrino factory setting

In this subsection, we display the features of various degeneracy solutions by taking a setting which may be appropriate for neutrino factory. Though the two-detector setting with baselines $L = 3000 - 4000$ km and $L \sim 7000$ km seems to be considered as the "standard" one [87] both for measurement of standard mixing parameters [55, 63], possibly as well as for search for effects of NSI [83, 71, 64], we just use the setup with one detector at $L = 4000$ km and $E = 20$ GeV, to illuminate the features of the degeneracy.

Note that we have used set of probabilities $P(\nu_\mu \to \nu_e)$ and $P(\bar{\nu}_\mu \to \bar{\nu}_e)$ to obtain the degenerate solutions. Therefore, if we want to consider the more realistic setting of a neutrino factory in which T-conjugate (golden) channels will be used, regard δ as $2\pi - \delta$.

In Figs. 6.29 and 6.30, the differences between the true solution and the fake degeneracy solutions, R_N and $D_N^{(i)}$ (N=II−VIII, $i = 1$ or 2), respectively, are plotted. As can be seen in these figures the differences between the true solution and the fake degeneracy solutions are generically larger than the cases of superbeam type settings discussed in the previous subsections. In accord with the expected higher sensitivities, we extend the region of $\sin^2 2\theta_{13}$ to 10^{-4}.

Figs. 6.31 and 6.32 are same figure of Figs. 6.29 and 6.30 respectively but with different neutrino energy $E = 5$ GeV which is lower than the energy $\frac{\Delta m_{31}^2 L}{4E} = \pi/2$. One can realize the difference of no-degenerate region between the case of 20 GeV and 5 GeV. For R_{II} plot, the difference can be regarded as $\delta \to \delta - \pi/2$ and roughly speaking, difference of no-degenerate regions have also similar feature. Meanwhile, $D_{\mathrm{II}}^{(2)}$ does not have such feature. For 20 GeV setting, it has negative value in large θ_{13} region as $\sin^2 2\theta_{13} > 10^{-2}$ but 5 GeV setting has large value on the same region.

In Figs. 6.33 and 6.34, the energy dependences of $\sin^2 2\theta_{13}^N$ and $D_N^{(i)}$, respectively, are presented. Generally speaking, the energy dependences of both of the quantities are significant compared to those in the SB1 and MB1 settings. Notable exceptions are the solution V (both $\sin^2 2\theta_{13}^{\mathrm{V}}$ and $D_{\mathrm{V}}^{(1)}$), and possibly $\sin^2 2\theta_{13}^{\mathrm{III}}$ and $\sin^2 2\theta_{13}^{\mathrm{VII}}$, all except for the low energy region $E \lesssim 10$ GeV. Unless there is a sensitivity to the low-energy region it would be difficult to resolve the degeneracy, in particular V, by the spectrum informations. Therefore, it is extremely important to lower the threshold into $E \lesssim 10$ GeV to resolve the degeneracy by spectrum analysis. An extensive effort toward this direction is in progress [88].

It is possible to understand smallness and lack of strong energy dependence of the solutions V and VII, at least qualitatively. Because the θ_{23} perturbation theory also applies to NF setting, it can be expected that the difference between the true solution and the clone one V is small. The similar statement holds for the solution VII given the smallness of the energy dependent term in $\sin^2 2\theta_{13}^{\mathrm{III}}$. Then, the question is why $\sin^2 2\theta_{13}^{\mathrm{III}}$ is small and lacks the significant energy dependence despite that the matter perturbation theory is not

valid for NF setting. Qualitatively, the answer is that pinning to a small value due to the fact that the assumed true value itself is small, and lack of energy dependence because of fast reach to the asymptotic behavior discussed in Sec. 6.2.3.

One notices that the intrinsic solution II in NF setting has the similar features as the one in MB2 setting, as can be seen by comparing Figs. 6.29 and 6.30 to Figs. 6.12 and 6.13. It is because the value of θ_{13} taken is small and the atmospheric term is comparable to the solar term. Parallelism is not so complete in the other types of degeneracies, but some features can be understood in analogy to the case of MB2 setting.[3] In doing so the difference due to the much wider no-solution region of the sign-Δm_{31}^2 degeneracy due to long baseline must, of course, be taken into account.

Finally, we should note that abrupt termination of lines in the figures that appears in Figs. 6.33 and 6.34 are either due to disappearance of the degeneracy solutions, or switching phenomenon between solutions that takes place due to our convention of labeling degeneracy solutions. See Secs. 6.1.3, 6.1.4, and 6.1.5 for discussion on this point.
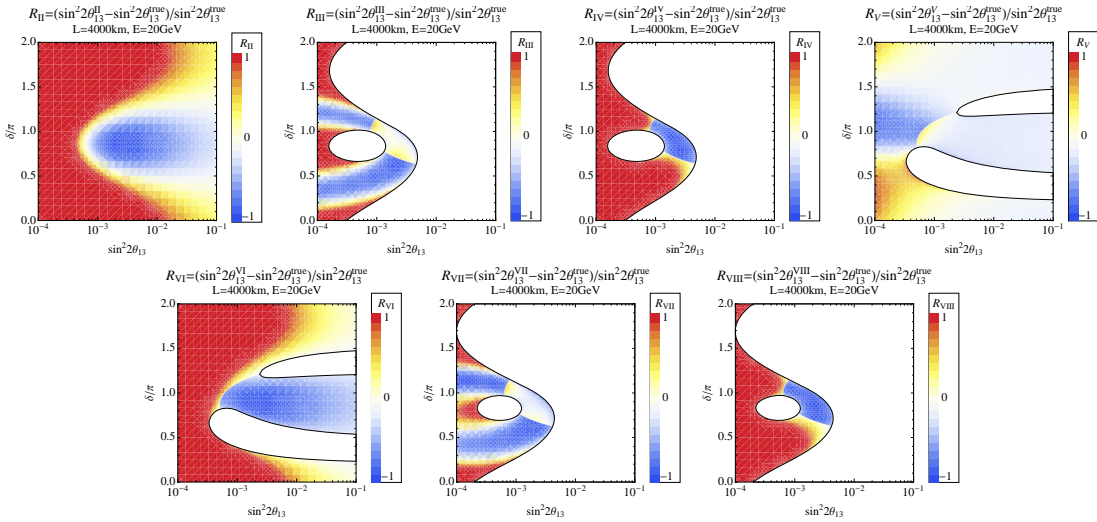
Figure 6.29: The ratio $R_{\mathrm{II}} - R_{\mathrm{VIII}}$ are plotted in $\sin^2 2\theta_{13} - \delta/\pi$ space for a typical baseline and energy of neutrino factory setting. The ratio R_{N} is defined as $R_{\mathrm{N}} = [\sin^2 2\theta_{13}^{\mathrm{N}} - \sin^2 2\theta_{13}^{\mathrm{true}}]/\sin^2 2\theta_{13}^{\mathrm{true}}$ defined in (6.75)

---

[3]An example is that there is the region that R_{V} is large in small θ_{13}. This is for the same reason of the case in MB2 setting, the difference between the true and V of order $\sim \epsilon_{\mathrm{oct}} Z$, is negligible compare with s_1. Another example is much stronger energy dependence of s_{II} in NF setting than SB1's, which is reminiscent of the feature of MB2 setting. It comes from larger effect of the solar-scale oscillation term.
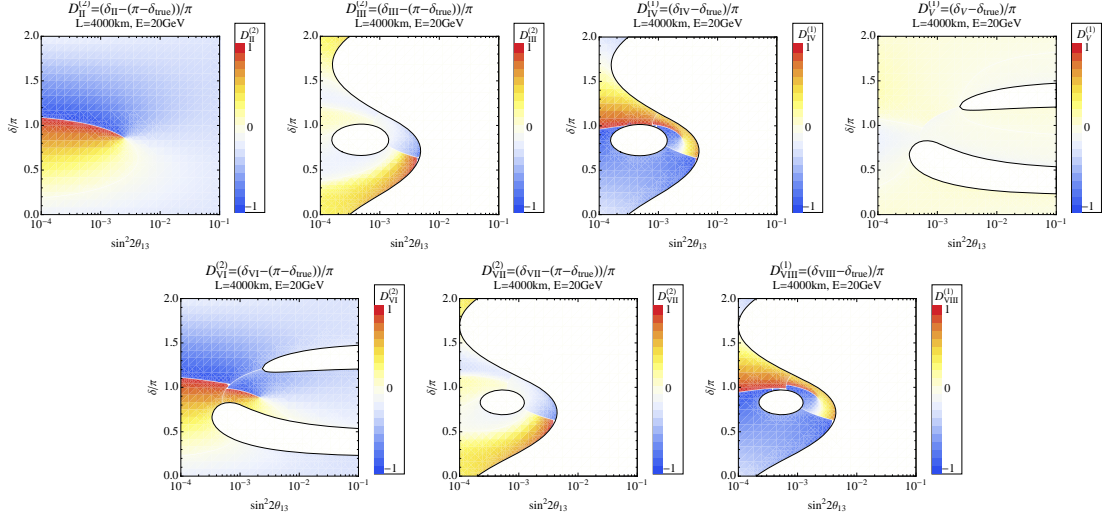
Figure 6.30: The normalized differences $D_{\mathrm{II}}^{(2)}$, $D_{\mathrm{III}}^{(2)}$, $D_{\mathrm{IV}}^{(1)}$, $D_{\mathrm{V}}^{(1)}$, $D_{\mathrm{VI}}^{(2)}$, $D_{\mathrm{VII}}^{(2)}$, and $D_{\mathrm{VIII}}^{(1)}$ are plotted in order in $\sin^2 2\theta_{13} - \delta/\pi$ space for a typical baseline and energy of neutrino factory setting. D_{N} is defined in (6.76) as $D_{\mathrm{N}}^{(2)} \equiv [\delta^{\mathrm{N}} - (\pi - \delta^{\mathrm{true}})]/\pi$ and $D_{\mathrm{N}}^{(1)} \equiv [\delta^{\mathrm{N}} - \delta^{\mathrm{true}}]/\pi$.
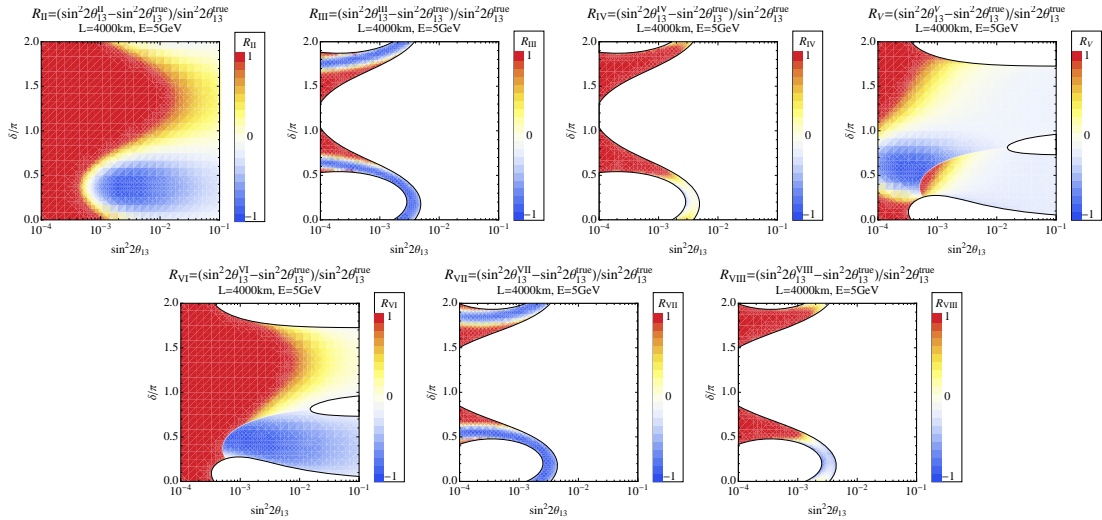
Figure 6.31: Same plot of Fig. 6.29 but with $E = 5$ GeV.

78
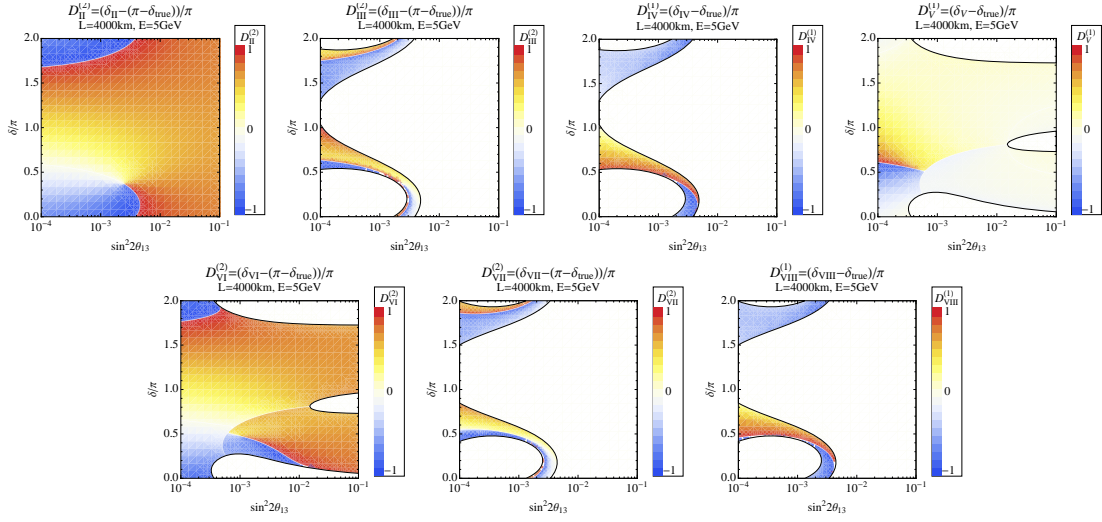
Figure 6.32: Same plot of Fig. 6.30 but with $E = 5$ GeV.
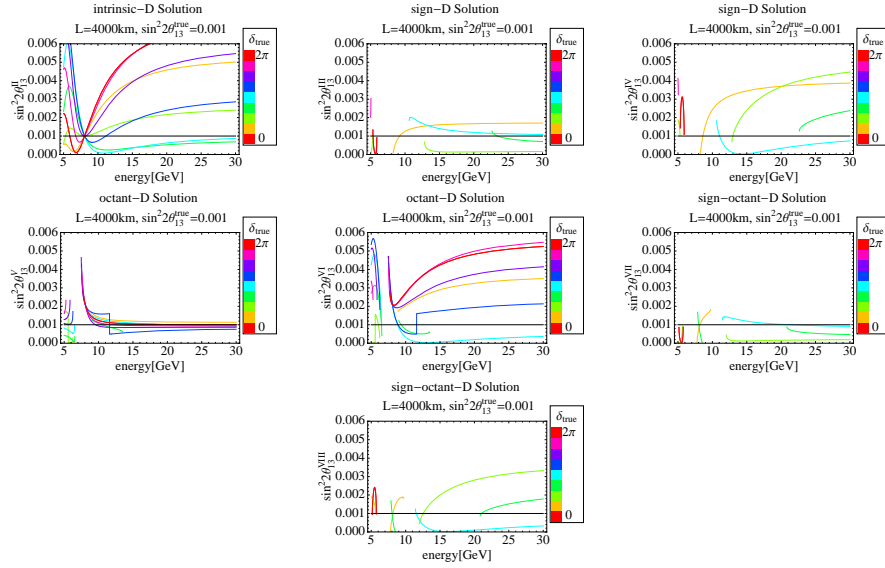
Figure 6.33: The energy dependences of $\sin^2 2\theta_{13}^{\mathrm{II}}$, $\sin^2 2\theta_{13}^{\mathrm{III}}$, $\sin^2 2\theta_{13}^{\mathrm{IV}}$, $\sin^2 2\theta_{13}^{\mathrm{V}}$, $\sin^2 2\theta_{13}^{\mathrm{VI}}$, $\sin^2 2\theta_{13}^{\mathrm{VII}}$, and $\sin^2 2\theta_{13}^{\mathrm{VIII}}$ are plotted in order. The true value of θ_{13} is taken as $\sin^2 2\theta_{13} = 0.001$, which is indicated by the horizontal solid line in the figure.
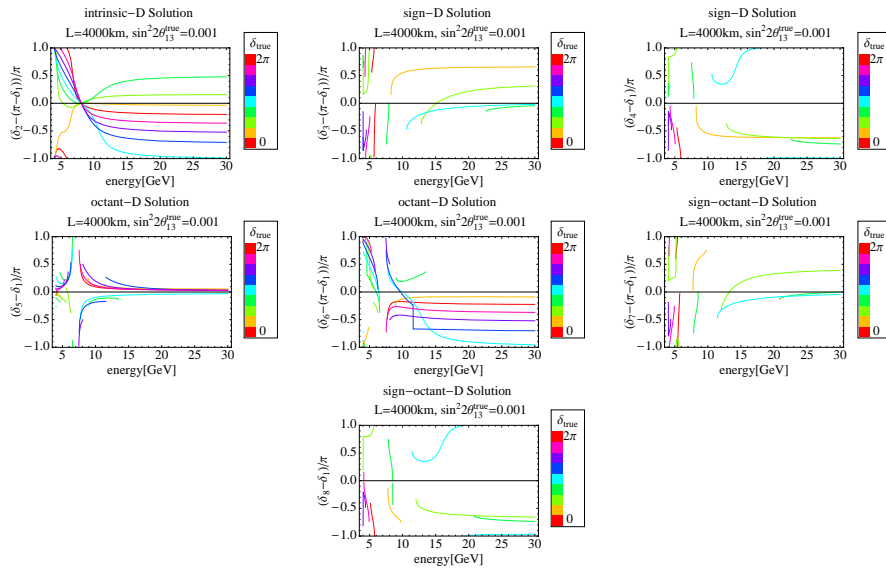
Figure 6.34: The energy dependences of $D_{\mathrm{II}}^{(2)}$, $D_{\mathrm{III}}^{(2)}$, $D_{\mathrm{IV}}^{(1)}$, $D_{\mathrm{V}}^{(1)}$, $D_{\mathrm{VI}}^{(2)}$, $D_{\mathrm{VII}}^{(2)}$, and $D_{\mathrm{VIII}}^{(1)}$ are plotted in order. $D_{\mathrm{N}}^{(1)}$ and $D_{\mathrm{N}}^{(2)}$ are defined in (6.76).

Chapter 7

Analytic Solution of Parameter Degeneracy in Various Measurement

In this chapter, we discuss analytic solutions of degeneracy in the T-conjugate measurement (Section 7.1), the CPT-conjugate (Section 7.3) measurement, and the golden-silver measurement combining the $\nu_e \to \nu_\mu$ (golden channel) and the $\nu_e \to \nu_\tau$ (silver channel) (Section 7.2). In these measurements, several types of degenerate solutions are directly determined by the symmetry of the approximate formulae of the oscillation probability.

7.1 Parameter degeneracy in T-conjugate measurement

In this section, we discuss the problem of parameter degeneracy in $P(\nu_\mu \to \nu_e)$ and its T-conjugate measurement in neutrino oscillation as illustrated in Fig. 7.1.

Though measurement of T violation does not appear to be feasible immediately understanding its structure may be interesting theoretically. It may be worth to note that the structure of the degeneracy with T-conjugate measurement is the simplest one among the cases discussed in this paper.

7.1.1 The intrinsic degeneracy in T-conjugate measurement

The intrinsic degeneracy solutions (s_i, δ_i) (i=1, 2) are defined in $\nu_\mu \to \nu_e$ channel by

$$
\begin{aligned}
P &= X_\pm^2 s_1^2 \pm 2X_\pm Z s_1 \left(\cos\delta_1 \cos\Delta_{31} \mp \sin\delta_1 \sin\Delta_{31}\right) + Z^2 \\
&= X_\pm^2 s_2^2 \pm 2X_\pm Z s_2 \left(\cos\delta_2 \cos\Delta_{31} \mp \sin\delta_2 \sin\Delta_{31}\right) + Z^2
\end{aligned}
\tag{7.1}
$$

and in T-conjugated channel by

$$
\begin{aligned}
P^T &= X_\pm^2 s_1^2 \pm 2X_\pm Z s_1 \left(\cos\delta_1 \cos\Delta_{31} \pm \sin\delta_1 \sin\Delta_{31}\right) + Z^2 \\
&= X_\pm^2 s_2^2 \pm 2X_\pm Z s_2 \left(\cos\delta_2 \cos\Delta_{31} \pm \sin\delta_2 \sin\Delta_{31}\right) + Z^2
\end{aligned}
\tag{7.2}
$$
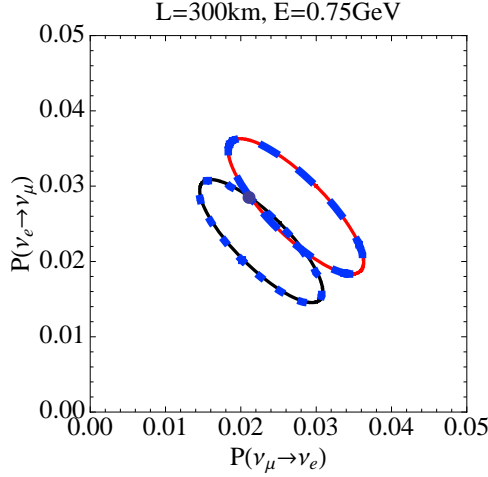
Figure 7.1: $P - P^T$ bi-probability plot by using perturbative formula. $\sin^2 2\theta_{13} = 0.05$ (black solid) with normal hierarchy, 0.061 (red solid) with normal hierarchy, 0.058 (blue dotted) with inverted hierarchy, 0.069 (blue dashed) with inverted hierarchy.

By adding and subtracting two equations (7.1) and (7.2), respectively, we obtain (assuming $Z \cos \Delta_{31} \neq 0$)

$$
\begin{aligned}
s_2 \sin \delta_2 &= s_1 \sin \delta_1 \\
s_2 \cos \delta_2 &= s_1 \cos \delta_1 \pm \frac{X_\pm}{2Z \cos \Delta_{31}} (s_1^2 - s_2^2)
\end{aligned}
\tag{7.3}
$$

Inserting (7.3) into $\cos^2 \delta_2 + \sin^2 \delta_2 = 1$ gives the equation for s_2 in a form $(s_2^2 - s_1^2)(s_2^2 - s_{\mathrm{II}}^2) = 1$. The intrinsic degeneracy solution is then written by

$$
s_{\mathrm{II}}^2 = s_1^2 \pm 2 \left(\frac{2Z \cos \Delta_{31}}{X_\pm} \right) s_1 \cos \delta_1 + \left(\frac{2Z_\pm \cos \Delta_{31}}{X_\pm} \right)^2 .
\tag{7.4}
$$

Given the solution $s_2 = s_{\mathrm{II}}$ the solution for δ_2 can be obtained by using (7.3) as

$$
\begin{aligned}
s_{\mathrm{II}} \sin \delta_{\mathrm{II}} &= s_1 \sin \delta_1, \\
s_{\mathrm{II}} \cos \delta_{\mathrm{II}} &= - \left(s_1 \cos \delta_1 \pm \frac{2Z \cos \Delta_{31}}{X_\pm} \right) .
\end{aligned}
\tag{7.5}
$$

7.1.2 The sign-Δm^2 degeneracy in T-conjugate measurement

We denote s_{13} variable for the opposite-sign Δm_{31}^2 solution as (s_3, δ_3), whose two (as we prove) solutions will be denoted as $(s_{\mathrm{III}}, \delta_{\mathrm{III}})$ and $(s_{\mathrm{IV}}, \delta_{\mathrm{IV}})$.

The sign-Δm_{31}^2 degeneracy is defined by the following two sets of equations:

$$
\begin{aligned}
P &= X_\pm^2 s_1^2 \pm 2X_\pm Z s_1 \left(\cos \delta_1 \cos \Delta_{31} \mp \sin \delta_1 \sin \Delta_{31} \right) + Z^2 \\
&= X_\mp^2 s_3^2 \mp 2X_\mp Z s_3 \left(\cos \delta_3 \cos \Delta_{31} \pm \sin \delta_3 \sin \Delta_{31} \right) + Z^2
\end{aligned}
\tag{7.6}
$$

$$\begin{aligned} P^T &= X_\pm^2 s_1^2 \pm 2X_\pm Z s_1 \left(\cos\delta_1 \cos\Delta_{31} \pm \sin\delta_1 \sin\Delta_{31} \right) + Z^2 \\ &= X_\mp^2 s_3^2 \mp 2X_\mp Z s_3 \left(\cos\delta_3 \cos\Delta_{31} \mp \sin\delta_3 \sin\Delta_{31} \right) + Z^2 \end{aligned} \tag{7.7}$$

By the similar procedure as in the previous subsection we obtain (assuming $X_\pm Z \cos\Delta_{31} \neq 0$)

$$\begin{aligned} s_3 \sin\delta_3 &= \left(\frac{X_\pm}{X_\mp} \right) s_1 \sin\delta_1, \\ s_3 \cos\delta_3 &= -\left(\frac{X_\pm}{X_\mp} \right) s_1 \cos\delta_1 \mp \frac{1}{2X_\mp Z \cos\Delta_{31}} \left(X_\pm^2 s_1^2 - X_\mp^2 s_3^2 \right) \end{aligned} \tag{7.8}$$

Inserting (7.8) into $\cos^2\delta_3 + \sin^2\delta_3 = 1$ leads to the equation for s_3^2 as

$$\left(s_3^2 - \frac{X_\pm^2}{X_\mp^2} s_1^2 \right) \left(s_3^2 - \frac{X_\pm^2}{X_\mp^2} s_{\mathrm{II}}^2 \right) = 0, \tag{7.9}$$

where s_{II} is defined in (7.4). Thus, the sign-Δm_{31}^2 degenerate solutions are given by

$$\begin{aligned} s_{\mathrm{III}} &= \frac{X_\pm}{X_\mp} s_1, \\ s_{\mathrm{IV}} &= \frac{X_\pm}{X_\mp} s_{\mathrm{II}}. \end{aligned} \tag{7.10}$$

The solutions for CP phase δ can be obtained by inserting these solutions into (7.8) as

$$\begin{aligned} \delta_{\mathrm{III}} &= \pi - \delta_1, \\ \delta_{\mathrm{IV}} &= \pi - \delta_{\mathrm{II}}. \end{aligned} \tag{7.11}$$

Figure 7.1 clearly exhibits the structure obtained in (7.11).

7.1.3 The θ_{23} octant degeneracy in T-conjugate measurement

The θ_{23} octant degeneracy in the same hierarchy is defined by the following equations,

$$\begin{aligned} P &= s_{23}^2 X_\pm'^2 s_1^2 \pm 2 s_{23} c_{23} X_\pm' Z' s_1 \left(\cos\delta_1 \cos\Delta_{31} \mp \sin\delta_1 \sin\Delta_{31} \right) + c_{23}^2 Z'^2, \\ &= c_{23}^2 X_\pm'^2 s_5^2 \pm 2 s_{23} c_{23} X_\pm' Z' s_5 \left(\cos\delta_5 \cos\Delta_{31} \mp \sin\delta_5 \sin\Delta_{31} \right) + s_{23}^2 Z'^2, \end{aligned} \tag{7.12}$$

$$\begin{aligned} P^T &= s_{23}^2 X_\pm'^2 s_1^2 \pm 2 s_{23} c_{23} X_\pm' Z' s_1 \left(\cos\delta_1 \cos\Delta_{31} \pm \sin\delta_1 \sin\Delta_{31} \right) + c_{23}^2 Z'^2, \\ P^T &= c_{23}^2 X_\pm'^2 s_5^2 \pm 2 s_{23} c_{23} X_\pm' Z' s_5 \left(\cos\delta_5 \cos\Delta_{31} \pm \sin\delta_5 \sin\Delta_{31} \right) + s_{23}^2 Z'^2. \end{aligned} \tag{7.13}$$

From these equations, we obtain

$$\begin{aligned} s_5 \cos\delta_5 &= s_1 \cos\delta_1 + \frac{(s_{23}^2 s_1^2 - c_{23}^2 s_5^2) X_\pm'^2 + Z'^2 \cos 2\theta_{23}}{2 s_{23} c_{23} X_\pm' Z' \cos\Delta_{31}} \\ s_5 \sin\delta_5 &= s_1 \sin\delta_1. \end{aligned} \tag{7.14}$$

The relation $\cos^2 \delta_5 + \sin^2 \delta_5 = 1$ gives the quadratic equation for s_5^2 which results in the similar solution

$$
s_{\mathrm{V,VI}}^2 = \frac{1}{c_{23}^2 X_{\pm}^{\prime 2}} \left[s_1^2 s_{23}^2 X_{\pm}^{\prime 2} + \cos 2\theta_{23} Z^{\prime 2} \right.
$$

$$
\left. \pm 2 c_{23} s_{23} s_1 X_{\pm}^{\prime} Z^{\prime} \cos \delta_1 \cos \Delta_{31} + 2 s_{23}^2 Z^{\prime 2} \cos^2 \Delta_{31} \left[\mp \right] d_{\pm}^{\text{T-oct-intr}} \sqrt{\frac{D_{\pm}^{\text{T-oct-intr}}}{(d_{\pm}^{\text{T-oct-intr}})^2}} \right],
$$

$$(7.15)$$

where the upper (lower) $[\mp]$ sign is for s_{V} (s_{VI}). The functions $D_{\pm}^{\text{T-oct-intr}}$ and $d_{\pm}^{\text{T-oct-intr}}$ are defined by

$$
D_{\pm}^{\text{T-oct-intr}} \equiv (2 s_{23} Z^{\prime} \cos \Delta_{31})^2 \left[(\pm c_{23} s_1 X_{\pm}^{\prime} \cos \delta_1 + s_{23} Z^{\prime} \cos \Delta_{31})^2 - \cos 2\theta_{23}(s_1^2 X_{\pm}^{\prime 2} - Z^{\prime 2}) \right]
$$

$$
d_{\pm}^{\text{T-oct-intr}} \equiv \lim_{\theta_{23} \to \pi/4} D_{\pm}^{\text{T-oct-intr}} = (\pm s_1 X_{\pm}^{\prime} \cos \delta_1 + Z^{\prime} \cos \Delta_{31}) Z^{\prime} \cos \Delta_{31}. \qquad (7.16)
$$

Once the solutions s_{V} and s_{VI} are known one can readily obtain δ_{V} and δ_{VI} by inserting (7.15) into (7.14).

As we discussed in Section6.2.1, we can easily obtain the solution of $(s_{\mathrm{VII}}, \delta_{\mathrm{VII}})$ and $(s_{\mathrm{VIII}}, \delta_{\mathrm{VIII}})$, the degeneracy with both the Δm_{31}^2-sign and the octant flips, by using the solutions obtained in this subsection as

$$
s_{\mathrm{VII}} = \frac{X_{\pm}^{\prime}}{X_{\mp}^{\prime}} s_{\mathrm{V}}, \qquad \delta_{\mathrm{VII}} = \pi - \delta_{\mathrm{V}},
$$

$$
s_{\mathrm{VIII}} = \frac{X_{\pm}^{\prime}}{X_{\mp}^{\prime}} s_{\mathrm{VI}}, \qquad \delta_{\mathrm{VIII}} = \pi - \delta_{\mathrm{VI}}. \qquad (7.17)
$$

7.2 Parameter degeneracy with golden and silver channels

We discuss the parameter degeneracy for a given measurement in the $\nu_e \to \nu_\mu$ (golden) and the $\nu_e \to \nu_\tau$ (silver) channels. The oscillation probability in the former and the latter channels are given by P^T in (5.33) and P^S in (5.35), respectively.

7.2.1 The intrinsic degeneracy in Golden-Silver measurement

The intrinsic degeneracy is defined by

$$
\begin{aligned}
P^T &= X_{\pm}^2 s_1^2 \pm 2 X_{\pm} Z s_1 \left(\cos \delta_1 \cos \Delta_{31} \pm \sin \delta_1 \sin \Delta_{31} \right) + Z^2 \\
&= X_{\pm}^2 s_2^2 \pm 2 X_{\pm} Z s_2 \left(\cos \delta_2 \cos \Delta_{31} \pm \sin \delta_2 \sin \Delta_{31} \right) + Z^2
\end{aligned} \qquad (7.18)
$$

and

$$
\begin{aligned}
P^S &= \cot^2 \theta_{23} X_{\pm}^2 s_1^2 \mp 2 X_{\pm} Z s_1 \left(\cos \delta_1 \cos \Delta_{31} \pm \sin \delta_1 \sin \Delta_{31} \right) + \tan^2 \theta_{23} Z^2 \\
&= \cot^2 \theta_{23} X_{\pm}^2 s_2^2 \mp 2 X_{\pm} Z s_2 \left(\cos \delta_2 \cos \Delta_{31} \pm \sin \delta_2 \sin \Delta_{31} \right) + \tan^2 \theta_{23} Z^2 \quad (7.19)
\end{aligned}
$$

Adding two equations (7.18) and (7.19) gives the solution of s_2 directly as

$$s_1^2 = s_2^2. \tag{7.20}$$

That is the degeneracy solution of θ_{13} is given by $s_{\mathrm{II}} = s_1$.

Using this solution, we obtain

$$\cos(\delta_2 \mp \Delta_{31}) = \cos(\delta_1 \mp \Delta_{31}). \tag{7.21}$$

Ignoring the trivial solution $\delta_2 = \delta_1$, the intrinsic degeneracy solution of δ is given by

$$\delta_{\mathrm{II}} = -(\delta_1 \mp 2\Delta_{31}). \tag{7.22}$$

The structure of the solutions of θ_{13} and δ should be obvious from the form of the oscillation probabilities in (7.18) and (7.19); The shrunk ellipse (Fig. 7.2) implies that there is no θ_{13} degeneracy and the two δ solutions must have the same values of $\cos(\delta \mp \Delta_{31})$.
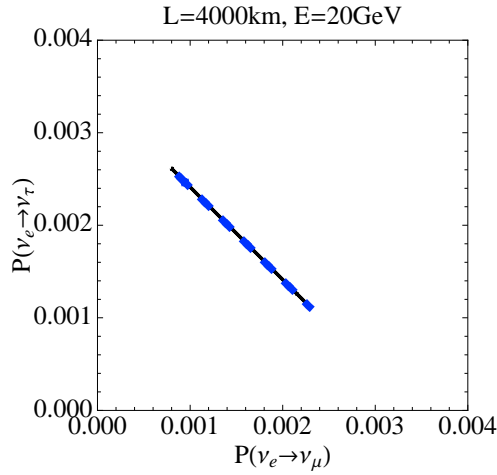
Figure 7.2: $P^T - P^S$ (Golden-Silver) bi-probability. The black solid (blue dashed) line is varying $\delta : 0 \to 2\pi$ with normal (inverted) mass hierarchy and $\sin^2 2\theta_{13} = 0.01(0.039)$.

7.2.2 The sign-Δm^2 degeneracy in Golden-Silver measurement

The sign-Δm^2 degeneracy is defined by

$$
\begin{aligned}
P^T &= X_\pm^2 s_1^2 \pm 2X_\pm Z s_1 \left(\cos\delta_1 \cos\Delta_{31} \pm \sin\delta_1 \sin\Delta_{31}\right) + Z^2 \\
&= X_\mp^2 s_3^2 \mp 2X_\mp Z s_3 \left(\cos\delta_3 \cos\Delta_{31} \mp \sin\delta_3 \sin\Delta_{31}\right) + Z^2
\end{aligned} \tag{7.23}
$$

$$
\begin{aligned}
P^S &= \cot^2\theta_{23} X_\pm^2 s_1^2 \mp 2X_\pm Z s_1 \left(\cos\delta_1 \cos\Delta_{31} \pm \sin\delta_1 \sin\Delta_{31}\right) + \tan^2\theta_{23} Z^2 \\
&= \cot^2\theta_{23} X_\mp^2 s_3^2 \pm 2X_\mp Z s_3 \left(\cos\delta_3 \cos\Delta_{31} \mp \sin\delta_3 \sin\Delta_{31}\right) + \tan^2\theta_{23} Z^2
\end{aligned} \tag{7.24}
$$

By adding two equations (7.23) and (7.24) we obtain

$$s_3^2 = \frac{X_\pm^2}{X_\mp^2} s_1^2. \tag{7.25}$$

Thus we have the solution of sign-Δm_{31}^2 degeneracy,

$$s_{\text{III}} = s_{\text{IV}} = \frac{X_\pm}{X_\mp} s_1 \tag{7.26}$$

The relationship of $s_{\text{III}} = s_{\text{IV}}$ is nothing but a copy of true and intrinsic solution; $s_{\text{II}} = s_1$.

By using (7.25), one can easily obtain the sign-Δm_{31}^2 solution for δ which satisfy the equation

$$\cos(\delta_3 \pm \Delta_{31}) = -\cos(\delta_1 \mp \Delta_{31}), \tag{7.27}$$

Therefore, we obtain

$$
\begin{aligned}
\delta_{\text{III}} &= \pi - \delta_1, \\
\delta_{\text{IV}} &= \pi - \delta_{\text{II}} = \pi + \delta_1 \mp 2\Delta_{31}.
\end{aligned} \tag{7.28}
$$

7.2.3 The octant degeneracy in Golden-Silver measurement

Now, we discuss the θ_{23} octant degeneracy in Golden-Silver measurement. The θ_{23} octant degeneracy solutions (s_5, δ_5) satisfy

$$
\begin{aligned}
P^T &= s_{23}^2 X_\pm'^2 s_1^2 \pm 2X_\pm' Z' s_1 \left(\cos\delta_1 \cos\Delta_{31} \pm \sin\delta_1 \sin\Delta_{31}\right) + c_{23}^2 Z'^2, \\
&= c_{23}^2 X_\pm'^2 s_5^2 \pm 2X_\pm' Z' s_5 \left(\cos\delta_5 \cos\Delta_{31} \pm \sin\delta_5 \sin\Delta_{31}\right) + s_{23}^2 Z'^2,
\end{aligned} \tag{7.29}
$$

and

$$
\begin{aligned}
P^S &= c_{23}^2 X_\pm'^2 s_1^2 \mp 2X_\pm' Z' s_1 \left(\cos\delta_1 \cos\Delta_{31} \pm \sin\delta_1 \sin\Delta_{31}\right) + s_{23}^2 Z'^2, \\
&= s_{23}^2 X_\pm'^2 s_5^2 \mp 2X_\pm' Z' s_5 \left(\cos\delta_5 \cos\Delta_{31} \pm \sin\delta_5 \sin\Delta_{31}\right) + c_{23} Z'^2.
\end{aligned} \tag{7.30}
$$

By adding two equations (7.29) and (7.30), it gives the simple solution of s_5 as $s_5^2 = s_1^2$ which leads to

$$s_{\text{V}} = s_{\text{VI}} = s_1. \tag{7.31}$$

To obtain δ_5, we proceed as usual which leads to the result

$$\cos(\delta_{\text{V}} \mp \Delta_{31}) = \cos(\delta_1 \mp \Delta_{31}) - \frac{\cot 2\theta_{23}(s_1^2 X_\pm'^2 - Z'^2)}{s_1 X_\pm' Z'} \tag{7.32}$$

Because of the intrinsic relation of the solution V and VI, δ_{VI} is given as

$$\delta_{\text{VI}} = -(\delta_V \mp 2\Delta_{31}). \tag{7.33}$$

As in the case of T-conjugate measurement described in Sec. 7.1.3, the solutions $(s_{\text{VII}}, \delta_{\text{VII}})$ and $(s_{\text{VII}}, \delta_{\text{VII}})$, which is the solution of sign-octant degeneracy, can be obtained as

$$
\begin{aligned}
s_{\text{VII}} &= s_{\text{VIII}} = \frac{X_\pm'}{X_\mp'} s_{\text{V}}, \\
\delta_{\text{VII}} &= \pi - \delta_{\text{V}}, \qquad \delta_{\text{VIII}} = \pi - \delta_{\text{VI}}.
\end{aligned} \tag{7.34}
$$

7.3 Parameter degeneracy in CPT-conjugate measurement

We discuss in this section the problem of parameter degeneracy in $P(\nu_\mu \to \nu_e)$ and its CPT-conjugate measurement.

7.3.1 The intrinsic degeneracy in CPT-conjugate measurement

The intrinsic degeneracy solutions (s_i, δ_i) (i=1, 2) are defined by

$$
\begin{aligned}
P &= X_\pm^2 s_1^2 \pm 2X_\pm Z s_1 \left(\cos\delta_1 \cos\Delta_{31} \mp \sin\delta_1 \sin\Delta_{31}\right) + Z^2, \\
&= X_\pm^2 s_2^2 \pm 2X_\pm Z s_2 \left(\cos\delta_2 \cos\Delta_{31} \mp \sin\delta_2 \sin\Delta_{31}\right) + Z^2,
\end{aligned}
\tag{7.35}
$$

and in CPT-conjugate $\bar\nu_e \to \bar\nu_\mu$ channel by

$$
\begin{aligned}
P^{CPT} &= X_\mp^2 s_1^2 \pm 2X_\mp Z s_1 \left(\cos\delta_1 \cos\Delta_{31} \mp \sin\delta_1 \sin\Delta_{31}\right) + Z^2, \\
&= X_\mp^2 s_2^2 \pm 2X_\mp Z s_2 \left(\cos\delta_2 \cos\Delta_{31} \mp \sin\delta_2 \sin\Delta_{31}\right) + Z^2.
\end{aligned}
\tag{7.36}
$$

Assuming $X_\pm \neq 0$, subtracting two equations $(7.35)/X_\pm$ and $(7.36)/X_\mp$ gives

$$
s_2^2 = s_1^2.
\tag{7.37}
$$

Thus we obtain the intrinsic degenerate solution of θ_{13} as $s_{\mathrm{II}} = s_1$, that is consistent with the expectation from the bi-probability plot Fig. 7.3. Inserting (7.37) into (7.35), the solution of δ is written by

$$
\delta_{\mathrm{II}} = -\delta_1 \mp 2\Delta_{31}.
\tag{7.38}
$$

7.3.2 The sign-Δm^2 degeneracy in CPT-conjugate measurement

We next discuss the sign-Δm_{31}^2 degeneracy in CPT-conjugate measurement. The clone solution (s_3, δ_3) with Δm_{31}^2-sign flipped satisfy the following equations. In the $\nu_\mu \to \nu_e$ channel,

$$
\begin{aligned}
P &= X_\pm^2 s_1^2 \pm 2X_\pm Z s_1 \left(\cos\delta_1 \cos\Delta_{31} \mp \sin\delta_1 \sin\Delta_{31}\right) + Z^2, \\
&= X_\mp^2 s_3^2 \mp 2X_\mp Z s_3 \left(\cos\delta_3 \cos\Delta_{31} \pm \sin\delta_3 \sin\Delta_{31}\right) + Z^2,
\end{aligned}
\tag{7.39}
$$

and in the CPT-conjugate channel

$$
\begin{aligned}
P^{CPT} &= X_\mp^2 s_1^2 \pm 2X_\mp Z s_1 \left(\cos\delta_1 \cos\Delta_{31} \mp \sin\delta_1 \sin\Delta_{31}\right) + Z^2, \\
&= X_\pm^2 s_3^2 \mp 2X_\pm Z s_3 \left(\cos\delta_3 \cos\Delta_{31} \pm \sin\delta_3 \sin\Delta_{31}\right) + Z^2.
\end{aligned}
\tag{7.40}
$$

Combing (7.39) and (7.40) by the similar manner in the previous subsection, we obtain

$$
(X_\mp - X_\pm)s_3^3 = \frac{s_1^2(X_\pm^3 - X_\mp^3) \pm 2s_1 Z(X_\pm^2 - X_\mp^2)\cos(\delta_1 \pm \Delta_{31})}{X_\pm X_\mp},
\tag{7.41}
$$
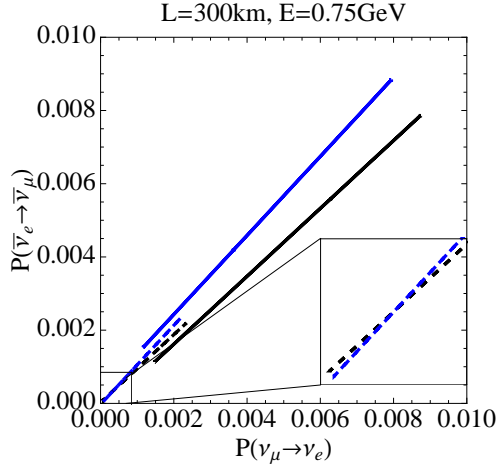
Figure 7.3: $P - P^{CPT}$ bi-probability plot. The black and the blue solid (dashed) lines, which correspond respectively to the normal and the inverted hierarchies, are for $\sin^2 2\theta_{13} = 0.01(0.001)$. The region with small probabilities $P \leq 0.0007$ is magnified into the sub-panel to show more clearly the crossing of the two shrunk ellipses in the region.

and then

$$s_{\text{III}} = s_{\text{IV}} = \sqrt{\frac{-s_1^2(X_\pm^3 - X_\mp^3) \mp 2s_1 Z(X_\pm^2 - X_\mp^2)\cos(\delta_1 \pm \Delta_{31})}{X_\pm X_\mp (X_\pm - X_\mp)}}. \qquad (7.42)$$

If the inside of square root is negative, sign-Δm_{31} degenerate solutions do not exist. In Fig. 7.4 shown as the shaded areas are the region of absence of the degeneracy. As we can imagine from bi-probability plot in Fig. 7.3, degeneracy exists at small values of θ_{13}. Upon
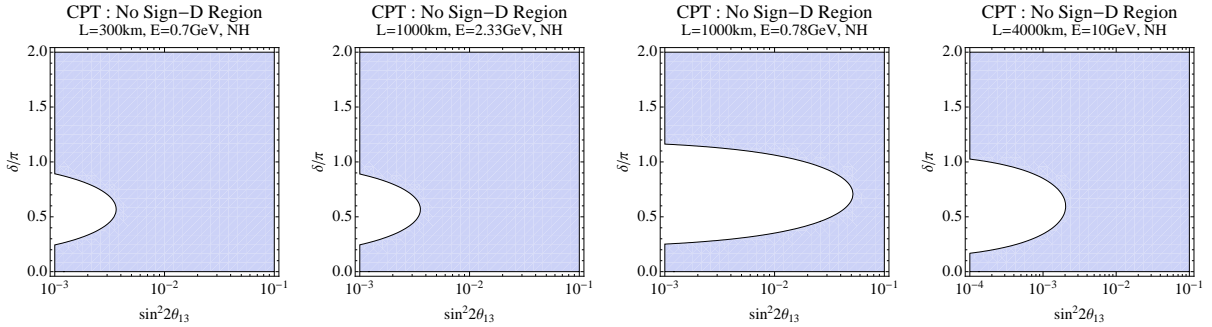
Figure 7.4: Parameter region with shade where sign-Δm_{31}^2 degeneracy in CPT measurement does not exist. The neutrino mass hierarchy is taken the normal one.

obtaining the s_3 solution one can readily obtain δ_3 by solving (7.41) for $\cos(\delta_3 \mp \Delta_{31})$. The

solutions of δ read

$$s_{\mathrm{III}} \cos(\delta_{\mathrm{III}} \mp \Delta_{31})$$
$$= \frac{\mp s_1^2 (X_\pm + X_\mp)(X_\pm^2 + X_\mp^2) - 2s_1 Z(X_\pm^2 + X_\pm X_\mp + X_\mp^2) \cos(\delta_1 \pm \Delta_{31})}{2X_\pm X_\mp Z}, \quad (7.43)$$

and

$$\delta_{\mathrm{IV}} = -\delta_{\mathrm{III}} \mp 2\Delta_{31} \qquad (7.44)$$

7.3.3 The octant degeneracy in CPT-conjugate measurement

The θ_{23} octant degeneracy is defined by the following two sets of equations:

$$\begin{aligned} P &= s_{23}^2 X_\pm'^2 s_1^2 \pm 2s_{23}c_{23}X_\pm' Z' s_1 \left(\cos\delta_1 \cos\Delta_{31} \mp \sin\delta_1 \sin\Delta_{31}\right) + c_{23}^2 Z'^2, \\ &= c_{23}^2 X_\pm'^2 s_5^2 \pm 2s_{23}c_{23}X_\pm' Z' s_5 \left(\cos\delta_5 \cos\Delta_{31} \mp \sin\delta_5 \sin\Delta_{31}\right) + s_{23}^2 Z'^2. \end{aligned} \quad (7.45)$$

$$\begin{aligned} P^{CPT} &= s_{23} X_\mp'^2 s_1^2 \pm 2s_{23}c_{23}X_\mp' Z' s_1 \left(\cos\delta_1 \cos\Delta_{31} \mp \sin\delta_1 \sin\Delta_{31}\right) + c_{23}^2 Z'^2, \\ &= c_{23}^2 X_\mp'^2 s_5^2 \pm 2s_{23}c_{23}X_\mp' Z' s_5 \left(\cos\delta_5 \cos\Delta_{31} \mp \sin\delta_5 \sin\Delta_{31}\right) + s_{23}^2 Z'^2. \end{aligned} \quad (7.46)$$

Following the similar procedure as before it is not difficult to obtain the equation which involve neither δ_5 nor δ_1. We obtain

$$s_{\mathrm{V}} = s_{\mathrm{VI}} = \tan\theta_{23} \sqrt{s_1^2 - \frac{\cos 2\theta_{23} Z'^2}{s_{23}^2 X_\pm' X_\mp'}}. \qquad (7.47)$$

Then, the phase δ_5 is determined as

$$s_{\mathrm{V}} \cos(\delta_{\mathrm{V}} \pm \Delta_{31}) = s_1 \cos(\delta_1 \pm \Delta_{31}) \mp \cot 2\theta_{23} \frac{Z'}{X_\pm'} \qquad (7.48)$$

As in the previous section the intrinsic degeneracy partner δ_{VI} is given by using (7.38) as

$$\delta_{\mathrm{VI}} = -\delta_V \mp 2\Delta_{31}. \qquad (7.49)$$

Fig. 7.5 shows the region that (7.47) is not a physical solution, i.e. no sign-Δm_{31}^2 degeneracy. If θ_{23} lives in second octant; $\cos 2\theta_{23} < 0$, octant degeneracy always exist unless the special case $X_\pm X_\mp < 0$ which is close to vacuum oscillation minimum.

As in the previous cases, the solutions of sign-octant degeneracy, $(s_{\mathrm{VII}}, \delta_{\mathrm{VII}})$ and $(s_{\mathrm{VII}}, \delta_{\mathrm{VII}})$, are given by the general argument as

$$\begin{aligned} s_{\mathrm{VII}} &= s_{\mathrm{VIII}} = \xi_\pm^{\mathrm{CPT}} \left(s_{\mathrm{V}}, \delta_{\mathrm{V}}, \pi/2 - \theta_{23}^{\mathrm{true}}\right) \\ \delta_{\mathrm{VII}} &= \eta_\pm^{\mathrm{CPT\ sign}}(s_{\mathrm{V}}, \delta_{\mathrm{V}}, \pi/2 - \theta_{23}^{\mathrm{true}}), \qquad \delta_{\mathrm{VIII}} = \eta_\pm^{\mathrm{CPT\ sign}}(s_{\mathrm{VI}}, \delta_{\mathrm{VI}}, \pi/2 - \theta_{23}^{\mathrm{true}}), \end{aligned} \quad (7.50)$$

where $\xi_\pm^{\mathrm{CPT\ sign}}$ and $\eta_\pm^{\mathrm{CPT\ sign}}$ are defined in (7.42) and inverse function for δ_{III} in (7.43), respectively, as a function of $(s_1, \delta_1, \theta_{23}^{\mathrm{true}})$.
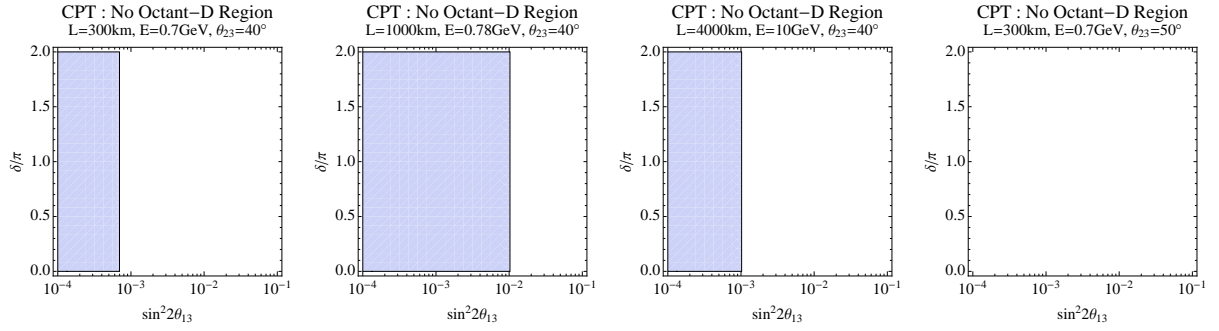
Figure 7.5: Parameter region with shade where θ_{23} octant degeneracy in CPT measurement does not exist. As indicated in the rightmost panel, the octant degeneracy solutions always exist for true θ_{23} in the second octant, as explained in the text.

Chapter 8

Parameter Degeneracy with Non-Standard Interaction

In this chapter, we show the parameter degeneracy caused by the non-standard neutrino interaction (NSI) [5, 65, 66, 67, 68] with matter. Especially, we consider the NSI only in propagation as the non-standard neutral-current interaction like

$$L_{\text{eff}}^{\text{NSI}} = -2\sqrt{2}\varepsilon_{\alpha\beta}^{fP}G_F(\bar{\nu}_\alpha\gamma_\mu P_L\nu_\beta)(\bar{f}\gamma^\mu Pf), \qquad (8.1)$$

where G_F is the Fermi constant, f stands for the index running over fermion species in the earth, $f = e, u, d$, and P stands for a projection operator which is either $P_L \equiv (1 - \gamma_5)/2$ or $P_R \equiv (1 + \gamma_5)/2$, and $\alpha, \beta = e, \mu, \tau$.

This type of interaction affect on the Hamiltonian as the direct flavor changing effect in off-diagonal elements or non-universal neutral-current in diagonal elements. To summarize effects on neutrino propagation it is customary to introduce the effective $\varepsilon_{\alpha\beta}$ parameters which are defined as $\varepsilon_{\alpha\beta} \equiv \sum_{f,P} \frac{n_f}{n_e}\varepsilon_{\alpha\beta}^{fP}$, where $n_{f(e)}$ denotes the f-type fermion (electron) number density along the neutrino trajectory in the earth. The Hamiltonian in flavor basis is given by

$$H^{\text{S+NSI}} = U \begin{pmatrix} 0 & 0 & 0 \\ 0 & \frac{\Delta m_{21}}{2E} & 0 \\ 0 & 0 & \frac{\Delta m_{31}^2}{2E} \end{pmatrix} U^{-1} + a \begin{pmatrix} 1 + \varepsilon_{ee} & \varepsilon_{e\mu} & \varepsilon_{e\tau} \\ \varepsilon_{e\mu}^* & \varepsilon_{\mu\mu} & \varepsilon_{\mu\tau} \\ \varepsilon_{e\tau}^* & \varepsilon_{\mu\tau}^* & \varepsilon_{\tau\tau} \end{pmatrix}. \qquad (8.2)$$

note that off-diagonal elements of $\varepsilon_{\alpha\beta}$ have a complex phase as non-standard CP-phase like $\varepsilon_{\alpha\beta} = |\varepsilon_{\alpha\beta}|e^{i\phi_{\alpha\beta}}$.

If we consider the possible existence of NSI, it is known that accuracy of determination of parameters θ_{13} and δ become worse by so-colled confusion problem [97] [83, 71]. In this chapter, we discuss the degeneracy caused by NSI. First, in order to take similar way to previous chapters, we prepare the approximate formula of oscillation probability with NSI. Perturbation formula in ϵ^2 order which small parameters are

$$s_{13} \sim \frac{\Delta m_{21}^2}{\Delta m_{31}^2} \sim \frac{\Delta m_{21}^2}{2Ea} \sim \varepsilon_{\alpha\beta} \sim \epsilon, \qquad (8.3)$$

is given by [70][1]. The value of s_{13} in (8.3) is reasonable one for the setting of neutrino factory. Remembering $\varepsilon_{\alpha\beta}$ parameters are normalized by weak scale, if the new physics scale is about 1(10) TeV we can naively consider $\varepsilon_{\alpha\beta}$ as order $10^{-2}(10^{-4})$.

With the definition of modified θ_{13} and solar parameter as

$$\Theta_\pm \equiv \pm\frac{\Delta m_{31}^2}{2Ea}s_{13}e^{-i\delta} + s_{23}\varepsilon_{e\mu} + c_{23}\varepsilon_{e\tau} \tag{8.4}$$

$$\Xi \equiv \frac{\Delta m_{21}^2}{2Ea}s_{12}c_{12} + c_{23}\varepsilon_{e\mu} - s_{23}\varepsilon_{e\tau}, \tag{8.5}$$

approximate oscillation probability of $\nu_e \to \nu_\mu$ can be written as

$$P(\nu_e \to \nu_\mu) = 4\left|s_{23}\mathcal{X}_\pm|\Theta_\pm| + e^{i(\xi-\theta_\pm\mp\Delta_{31})}c_{23}\mathcal{Z}|\Xi|\right|^2 \tag{8.6}$$

where $\theta_\pm$ and ξ are the phase of $\Theta_\pm$ and Ξ respectively and

$$\mathcal{X}_\pm \equiv \frac{A}{A\mp\Delta}\sin(A\mp\Delta_{31}) \tag{8.7}$$

$$\mathcal{Z} \equiv \sin A \tag{8.8}$$

(See Appendix A.2 for derivation).

Therefore, $P(\nu_e \to \nu_\mu)$ with NSI depend only $\varepsilon_{e\mu}$ and $\varepsilon_{e\tau}$ in this order; i.e. other $\epsilon_{\alpha\beta}$ can be ignored. The most important point of perturbation formula is that one can easily imagine that NSI confuse with the non-zero θ_{13} and CP-violation from (8.4).

8.1 Intrinsic, sign-Δm_{31}^2, and octant degeneracy with NSI

First, we discuss familiar degeneracy as intrinsic, sign-Δm_{31}^2 and octant degeneracy. As we can see the form of perturbation formula of oscillation probability with NSI (8.6), it remains that the simple structure of dependence of unknown parameters,

$$|\Theta_\pm|, \quad |\Xi|, \quad \chi_\pm \equiv \xi - \theta_\pm \tag{8.9}$$

$|\Theta_\pm|$ can be regarded modified θ_{13} and $\chi_\pm$ is as modified complex phase δ and $|\Xi|$ is additional unknown parameter caused by NSI. Note that CP-conjugate measurements, $|\bar{\Theta}_\pm|, |\bar{\Xi}|$, and $\bar{\chi}$, can not be written by the simple relation of neutrino channel's because they are the independent parameters from $|\Theta_\pm|, |\Xi|, \chi_\pm$.

We can consider the degeneracy with NSI as expansion of familiar degeneracy. But it require careful attention that the number of unknown parameters increase. Therefore we need enough measurements to it, for example, the measurements at different baseline distance or energy, or different channel of oscillations.

Next, we show some characteristic parameter degeneracy of existence of NSI.

---

[1][70] gives the perturbation formula also in ϵ^3 order for $P(\nu_e \to \nu_\mu)$, but in this thesis, we consider up to ϵ^2 for simplicity.

8.2 ϕ-degeneracy

In this subsection, we would discuss the ϕ-degeneracy in CP-conjugate measurement with one ε ($\varepsilon_{e\mu}$ or $\varepsilon_{e\tau}$) which degenerate solutions are characterized only by distinct values of non-standard complex phase ϕ. The ϕ-degeneracy is discovered by [71] in numerical simulation of neutrino factory. The oscillation probability $P(\nu_e \to \nu_\mu)$ and $P(\bar{\nu}_e \to \bar{\nu}_\mu)$ can be written by

$$
\begin{aligned}
P &= \mathcal{F} + \mathcal{G}\cos(\phi_{e\beta} + \alpha) \\
\bar{P} &= \bar{\mathcal{F}} + \bar{\mathcal{G}}\cos(\phi_{e\beta} + \bar{\alpha}),
\end{aligned}
\tag{8.10}
$$

where $\phi_{e\beta}$ is $\phi_{e\mu}$ or $\phi_{e\tau}$ depending on which $\varepsilon_{e\beta}$ we consider, over-line of symbol means anti-neurino channel. Though we do not show the manifest expression of $\mathcal{F}$, $\mathcal{G}$, or α because it is not important to discuss the degeneracy, one can easily obtain it from (8.6) and note that they does not depend on $\phi_{e\beta}$.

One can realize that if there is a condition that $\alpha = \bar{\alpha}$, $\phi'_{e\beta} = 2\pi - \phi^{\text{true}}_{e\beta} - 2\alpha$ duplicates the true oscillation probabilities which made by $\phi^{\text{true}}_{e\beta}$.

This degeneracy can be understood by analogy of intrinsic degeneracy at oscillation maximum without NSI. Namely, the bi-probability plot $(P, \bar{P})$ varying only ϕ have a shape of"line" like Fig. 7.2 which is the special case of ellipse in the condition $\alpha = \bar{\alpha}$. Therefore, holding other parameters, there are discrete degenerate solution in the complex phase ϕ.

8.3 Solar-Atmospheric degeneracy

In this section, we show the simple and characteristic degeneracy in NSI. The approximate formula of oscillation probability relating $\nu_e \to \nu_\mu$ or ν_τ have 6 unknown parameters, $\theta_{13}, \delta, |\varepsilon_{e\mu}|, \phi_{e\mu}, |\varepsilon_{e\tau}|, \phi_{e\tau}$. In order to determine these parameters, let us have 6 independent measurements like

$$
P(\nu_e \to \nu_\mu) = 4\left| s_{23}\mathcal{X}_\pm|\Theta_\pm| + e^{i(\xi - \theta_\pm \mp \Delta_{31})}c_{23}\mathcal{Z}|\Xi| \right|^2
\tag{8.11}
$$

$$
P(\nu_e \to \nu_\tau) = 4\left| c_{23}\mathcal{X}_\pm|\Theta_\pm| - e^{i(\xi - \theta_\pm \mp \Delta_{31})}s_{23}\mathcal{Z}|\Xi| \right|^2
\tag{8.12}
$$

$$
P(\nu_\mu \to \nu_e) = 4\left| s_{23}\mathcal{X}_\pm|\Theta_\pm| + e^{i(\xi - \theta_\pm \pm \Delta_{31})}c_{23}\mathcal{Z}|\Xi| \right|^2
\tag{8.13}
$$

$$
P(\bar{\nu}_e \to \bar{\nu}_\mu) = 4\left| s_{23}\mathcal{X}_\mp|\bar{\Theta}_\pm| + e^{i(\bar{\xi} - \bar{\theta}_\pm \mp \Delta_{31})}c_{23}\mathcal{Z}|\bar{\Xi}| \right|^2
\tag{8.14}
$$

$$
P(\bar{\nu}_e \to \bar{\nu}_\tau) = 4\left| c_{23}\mathcal{X}_\mp|\bar{\Theta}_\pm| - e^{i(\bar{\xi} - \bar{\theta}_\pm \mp \Delta_{31})}s_{23}\mathcal{Z}|\bar{\Xi}| \right|^2
\tag{8.15}
$$

$$
P(\bar{\nu}_\mu \to \bar{\nu}_e) = 4\left| s_{23}\mathcal{X}_\mp|\bar{\Theta}_\pm| + e^{i(\bar{\xi} - \bar{\theta}_\pm \pm \Delta_{31})}c_{23}\mathcal{Z}|\bar{\Xi}| \right|^2.
\tag{8.16}
$$

where $\bar{\Theta}_\pm$ and $\bar{\Xi}$ can be given by $a \to -a$ and taking complex conjugate of $\Theta_\pm$ and Ξ respectively.

One can immediately realize that (8.11-8.16) is invariant under the transformation as

exchanging the coefficient of the solar and the atmospheric scale term like

$$|\Theta_\pm| \to \frac{\mathcal{Z}}{\mathcal{X}_\pm}|\Xi| \quad , \quad |\Xi| \to \frac{\mathcal{X}_\pm}{\mathcal{Z}}|\Theta_\pm|$$

$$|\bar{\Theta}_\pm| \to \frac{\mathcal{Z}}{\mathcal{X}_\mp}|\bar{\Xi}| \quad , \quad |\bar{\Xi}| \to \frac{\mathcal{X}_\mp}{\mathcal{Z}}|\bar{\Theta}_\pm| \tag{8.17}$$

under the maximal θ_{23}.

Therefore, even though we have enough measurements to the number of unknown parameters, it remains the degenerate solution $(\Theta^{\mathrm{II}}, \Xi^{\mathrm{II}}, \bar{\Theta}^{\mathrm{II}}, \bar{\Xi}^{\mathrm{II}}, \xi^{\mathrm{II}} - \theta^{\mathrm{II}}_\pm)$ for true $(\Theta^1_\pm, \Xi^1,$ $\bar{\Theta}^1, \bar{\Xi}^1, \xi^1 - \theta^1_\pm)$. Furthermore, considering the oscillation probabilities with the inverted mass hierarchy, the transformation as

$$|\Theta_\mp| \to \frac{\mathcal{Z}}{\mathcal{X}_\mp}|\Xi| \quad , \quad |\Xi| \to \frac{\mathcal{X}_\pm}{\mathcal{Z}}|\Theta_\pm|$$

$$|\bar{\Theta}_\mp| \to \frac{\mathcal{Z}}{\mathcal{X}_\mp}|\bar{\Xi}| \quad , \quad |\bar{\Xi}| \to \frac{\mathcal{X}_\pm}{\mathcal{Z}}|\bar{\Theta}_\pm|$$

$$\xi - \theta_\mp \to -(\xi - \theta_\pm) \quad , \quad \bar{\xi} - \bar{\theta}_\mp \to -(\bar{\xi} - \bar{\theta}_\pm) \tag{8.18}$$

duplicates the 6 measurements with the normal mass hierarchy.

This type of degeneracy occur only with complex NSI. For example, the coefficient of the solar scale terms can not be modified in the case without NSI or if there is no more complex phase than standard one, one can not take solar-atmospheric exchange because less of the number of free parameters.

8.4 Various degenerate solutions and analytic solutions

At the end of this chapter, we show some example of analytic solutions which reproduce the results of the numerical simulation displayed by [71] using the measurements at different energy.

Fig. 8.1 and 8.2 show the allowed regions produced by numerical simulation of the neutrino factory considering the existence of a element of NSI ($\varepsilon_{e\mu}$ or $\varepsilon_{e\tau}$).

The setting of the simulation : parent muon energy is taken at 50 GeV, two detectors at 3000 km and 7000 km, oscillation channels are $P(\nu_e \to \nu_\mu)$ and $P(\bar{\nu}_e \to \bar{\nu}_\mu)$.

Fig. 8.1 show the result with only $|\varepsilon_{e\mu}|$ and its phase $\phi_{e\mu}$, Fig. 8.2 is same one for $\varepsilon_{e\tau}$. Upper two rows are the results of the measurements only at 3000 km, the third row is the result of only at 7000 km, and last row show the result of combining the measurements of two detectors. For the case where only a single detector at 3000 km is taken into account, allowed regions exist not only in the (input) normal mass hierarchy but also in the inverted one, as shown in the panels in the second row.

We note that for a given true solution, it is possible to obtain the degenerate solutions using analytic expressions as follows. We denote $P(\nu_e \to \nu_\mu)$ in (8.6) with the notation $P(\nu_e \to \nu_\mu) \equiv P_{e\mu}(\delta, \theta_{13}, |\epsilon_{e\alpha}|, \phi_{e\alpha}; E)$ ($\alpha = \mu, \tau$). Since the number of unknown parameters
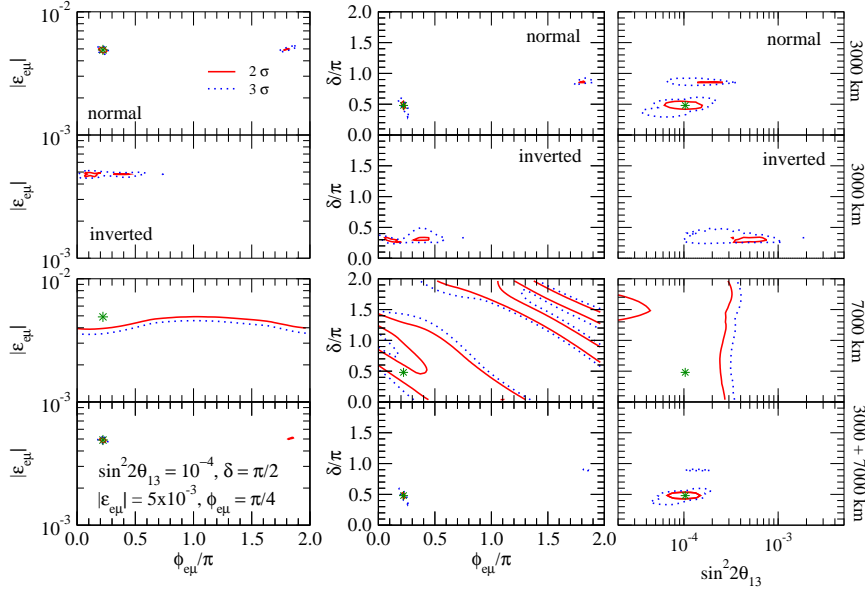
Figure 8.1: Allowed regions in the $\phi_{e\mu} - |\varepsilon_{e\mu}|$ plane (left column), $\phi_{e\mu} - \delta$ plane (middle column) and $\sin^2 2\theta_{13} - \delta$ plane (right column) corresponding to 2 and 3 σ CL obtained for the system with $\varepsilon_{e\mu}$. Panels in the upper 2 rows (3rd row) correspond to the case where only a single detector at 3000 km (7000 km) is taken into account, whereas the ones in the 4th row correspond to the case where results from the two detectors are combined. The input parameters are taken as: $\sin^2 2\theta_{13} = 10^{-4}$, $\delta = \pi/2$, $|\varepsilon_{e\mu}| = 5 \times 10^{-3}$ and $\phi_{e\mu} = \pi/4$ (indicated by the green asterisk), and the mass hierarchy is the normal one.
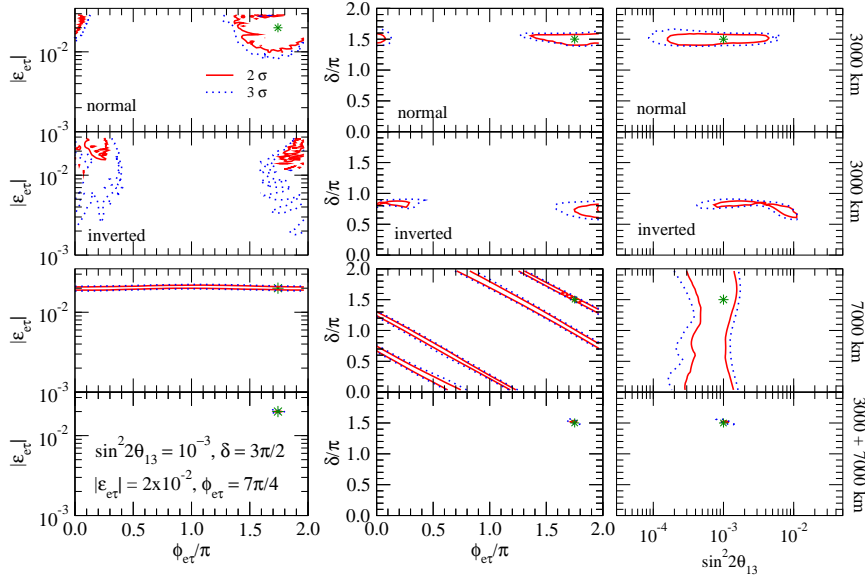
Figure 8.2: Allowed regions with $\varepsilon_{e\tau}$. The input parameters are taken as: $\sin^2 2\theta_{13} = 10^{-3}$, $|\varepsilon_{e\tau}| = 2 \times 10^{-2}$, $\delta = 3\pi/2$, and $\phi_{e\tau} = 7\pi/4$ and normal mass hierarchy.

nature of the solution	hierarchy	$\sin^2 2\theta_{13}$	δ	$|\varepsilon_{e\mu}|$	$\phi_{e\mu}$
input (Fig. 8.1)	normal	0.001	0	0.005	$\frac{3}{4}\pi = 2.4$
solution of (8.19)	normal	0.001	0	0.005	3.9
approximate solution	inverted	0.0035	1.5	0.0046	3.4
approximate solution	inverted	0.0025	1.4	0.0048	5.1

Table 8.1: Presented are solutions of the degeneracy equation (8.19) for input parameters corresponding to Fig. 8.1 given in the first row. See the text for explanation of what "approximate solution of (8.19)" means in the first column of the Table.

are four, $(\theta_{13}, \delta, |\epsilon|, \text{and } \phi)$, we need four observable quantities. Therefore we take the oscillation probabilities $P(\nu_e \to \nu_\mu)$ and $P(\bar{\nu}_e \to \bar{\nu}_\mu)$ at two different energies E_1 and E_2 for these four inputs. Taking the assumed input values of the four parameters given in the caption of Fig. 8.1 and Fig. 8.2, we can solve the equations

$$
\begin{aligned}
P_{e\mu}(\delta^{\text{true}}, \theta_{13}^{\text{true}}, |\epsilon_{e\alpha}^{\text{true}}|, \phi_{e\alpha}^{\text{true}}; E_1) &= P_{e\mu}(\delta^D, \theta_{13}^D, |\epsilon_{e\alpha}^D|, \phi_{e\alpha}^D; E_1) \\
P_{e\mu}(\delta^{\text{true}}, \theta_{13}^{\text{true}}, |\epsilon_{e\alpha}^{\text{true}}|, \phi_{e\alpha}^{\text{true}}; E_2) &= P_{e\mu}(\delta^D, \theta_{13}^D, |\epsilon_{e\alpha}^D|, \phi_{e\alpha}^D; E_2) \\
\bar{P}_{e\mu}(\delta^{\text{true}}, \theta_{13}^{\text{true}}, |\epsilon_{e\alpha}^{\text{true}}|, \phi_{e\alpha}^{\text{true}}; E_1) &= \bar{P}_{e\mu}(\delta^D, \theta_{13}^D, |\epsilon_{e\alpha}^D|, \phi_{e\alpha}^D; E_1) \\
\bar{P}_{e\mu}(\delta^{\text{true}}, \theta_{13}^{\text{true}}, |\epsilon_{e\alpha}^{\text{true}}|, \phi_{e\alpha}^{\text{true}}; E_2) &= \bar{P}_{e\mu}(\delta^D, \theta_{13}^D, |\epsilon_{e\alpha}^D|, \phi_{e\alpha}^D; E_2) \quad (\alpha = \mu, \tau) \quad (8.19)
\end{aligned}
$$

numerically to obtain the degenerate solutions attached the superscript "D". For degenerate solutions, we allow the mass hierarchy can be taken different from input (normal) one like sign-Δm_{31}^2 degeneracy. But θ_{23} is taken maximal ($=\pi/4$) for the sake of shorthand, i.e. we ignore the octant degeneracy. In order to solve (8.19) we take two reference energies as $E_1 = 10$ GeV and $E_2 = 20$ GeV.

The first column of Table 8.1 is to specify the nature of the solutions. The label "approximate solution of (8.19)" implies the following situation: By solving (8.19) with the input parameters in the second column we obtain a complex solution which cannot be regarded as the physical one or it seems that mathematically there is no degeneracy in the Equations (8.19). But the solutions given in Table 8.1 in real numbers which are close enough to the complex solutions reproduce the allowed region of numerical simulation. It should also be noticed that the degeneracy equations (8.19) sometimes have solutions which do not survive in a form of allowed regions as a results of numerical simulation of neutrino factory only with measurement at $L = 3000$ km. For example, there is a solution $\sin^2 2\theta_{13} = 0.0028$, $\delta = 3.5$, $|\varepsilon_{e\mu}| = 0.008$, and $\phi_{e\mu} = 5.1$ for the same input as given in Table 8.1. We confirm that this solution indeed solves the equation (8.19) at $E = 10$ GeV and $E = 20$ GeV, but the oscillation probabilities deviate from the input ones at other energy. Therefore, the degenerate solution was lifted by the spectral informations used by our numerical analysis.

nature of the solution	hierarchy	$\sin^2 2\theta_{13}$	δ	$|\varepsilon_{e\tau}|$	$\phi_{e\tau}$
input (Fig. 8.2)	normal	0.001	$\frac{3}{2}\pi$	0.02	$\frac{7}{4}\pi$
solution of (8.19)	inverted	0.0016	2.77	0.022	0.51

Table 8.2: Presented are solutions of the degeneracy equation (8.19) for input parameters corresponding to Fig. 8.2 given in the first row.

Chapter 9

Conclusion

In this paper, we have analyzed the structure of the parameter degeneracy in neutrino oscillations. We derived the degenerate solutions of the eightfold parameter degeneracy in various settings, CP-conjugate, T-conjugate, CPT-conjugate measurement, as well as the one combining the golden and the silver channels. We have used the approximate forms of the oscillation probabilities derived by Cervera et al., which are widely used in the literatures. Apart from the case of CP-conjugate measurement, the exact solutions are derived by our work for the first time. We also obtain the perturbative formulas of the degenerate solutions, the sign-Δm_{31}^2 solution by the matter perturbation and the octant degeneracy solutions by the the maximal θ_{23} perturbation theories. These formulas make features of the degenerate solutions transparent.

We have revealed a transparent structure of the parameter degeneracy. That is, we uncovered the discrete transformations of the mixing parameters by which the eightfold degeneracy solutions can be related with each other. The transformations consist of the three basic mappings, the intrinsic, the sign, and the octant transformations as defined in Section 6.1. The feature of the relationships between the degeneracy solutions is illuminated in Fig. 1.1. Thanks to the structure of the degeneracy, we can easily understand that, for example, the solutions of the sign-Δm_{31}^2, the θ_{23} octant, and the sign-octant degeneracies come with intrinsic degeneracy pairs. Moreover, one can make predictions on the properties of degenerate solutions by using the solution network.

We mainly treated the degeneracy in $\nu_\mu \to \nu_e$ and its CP-conjugate $\bar{\nu}_\mu \to \bar{\nu}_e$ channel because they may be the most feasible ones from experimental point of view. To give an overview of the parameter degeneracy, we presented the plots of difference between the true and the degenerate solutions in the $\sin^2 2\theta_{13} - \delta/\pi$ plane utilizing the analytic expressions of the degeneracy solutions. Using the plots, we illuminated some significant features of the degeneracy for the three typical superbeam settings and a neutrino factory setting. Overall, the octant degeneracy solutions are close to the true one independent of the baseline settings. The difference between the true and the intrinsic degeneracy solutions of θ_{13} is relatively large compared to those of the other types of the degeneracies, and it becomes larger at smaller values of θ_{13}. In addition, though the sin-Δm_{31}^2 degenerate solution of θ_{13} is close to the true value at short baseline distances, it is very far from the true one at the baseline distance $L = 4000$ km with broadened region of no degeneracy solution.

Furthermore, we analyzed the energy spectra of degenerate solutions. The energy dependence of the sign-Δm_{31}^2 solution is weak in short baseline distances. It can be also understood by perturbation formula for the degenerate solutions. But near the second oscillation maximum, the feature is completely different from that of near the first oscillation maximum, showing a strong energy dependence. On the other hand, intrinsic degeneracy solutions have strong energy dependence even at near the first oscillation maximum. The energy dependence of the octant degeneracy solutions are always weak independent of baseline setting except for region near the second oscillation maximum. These results illuminate which type of degeneracy would be difficult to lift by using the spectrum analysis.

In chapter 8, we have discussed the problem of parameter degeneracy for systems in which NSI exist in addition to standard model interactions. Even if we rely on the approximate form of oscillation probabilities (8.6), we need to determine all the six parameters in the game, $\theta_{13}, \delta, \varepsilon_{\alpha\beta}$; We must have six independent measurement, or the spectrum analysis. Because of the existence of wealth of the NSI parameters, we have shown that there exists a nobel type of degeneracy associate with exchanging the solar and the atmospheric scale oscillation variables. We have also shown that degeneracy of the conventional type, the intrinsic, the sign-Δm_{31}^2, and the octant ones, have natural extension to the systems with non-standard interaction, in which non-standard interaction variables are actively involved. Finally, we presented some examples of analytic treatment of degeneracy in systems with non-standard interaction. They reproduce well the result of the numerical simulation of the neutrino factory measurement.

Acknowledgement

Appendix A

Oscillation Probability Formula in Matter with and without Non-Standard Interaction

A.1 Exact formula of oscillation probability in matter

In this section, we would derive the exact formula of oscillation probability in matter which worked by Kimura-Takamura-Yokomakura[8].

If the electron number density is constant, MSW matter effect does not depend on time. The oscillation probability can be written by the effective eigenvalues, λ_i, and mixing matrix, $\tilde{U}$, of the Hamiltonian in matter,

$$H_{\mathrm{matt}} = \frac{1}{2E} \left(U \begin{pmatrix} m_1^2 & 0 & 0 \\ 0 & m_2^2 & 0 \\ 0 & 0 & m_3^2 \end{pmatrix} U^{-1} + \begin{pmatrix} 2Ea & 0 & 0 \\ 0 & 0 & 0 \\ 0 & 0 & 0 \end{pmatrix} \right), \tag{A.1}$$

$$a = \sqrt{2} G_F n_e, \tag{A.2}$$

as

$$P(\nu_e \to \nu_\mu) = |\sum_i \tilde{U}_{ei}^* e^{-i\frac{\lambda_i}{2E}} \tilde{U}_{\mu i}|^2. \tag{A.3}$$

This is simple exchange of mixing matrix and mass eigenvalues in vacuum to matter. Considering the oscillation probability in vacuum can be written by the products of elements of mixing matrix as $U_{\alpha i}^* U_{\beta i}$, if we have the products of effective mixing matrix, $\tilde{U}_{\alpha i}^* U_{\beta i}$, and effective eigenvalues, λ_i, expressed only by oscillation parameters in vacuum and matter effect, a, it is also possible that oscillation probability in matter can be written by them. The effective eigenvalues can be obtain by solving the eigenvalue equation of (A.1).

First, considering the effective Hamiltonian have a same form as the case in vacuum

except for the elements H_{ee}^{matt}, p and q determined as

$$\frac{p}{2E} \equiv H_{e\mu}^{\text{matt}} \tag{A.4}$$

$$\frac{q}{(2E)^2} \equiv H_{e\tau}^{\text{matt}} H_{\tau\mu}^{\text{matt}} - H_{e\mu}^{\text{matt}} H_{\tau\tau}^{\text{matt}} \tag{A.5}$$

have a simple relation like

$$\sum_i \tilde{U}_{ei}^* \tilde{U}_{\mu i} = \sum_i U_{ei}^* U_{\mu i} = 0 \tag{A.6}$$

$$\sum_i \lambda_i \tilde{U}_{ei}^* \tilde{U}_{\mu i} = \sum_i m_i^2 U_{ei}^* U_{\mu i} = p \tag{A.7}$$

$$\sum_{(i,j,k)}^{\text{cyclic}} \lambda_j \lambda_k \tilde{U}_{ei}^* \tilde{U}_{\mu i} = \sum_{(i,j,k)}^{\text{cyclic}} m_j^2 m_k^2 U_{ei}^* U_{\mu i} = q, \tag{A.8}$$

where cyclic (i, j, k) means sum over (1,2,3),(2,3,1),(3,2,1).

These are the simultaneous equations for three unknown parameters $\tilde{U}_{ei}\tilde{U}_{\mu i}(i = 1, 2, 3)$ and can be solved like

$$\tilde{U}_{ei}^* \tilde{U}_{\mu i} = \frac{p\lambda_i + q}{\Delta\lambda_{ji}\Delta\lambda_{ki}}, \tag{A.9}$$

where $\Delta\lambda_{ij} \equiv \lambda_i - \lambda_j$.

Moreover, expressing the oscillation probability in matter barely,

$$P(\nu_e \to \nu_\mu) = -4 \sum_{(i,j)}^{\text{cyclic}} \text{Re}(\tilde{U}_{ei}^* \tilde{U}_{\mu i} \tilde{U}_{ej} \tilde{U}_{\mu j}^*) \sin^2\left(\frac{\Delta\lambda_{ij}L}{4E}\right) - 2 \sum_{(i,j)}^{\text{cyclic}} \tilde{J} \sin\left(\frac{\Delta\lambda_{ij}L}{2E}\right) \tag{A.10}$$

$$\text{Re}(\tilde{U}_{ei}^* \tilde{U}_{\mu i} \tilde{U}_{ej} \tilde{U}_{\mu j}^*) = \frac{|p|^2 \lambda_i \lambda_j + |q|^2 + \text{Re}(pq^*)(\lambda_i + \lambda_j)}{\Delta\lambda_{ij}\Delta\lambda_{12}\Delta\lambda_{23}\Delta\lambda_{31}} \tag{A.11}$$

$$\tilde{J} = -\frac{\text{Im}(pq^*)}{\Delta\lambda_{12}\Delta\lambda_{23}\Delta\lambda_{31}}. \tag{A.12}$$

Putting the parameters of mixing matrix in vacuum (2.26) into p and q, we take

$$p = p_1 e^{i\delta} + p_2 \tag{A.13}$$

$$q = q_1 e^{i\delta} + q_2 \tag{A.14}$$

$$p_1 = (\Delta m_{31}^2 - \Delta m_{21}^2 s_{12}^2)s_{23}s_{13}c_{13} \quad , \quad p_2 = \Delta m_{21}^2 s_{12}c_{12}c_{23}c_{13}$$
$$q_1 = -\Delta m_{31}^2 \Delta m_{21}^2 c_{12}^2 s_{23}s_{13}c_{13} \quad , \quad q_2 = -\Delta m_{31}^2 \Delta m_{21}^2 s_{12}c_{12}c_{23}c_{13}$$

Therefore the products of (A.11) and (A.12) is given as

$$|p|^2 = p_1^2 + p_2^2 + 2p_1 p_2 \cos\delta \tag{A.15}$$

$$|q|^2 = q_1^2 + q_2^2 + 2q_1 q_2 \cos\delta \tag{A.16}$$

$$\text{Re}(pq^*) = p_1 q_1 + p_2 q_2 + (p_1 q_2 + q_1 p_2)\cos\delta \tag{A.17}$$

$$\text{Im}(pq^*) = (p_2 q_1 - p_1 q_2)\sin\delta \tag{A.18}$$

Herewith, we have the oscillation probability in matter in the form of separating CP phase as

$$P(\nu_e \to \nu_\mu) = D \cos \delta + B \sin \delta + C \tag{A.19}$$

where

$$D = \sum_{(i,j)}^{\text{cyclic}} A_{ij} \sin^2 \left(\frac{\Delta \lambda_{ij} L}{4E} \right) \tag{A.20}$$

$$B = \sum_{(i,j)}^{\text{cyclic}} B' \sin \left(\frac{\Delta \lambda_{ij} L}{2E} \right) \tag{A.21}$$

$$C = \sum_{(i,j)}^{\text{cyclic}} C_{ij} \sin^2 \left(\frac{\Delta \lambda_{ij} L}{4E} \right) \tag{A.22}$$

$$D_{ij} = -4 \left[2p_1 p_2 \lambda_i \lambda_j + 2q_1 q_2 + (p_1 q_2 + q_1 p_2)(\lambda_i + \lambda_j) \right] (\Delta \lambda_{ij} \Delta \lambda_{12} \Delta \lambda_{23} \Delta \lambda_{31})^{-1} \tag{A.23}$$

$$B' = \frac{2(p_1 q_2 - p_2 q_1)}{\Delta \lambda_{12} \Delta \lambda_{23} \Delta \lambda_{31}} \tag{A.24}$$

$$C_{ij} = -4 \left[(p_1^2 + p_2^2) \lambda_i \lambda_j + (q_1^2 + q_2^2) + (p_1 q_1 + q_2 p_2)(\lambda_i + \lambda_j) \right]$$
$$\times (\Delta \lambda_{ij} \Delta \lambda_{12} \Delta \lambda_{23} \Delta \lambda_{31})^{-1} \tag{A.25}$$

A.2 Approximate formula with non-standard interaction by KTY

In this section, we derive the approximate formula of $P(\nu_e \to \nu_\mu)$ with non-standard interaction(NSI) using KTY method.

The Hamiltonian with NSI is given as

$$H^{\text{S+NSI}} = U \begin{pmatrix} 0 & 0 & 0 \\ 0 & \frac{\Delta m_{21}}{2E} & 0 \\ 0 & 0 & \frac{\Delta m_{31}^2}{2E} \end{pmatrix} U^{-1} + a \begin{pmatrix} 1 + \varepsilon_{ee} & \varepsilon_{e\mu} & \varepsilon_{e\tau} \\ \varepsilon_{e\mu}^* & \varepsilon_{\mu\mu} & \varepsilon_{\mu\tau} \\ \varepsilon_{e\tau}^* & \varepsilon_{\mu\tau}^* & \varepsilon_{\tau\tau} \end{pmatrix}. \tag{A.26}$$

Using the following parameters,

$$s_{13} \sim \frac{\Delta m_{21}^2}{\Delta m_{31}^2} \sim \varepsilon_{\alpha\beta} \sim \epsilon, \tag{A.27}$$

let us obtain the approximate formula up to order ϵ^2.

On the condition that matter effect with NSI are constant, KTY method as discussed before can be used to take the oscillation probability. Modifying p and q in (A.4) and (A.5)

for the case with NSI,

$$\frac{p'}{2E} \equiv H_{e\mu}^{\text{S+NSI}}$$

$$= a\left(\frac{\Delta m_{31}^2}{v}s_{23}s_{13}e^{-i\delta} + \frac{\Delta m_{21}^2}{v}s_{12}c_{12}c_{23} + \varepsilon_{e\mu} + O(\epsilon^2)\right) \tag{A.28}$$

$$\frac{q'}{(2E)^2} \equiv H_{e\tau}^{\text{S+NSI}}H_{\tau\mu}^{\text{S+NSI}} - H_{e\mu}^{\text{S+NSI}}H_{\tau\tau}^{\text{S+NSI}}$$

$$= -a^2\frac{\Delta m_{31}^2}{v}\left(\frac{\Delta m_{21}^2}{v}s_{12}c_{12}c_{23} + c_{23}^2\varepsilon_{e\mu} - s_{23}c_{23}\varepsilon_{e\tau} + O(\epsilon^2)\right) \tag{A.29}$$

where $v = 2Ea$.

$$p' = v\left[s_{23}\left(\frac{\Delta m_{31}^2}{v}s_{13}e^{-i\delta} + s_{23}\varepsilon_{e\mu} + c_{23}\varepsilon_{e\tau}\right) + c_{23}\left(\frac{\Delta m_{21}^2}{v}s_{12}c_{12} + c_{23}\varepsilon_{e\mu} - s_{23}\varepsilon_{e\tau}\right)\right]$$

$$+vO(\epsilon^2) \tag{A.30}$$

$$q' = v^2\frac{\Delta m_{31}^2}{v}\left(\frac{\Delta m_{21}^2}{v}s_{12}c_{12} + c_{23}\varepsilon_{e\mu} - s_{23}\varepsilon_{e\tau}\right) + v^2O(\epsilon^2) \tag{A.31}$$

Remembering the form of $\tilde{U}_{ei}^*\tilde{U}_{\mu i}$ that is (A.9), we can ignore the terms proportional to order ϵ^2 in p' and q' and the correction proportional to order ϵ in eigenvalues λ_i because it yield higher order term for our interesting in oscillation probability.

Therefore, one can consider the presence of NSI as just the transformation of s_{13} and Δm_{21}^2 like

$$\frac{\Delta m_{31}^2}{v}s_{13}e^{-i\delta} \rightarrow \frac{\Delta m_{31}^2}{v}s_{13}e^{-i\delta} + s_{23}\varepsilon_{e\mu} + c_{23}\varepsilon_{e\tau} \equiv \Theta \tag{A.32}$$

$$\frac{\Delta m_{21}^2}{v}s_{12}c_{12} \rightarrow \frac{\Delta m_{21}^2}{v}s_{12}c_{12} + c_{23}\varepsilon_{e\mu} - s_{23}\varepsilon_{e\tau} \equiv \Xi \tag{A.33}$$

in ϵ^2 approximate formula of $P(\nu_e \rightarrow \nu_\mu)$.

Inserting the modification (A.32) and (A.33) into standard approximate formula gives the simple expression for the oscillation probability with NSI [70] as the absolute square of superposition of two amplitudes like

$$P(\nu_e \rightarrow \nu_\mu) = 4\left|\frac{\Delta m_{31}^2}{v}s_{13}e^{-i\delta}s_{23}\mathcal{X} + e^{-i\Delta_{31}}\frac{\Delta m_{21}}{v}s_{12}c_{12}c_{23}\mathcal{Z}\right|^2$$

$$\rightarrow 4\left|s_{23}\Theta\mathcal{X} + e^{-i\Delta_{31}}c_{23}\Xi\mathcal{Z}\right|^2 \tag{A.34}$$

where $\mathcal{X} \equiv \frac{A}{A-\Delta}\sin(A-\Delta_{31})$, $\mathcal{Z} \equiv \sin A$.

reference

[1] S. Weinberg, Phys. Rev. Lett. 19, 1264 (1967); A. Salam, p.367 of Elementary Particle Thepty, ed. N. svartholm (Almwuist and Wiksells, Stockholm, 1969); S.L. Glashow, J. Iliopoulos, and L. Maiani, Phys. Rev. D2, 1285 (1970).

[2] M. Kobayashi and T. Maskawa, Prog. Theor. Phys. **49**, 652 (1973).

[3] Z. Maki, M. Nakagawa and S. Sakata, Prog. Theor. Phys. **28**, 870 (1962).

[4] C. Jarlskog, Phys. Rev. Lett. **55**, 1039 (1985).

[5] L. Wolfenstein, Phys. Rev. D **17**, 2369 (1978).

[6] S. P. Mikheev and A. Y. Smirnov, Sov. J. Nucl. Phys. **42**, 913 (1985) [Yad. Fiz. **42**, 1441 (1985)].

[7] C. Amsler et al. (Particle Data Group), PL B667, 1 (2008) and 2009 partial update for the 2010 edition (URL: http://pdg.lbl.gov).

[8] K. Kimura, A. Takamura and H. Yokomakura, Phys. Lett. B **537**, 86 (2002).

[9] C. Kraus *et al.*, Eur. Phys. J. C **40**, 447 (2005) [arXiv:hep-ex/0412056]. V. M. Lobashev *et al.*, Phys. Lett. B **460**, 227 (1999). C. Weinheimer *et al.*, Phys. Lett. B **460**, 219 (1999). and more...

[10] A. Osipowicz *et al.* [KATRIN Collaboration], arXiv:hep-ex/0109033.

[11] E. Komatsu *et al.* [WMAP Collaboration], Astrophys. J. Suppl. **180**, 330 (2009) [arXiv:0803.0547 [astro-ph]].

[12] U. Seljak, A. Slosar and P. McDonald, JCAP **0610**, 014 (2006) [arXiv:astro-ph/0604335].

[13] C. Arnaboldi *et al.* [CUORICINO Collaboration], Phys. Rev. C **78**, 035502 (2008) [arXiv:0802.3439 [hep-ex]].

[14] H. V. Klapdor-Kleingrothaus, A. Dietz, H. L. Harney and I. V. Krivosheina, Mod. Phys. Lett. A **16**, 2409 (2001) [arXiv:hep-ph/0201231].

[15] C. E. Aalseth *et al.*, Mod. Phys. Lett. A **17**, 1475 (2002) [arXiv:hep-ex/0202018].

[16] K. S. Hirata *et al.* [KAMIOKANDE-II Collaboration], Phys. Lett. B **205**, 416 (1988).

[17] K. S. Hirata *et al.* [Kamiokande-II Collaboration], Phys. Lett. B **280**, 146 (1992).

[18] Y. Fukuda *et al.* [Super-Kamiokande Collaboration], Phys. Rev. Lett. **81**, 1562 (1998) [arXiv:hep-ex/9807003].

[19] Y. Ashie *et al.* [Super-Kamiokande Collaboration], Phys. Rev. D **71**, 112005 (2005) [arXiv:hep-ex/0501064].

[20] J. Hosaka *et al.* [Super-Kamiokande Collaboration], Phys. Rev. D **74**, 032002 (2006) [arXiv:hep-ex/0604011].

[21] M. H. Ahn *et al.* [K2K Collaboration], Phys. Rev. Lett. **90**, 041801 (2003) [arXiv:hep-ex/0212007].

[22] M. H. Ahn *et al.* [K2K Collaboration], Phys. Rev. D **74**, 072003 (2006) [arXiv:hep-ex/0606032].

[23] P. Adamson *et al.* [MINOS Collaboration], Phys. Rev. Lett. **101**, 131802 (2008) [arXiv:0806.2237 [hep-ex]].

[24] P. Adamson *et al.* [MINOS Collaboration], arXiv:0909.4996 [hep-ex].

[25] J. N. Bahcall, A. M. Serenelli and S. Basu, Astrophys. J. **621**, L85 (2005) [arXiv:astro-ph/0412440].

[26] R. J. Davis, D. S. Harmer and K. C. Hoffman, Phys. Rev. Lett. **20**, 1205 (1968).

[27] W. Hampel *et al.* [GALLEX Collaboration], Phys. Lett. B **447**, 127 (1999).

[28] J. N. Abdurashitov *et al.* [SAGE Collaboration], Phys. Rev. C **60**, 055801 (1999) [arXiv:astro-ph/9907113].

[29] M. Altmann *et al.* [GNO Collaboration], Phys. Lett. B **490**, 16 (2000) [arXiv:hep-ex/0006034].

[30] K. S. Hirata *et al.* [KAMIOKANDE-II Collaboration], Phys. Rev. Lett. **65**, 1297 (1990).

[31] Y. Fukuda *et al.* [Super-Kamiokande Collaboration], Phys. Rev. Lett. **82**, 1810 (1999) [arXiv:hep-ex/9812009].

[32] J. Hosaka *et al.* [Super-Kamkiokande Collaboration], Phys. Rev. D **73**, 112001 (2006) [arXiv:hep-ex/0508053].

[33] J. P. Cravens *et al.* [Super-Kamiokande Collaboration], Phys. Rev. D **78**, 032002 (2008) [arXiv:0803.4312 [hep-ex]].

[34] Q. R. Ahmad *et al.* [SNO Collaboration], Phys. Rev. Lett. **89**, 011301 (2002) [arXiv:nucl-ex/0204008].

[35] T. S. Collaboration, arXiv:0910.2984 [nucl-ex].

[36] C. Arpesella *et al.* [The Borexino Collaboration], Phys. Rev. Lett. **101**, 091302 (2008) [arXiv:0805.3843 [astro-ph]].

[37] S. Abe *et al.* [KamLAND Collaboration], Phys. Rev. Lett. **100**, 221803 (2008) [arXiv:0801.4589 [hep-ex]].

[38] T. Araki *et al.*, Nature **436**, 499 (2005).

[39] F. Reines and C. L. Cowan, Phys. Rev. **92**, 830 (1953).

[40] M. Apollonio *et al.* [CHOOZ Collaboration], Phys. Lett. B **466**, 415 (1999) [arXiv:hep-ex/9907037].

[41] G. L. Fogli, E. Lisi, A. Marrone, A. Palazzo and A. M. Rotunno, Phys. Rev. Lett. **101**, 141801 (2008) [arXiv:0806.2649 [hep-ph]].

[42] F. Ardellier *et al.* [Double Chooz Collaboration], arXiv:hep-ex/0606025. X. Guo *et al.* [Daya-Bay Collaboration], arXiv:hep-ex/0701029. K. K. Joo [RENO Collaboration], Nucl. Phys. Proc. Suppl. **168**, 125 (2007).

[43] Y. Itow *et al.*, arXiv:hep-ex/0106019.
For an updated version, see: http://neutrino.kek.jp/jhfnu/loi/loi.v2.030528.pdf

[44] Y. Hayato [T2K Collaboration], Nucl. Phys. Proc. Suppl. **143**, 269 (2005).

[45] D. Ayres *et al.* [Nova Collaboration], arXiv:hep-ex/0503053.

[46] M. Guler *et al.* [OPERA Collaboration],

[47] Y. Itow *et al.* [The T2K Collaboration], arXiv:hep-ex/0106019.

[48] M. Mezzetto, J. Phys. G **29**, 1781 (2003) [arXiv:hep-ex/0302005].

[49] Project-X ICD reference. (http://projectx.fnal.gov/)

[50] M. Diwan *et al.*, arXiv:hep-ex/0608023.

[51] V. Barger *et al.*, arXiv:0705.4396 [hep-ph].

[52] P. Zucchelli, Phys. Lett. B **532**, 166 (2002).

[53] J. Burguet-Castell, D. Casper, J. J. Gomez-Cadenas, P. Hernandez and F. Sanchez, Nucl. Phys. B **695**, 217 (2004) [arXiv:hep-ph/0312068].

[54] S. Geer, Phys. Rev. D **57**, 6989 (1998) [Erratum-ibid. D **59**, 039903 (1999)] [arXiv:hep-ph/9712290]. A. De Rujula, M. B. Gavela and P. Hernandez, Nucl. Phys. B **547**, 21 (1999) [arXiv:hep-ph/9811390].

107

[55] J. Burguet-Castell, M. B. Gavela, J. J. Gomez-Cadenas, P. Hernandez and O. Mena, Nucl. Phys. B **608**, 301 (2001) [arXiv:hep-ph/0103258].

[56] H. Minakata and H. Nunokawa, JHEP **0110**, 001 (2001) [arXiv:hep-ph/0108085].

[57] G. L. Fogli and E. Lisi, Phys. Rev. D **54**, 3667 (1996) [arXiv:hep-ph/9604415].

[58] H. Minakata and H. Nunokawa, Nucl. Phys. Proc. Suppl. **110**, 404 (2002) [arXiv:hep-ph/0111131].

[59] V. Barger, D. Marfatia and K. Whisnant, Phys. Rev. D **65**, 073023 (2002) [arXiv:hep-ph/0112119].

[60] A. Donini, D. Meloni and S. Rigolin, JHEP **0406**, 011 (2004) [arXiv:hep-ph/0312072].

[61] H. Minakata, H. Nunokawa and S. J. Parke, Phys. Rev. D **66**, 093012 (2002) [arXiv:hep-ph/0208163].

[62] A. Cervera, A. Donini, M. B. Gavela, J. J. Gomez Cadenas, P. Hernandez, O. Mena and S. Rigolin, Nucl. Phys. B **579**, 17 (2000) [Erratum-ibid. B **593**, 731 (2001)] [arXiv:hep-ph/0002108].

[63] P. Huber and W. Winter, Phys. Rev. D **68**, 037301 (2003) [arXiv:hep-ph/0301257].

[64] J. Kopp, T. Ota and W. Winter, Phys. Rev. D **78**, 053007 (2008) [arXiv:0804.2261 [hep-ph]].

[65] J. W. F. Valle, Phys. Lett. B **199** (1987) 432.

[66] M. M. Guzzo, A. Masiero and S. T. Petcov, Phys. Lett. B **260**, 154 (1991).

[67] Y. Grossman, Phys. Lett. B **359**, 141 (1995) [arXiv:hep-ph/9507344].

[68] Z. Berezhiani and A. Rossi, Phys. Lett. B **535**, 207 (2002) [arXiv:hep-ph/0111137].

[69] H. Minakata, arXiv:0905.1387 [hep-ph].

[70] T. Kikuchi, H. Minakata and S. Uchinami, JHEP **0903**, 114 (2009) [arXiv:0809.3312 [hep-ph]].

[71] A. M. Gago, H. Minakata, H. Nunokawa, S. Uchinami and R. Zukanovich Funchal, JHEP **1001**, 049 (2010) [arXiv:0904.3360 [hep-ph]].

[72] H. Minakata and H. Nunokawa, Phys. Lett. B **495**, 369 (2000) [arXiv:hep-ph/0004114].

[73] J. Sato, Nucl. Instrum. Meth. A **472**, 434 (2001) [arXiv:hep-ph/0008056].

[74] B. Richter, arXiv:hep-ph/0008222.

[75] T. Kobayashi, Talk at 5th TOKUTEI-RCCN Workshop, Institute for Cosmic Ray Research, Chiba, Japan, February 23-24, 2001.

[76] H. Minakata and H. Nunokawa, Nucl. Instrum. Meth. A **503**, 218 (2001) [arXiv:hep-ph/0111130].

[77] H. Minakata, H. Nunokawa and S. J. Parke, Phys. Lett. B **537**, 249 (2002) [arXiv:hep-ph/0204171].

[78] H. Minakata and H. Nunokawa, Phys. Lett. B **413**, 369 (1997) [arXiv:hep-ph/9706281].

[79] M. Ishitsuka, T. Kajita, H. Minakata and H. Nunokawa, Phys. Rev. D **72**, 033003 (2005) [arXiv:hep-ph/0504026].

[80] T. Kajita, H. Minakata, S. Nakayama and H. Nunokawa, Phys. Rev. D **75**, 013006 (2007) [arXiv:hep-ph/0609286].

[81] D. Beavis *et al.*, arXiv:hep-ex/0205040; M. V. Diwan *et al.*, Phys. Rev. D **68**, 012002 (2003) [arXiv:hep-ph/0303081].

[82] H. Minakata, H. Sugiyama, O. Yasuda, K. Inoue and F. Suekane, Phys. Rev. D **68**, 033017 (2003) [Erratum-ibid. D **70**, 059901 (2004)] [arXiv:hep-ph/0211111].

[83] N. Cipriano Ribeiro, H. Minakata, H. Nunokawa, S. Uchinami and R. Zukanovich Funchal, JHEP **0712**, 002 (2007) [arXiv:0709.1980 [hep-ph]].

[84] T. Kajita, H. Minakata and H. Nunokawa, Phys. Lett. B **528**, 245 (2002) [arXiv:hep-ph/0112345].

[85] J. Arafune, M. Koike and J. Sato, Phys. Rev. D **56**, 3093 (1997) [Erratum-ibid. D **60**, 119905 (1999)] [arXiv:hep-ph/9703351].

[86] H. Minakata and H. Nunokawa, Phys. Rev. D **57**, 4403 (1998) [arXiv:hep-ph/9705208].

[87] A. Bandyopadhyay *et al.* [ISS Physics Working Group], Rept. Prog. Phys. **72**, 106201 (2009) [arXiv:0710.4947 [hep-ph]].

[88] T. Abe *et al.* [ISS Detector Working Group], JINST **4**, T05001 (2009) [arXiv:0712.4129 [physics.ins-det]].

[89] S. Geer, O. Mena and S. Pascoli, Phys. Rev. D **75**, 093001 (2007) [arXiv:hep-ph/0701258].

[90] A. D. Bross, M. Ellis, S. Geer, O. Mena and S. Pascoli, Phys. Rev. D **77**, 093012 (2008) [arXiv:0709.3889 [hep-ph]].

[91] V. Barger, M. Dierckxsens, M. Diwan, P. Huber, C. Lewis, D. Marfatia and B. Viren, Phys. Rev. D **74**, 073004 (2006) [arXiv:hep-ph/0607177].

[92] O. L. G. Peres and A. Y. Smirnov, Phys. Lett. B **456**, 204 (1999) [arXiv:hep-ph/9902312]; Nucl. Phys. B **680**, 479 (2004) [arXiv:hep-ph/0309312];

[93] M. C. Gonzalez-Garcia, M. Maltoni and A. Y. Smirnov, Phys. Rev. D **70**, 093005 (2004) [arXiv:hep-ph/0408170].

[94] S. Choubey and P. Roy, Phys. Rev. D **73**, 013006 (2006) [arXiv:hep-ph/0509197].

[95] M. Shiozawa, T. Kajita, S. Nakayama, Y. Obayashi, and K. Okumura, in Proceedings of the RCCN International Workshop on Sub-dominant Oscillation Effects in Atmospheric Neutrino Experiments, Kashiwa, Japan, Dec. 2004, p.57; T. Kajita, Nucl. Phys. Proc. Suppl. **155**, 87 (2006).

[96] K. Hiraide, H. Minakata, T. Nakaya, H. Nunokawa, H. Sugiyama, W. J. C. Teves and R. Zukanovich Funchal, Phys. Rev. D **73**, 093008 (2006) [arXiv:hep-ph/0601258].

[97] P. Huber, T. Schwetz and J. W. F. Valle, Phys. Rev. Lett. **88**, 101804 (2002) [arXiv:hep-ph/0111224].

[98] P. Huber, M. Maltoni and T. Schwetz, Phys. Rev. D **71**, 053006 (2005) [arXiv:hep-ph/0501037].

[99] D. Meloni, Phys. Lett. B **664**, 279 (2008) [arXiv:0802.0086 [hep-ph]].

[100] J. E. Campagne, M. Maltoni, M. Mezzetto and T. Schwetz, JHEP **0704**, 003 (2007) [arXiv:hep-ph/0603172].